Volume 2 | Issue 4 | September 2022

MICROSTRUCTURES

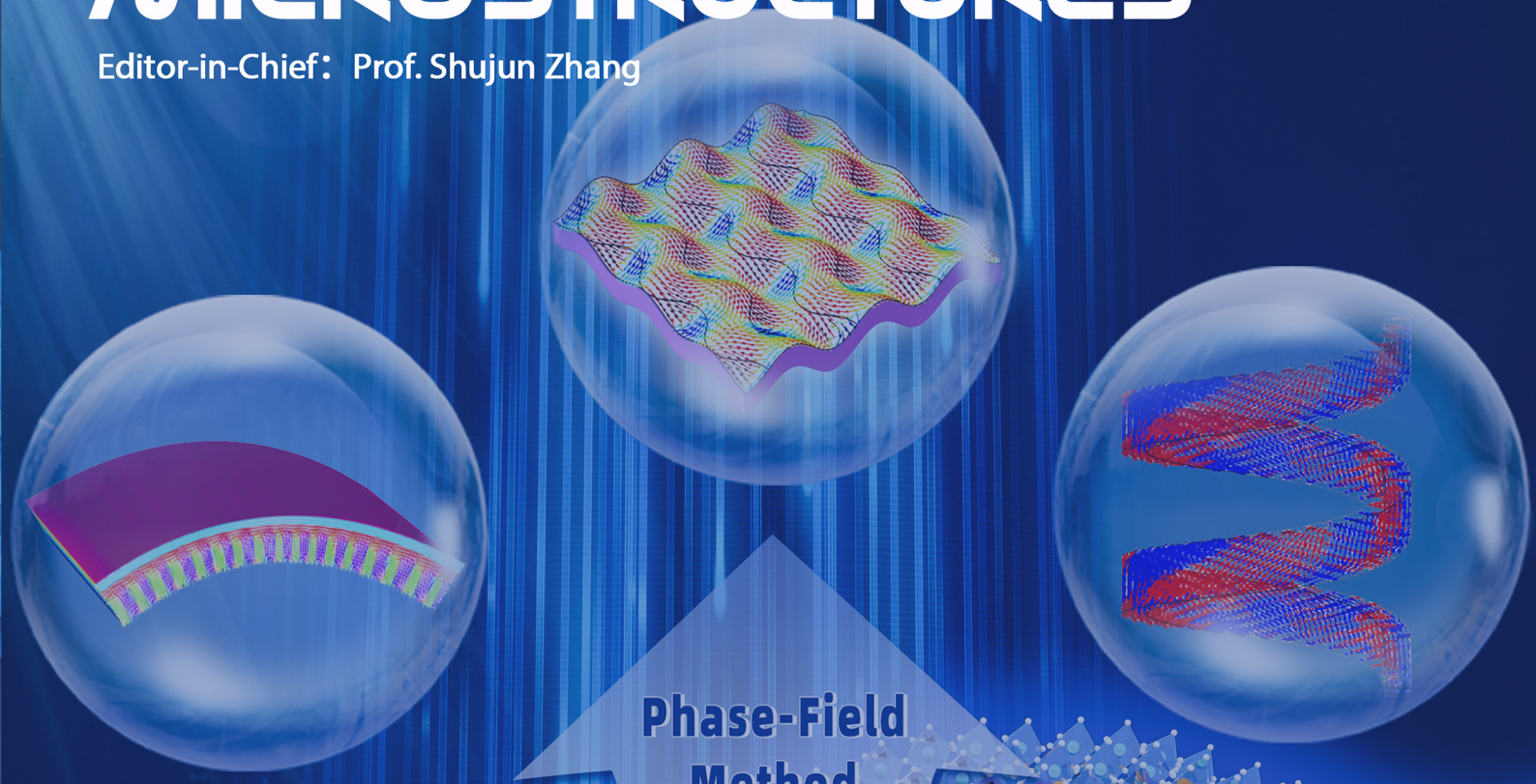

Phase-Field Method

Design of super-elastic freestanding ferroelectric thin films guided by phase-field simulations

Changqing Guo, Houbing Huang*

Open Access
ISSN 2770-2995 (Online)
www.microstructj.com

EDITORIAL BOARD

GENERAL INFORMATION

About the Journal

Microstructures, ISSN 2770-2995 (Online), is a peer-reviewed and continuously published online journal with print on demand compilation of articles published. The journal's full text is available online at www.jcmtjournal.com. The journal allows free access (Open Access) to its contents and permits authors to self-archive final accepted version of Microstructure, which is the nature, quantity and distribution of structural elements or phases that make up materials, determines the properties of materials. Understanding microstructure–properties relationships is critical for the design of materials. With the increase of demand and investment in new materials around the globe, there has been a great deal of interest in the exploration and manipulation of microstructure in materials science and engineering.

Information for Authors

Manuscripts should be prepared in accordance with Author Instructions.
Please check www.microstructj.com/pages/view/author_instructions for details.
All manuscripts should be submitted online at https://oaemesas.com/login?JournalId=microstructures.

Copyright

Permissions

For information on how to request permissions to reproduce articles/information from this journal, please visit www.microstructj.com.

Disclaimer

The information and opinions presented in the journal reflect the views of the authors and not of the journal or its Editorial Board or the Publisher. Publication does not constitute endorsement by the journal. Neither the *Microstructures* nor its publishers nor anyone else involved in creating, producing or delivering the *Microstructures* or the materials contained therein, assumes any liability or responsibility for the accuracy, completeness, or usefulness of any information provided in the *Microstructures*, nor shall they be liable for any direct, indirect, incidental, special, consequential or punitive damages arising out of the use of the *Microstructures*. The *Microstructures*, nor its publishers, nor any other party involved in the preparation of material contained in the *Microstructures* represents or warrants that the information contained herein is in every respect accurate or complete, and they are not responsible for any errors or omissions or for the results obtained from the use of such material. Readers are encouraged to confirm the information contained herein with other sources.

Publisher

OAE Publishing Inc.
245 E Main Street st112, Alhambra, CA 91801, USA
Website: www.oaepublish.com

Contacts

E-mail: editorialoffice@microstructj.com
Website: www.microstructj.com

Microstructures

CONTENTS

Volume 2 / Issue 4 / October 2022 /

Research Article

Review

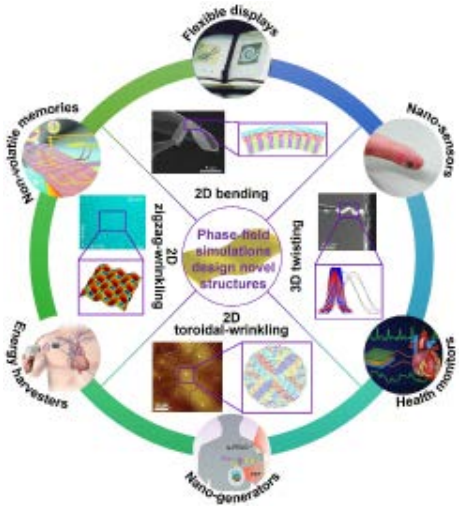

Article Highlights: Understanding the dynamic behavior of domain structures is critical to the design and application of super-elastic freestanding ferroelectric thin films. Phase-field simulations represent a powerful tool for observing, exploring and revealing the domain-switching behavior and phase transitions in ferroelectric materials at the mesoscopic scale. This review summarizes the recent theoretical progress regarding phase-field methods in freestanding ferroelectric thin films and novel buckling-induced wrinkled and helical structures. Furthermore, the strong coupling relationship between strain and ferroelectric polarization in super-elastic ferroelectric nanostructures is confirmed and discussed, resulting in new design strategies for the strain engineering of freestanding ferroelectric thin film systems. Finally, to further promote the innovative development and application of freestanding ferroelectric thin film systems, this review provides a summary and outlook on the theoretical modeling of freestanding ferroelectric thin films

Available at: No. 2022021

Lu *et al. Microstructures* 2022;2:2022017
DOI: 10.20517/microstructures.2022.14

Microstructures

Research Article

Open Access

Detwinning/twin growth-induced phase transformation in a metastable compositionally complex alloy

Wenjun Lu[1], **Fengchao An**[1], **Christian H. Liebscher**[2]

[1]Department of Mechanical and Energy Engineering, Southern University of Science and Technology, Shenzhen 518055, Guangdong, China.
[2]Max-Planck-Institut für Eisenforschung, Max-Planck-Straße 1, Düsseldorf 40237, Germany.

Correspondence to: Prof. Wenjun Lu, Department of Mechanical and Energy Engineering, Southern University of Science and Technology, 1088 Xueyuan Blvd, Nanshan, Shenzhen 518055, Guangdong, China. E-mail: luwj@sustech.edu.cn; Prof. Christian H. Liebscher, Max-Planck-Institut für Eisenforschung, Max-Planck-Straße 1, Düsseldorf 40237, Germany. E-mail: liebscher@mpie.de

How to cite this article: Lu W, An F, Liebscher CH. Detwinning/twin growth-induced phase transformation in a metastable compositionally complex alloy. *Microstructures* 2022;2:2022017. https://dx.doi.org/10.20517/microstructures.2022.14

Received: 9 Jun 2022 **First Decision:** 29 Jun 2022 **Revised:** 11 Jul 2022 **Accepted:** 8 Aug 2022 **Published:** 12 Aug 2022

Academic Editors: Zibin Chen, Jian Wang **Copy Editor:** Fangling Lan **Production Editor:** Fangling Lan

Abstract

Extensive experiments have shown that the transformation from the face-centered cubic to hexagonal close-packed ε phase usually occurs around coherent Σ3 boundaries. However, in this letter, we reveal a different transformation mechanism in a metastable dual-phase compositionally complex alloy via a systematic high-resolution scanning transmission electron microscopy analysis. The face-centered cubic γ matrix can be transformed to the hexagonal close-packed ε phase (as small as one unit) around an incoherent Σ3 boundary (~30 nm), i.e., the facet of the coherent Σ3 boundary. This transformation is assisted by the detwinning/twin growth of a coherent Σ3 boundary during annealing treatment (900 °C for 60 min).

Keywords: Detwinning/twin growth, incoherent Σ3 boundary, 9R structure, displacive transformation, compositionally complex alloy

INTRODUCTION

Phase transformation-assisted alloys have motivated investigations due to their exceptional mechanical properties and excellent application potential in advanced technologies[1-6]. However, a key bottleneck that

hinders their widespread applications is the traditional strength-ductility trade-off[7]. It was recently reported that dual-phase compositionally complex alloys (CCAs) could overcome this hurdle[8-12]. The dual-phase non-equiatomic FeMnCoCr CCA contains face-centered cubic (FCC) γ and hexagonal close-packed (HCP) ε phases, which are obtained by successive cold rolling, annealing above 900 °C and water quenching[8]. Owing to the metastable FCC γ and stable HCP ε phases at room temperature, the mechanical deformation can actively promote the transformation from FCC γ to HCP ε phase[4,5,11]. Such a phase transformation mainly contributes to the work hardening and thus optimizes the strength and ductility simultaneously.

Generally, the displacive transformation from the FCC γ to HCP ε phase is preferentially initiated at high-angle grain boundaries (HAGBs) or the grain interior with a high dislocation density[8,9]. A Σ3 twin boundary is not an ideal nucleation site for the γ→ε phase transformation, owing to its perfect coincidence site lattice (…ABCABACBA… stacking) and low energy state[13]. For a coherent Σ3 boundary, the grain orientation[14], chemical segregation[1,15,16], internal stresses[1,17] and temperature effect[18] can play key roles in promoting the phase transformation. However, the effects of incoherent Σ3 boundary segments (i.e., de-twinning/twin growth processes)[19,20] on the phase transformation are still ambiguous.

In the present work, the microstructure of a dual-phase $Fe_{50}Mn_{30}Co_{10}Cr_{10}$ (at.%) CCA subjected to a high-temperature annealing treatment and subsequent water quenching is examined, focusing on the displacive transformations at the twin boundaries. We observe that the HCP ε phase is formed at the 9R structure, which is attached to the phase boundaries of the nanoscale {112} incoherent twin boundary[21-24]. The phase transformation mechanisms are systemically investigated through multiple electron microscopies and discussed based on kinetics and thermodynamics.

MATERIALS AND METHODS

In this letter, an ingot of a quaternary dual-phase CCA (40 mm × 40 mm × 6 mm) with a nominal composition of Fe-30Mn-10Co-10Cr (at.%) was cast by vacuum induction melting using pure metals (> 99.5 wt.% purity). The ingot was then hot rolled at 900 °C with a thickness reduction ratio of 50% and homogenized for 2 h at 1200 °C in high-purity argon gas flow, followed by water quenching. In order to obtain a proper recrystallized grain size and phase fraction for later analysis, cold rolling was conducted on the homogenized CCA with a thickness reduction ratio of 60%, followed by annealing at 900 °C for 60 min in an argon-protected furnace and water quenching. The recrystallized sample surface was mechanically ground with silicon carbide abrasive paper (P60 to P4000) and then polished using 3 and 1 μm diamond suspensions. The final polishing was conducted using a 50 nm SiO_2 suspension to remove the residual stress on the surface. The microstructure of the polished bulk sample (10 mm × 10 mm × 1.2 mm) was characterized by means of scanning electron microscopy (SEM) equipped with an electron backscattered diffraction (EBSD) TSL high-speed detector using a 50 nm step size and a 15-kV acceleration voltage (JEOL-6500 FEG-SEM). Electron channeling contrast (ECC) imaging was conducted using a Zeiss Merlin microscope. For transmission electron microscopy (TEM)/scanning TEM (STEM) observations, a lift-out lamella containing multiple Σ3 twins was cut using a site-specific procedure in a dual-beam focused ion beam/SEM (FEI Helios Nanolab 600i) instrument[25]. The bright/dark-field TEM images and selected area electron diffraction (SAED) patterns were acquired in an image aberration-corrected FEI Titan Themis 80-300 microscope operated at a 300-kV accelerating voltage. High-resolution STEM imaging and energy-dispersive X-ray spectroscopy (EDS) were carried out using a probe aberration-corrected FEI Titan Themis 60-300 with an acceleration voltage of 300-kV. For high-angle annular dark-field (HAADF) imaging, a probe semi-convergence angle of 17 mrad and inner and outer semi-collection angles of the annular detector ranging from 73 to 200 mrad were used[26].

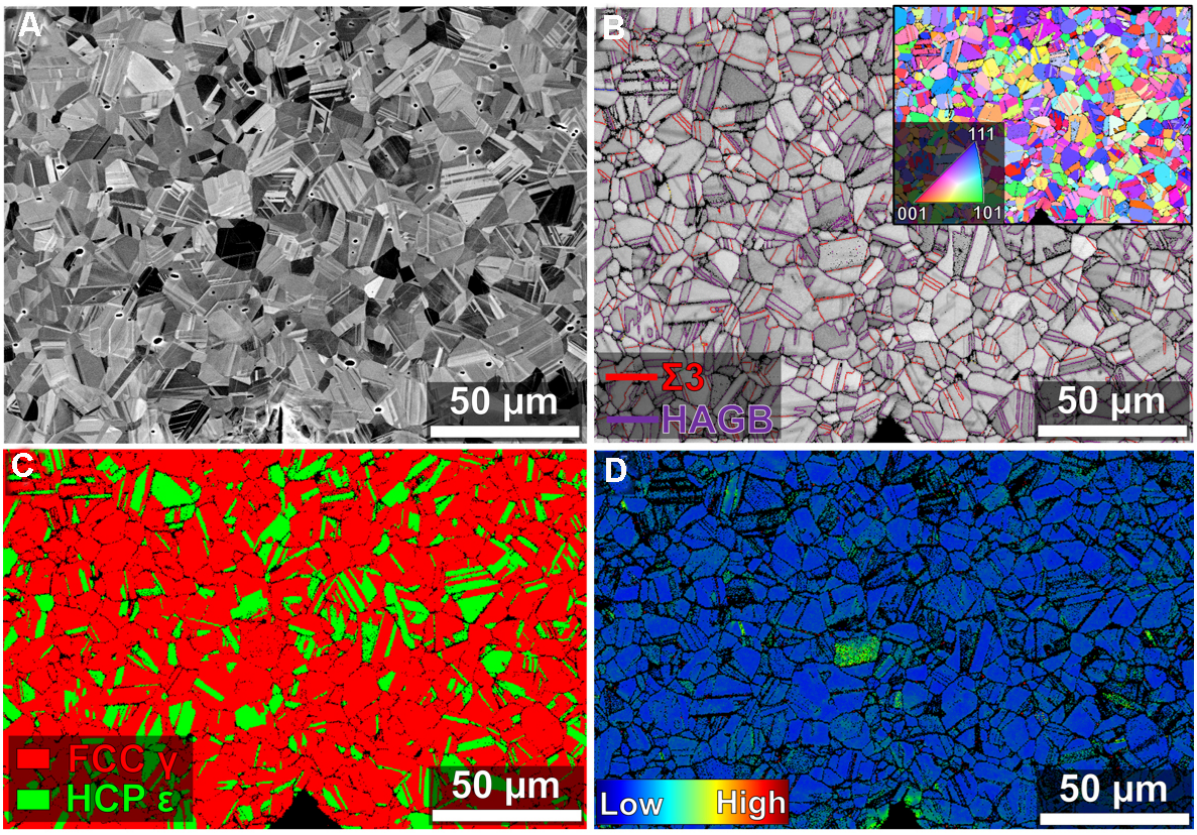

Figure 1. Microstructural characterization for metastable CCA after hot rolling and homogenization. (A) ECC image of the water-quenched sample. (B) EBSD boundary map of same sample region imaged in (A). The inset on the right is the EBSD orientation map. (C and D) Corresponding EBSD phase and KAM maps. The FCC γ and HCP ε phases, Σ3 twin boundary and HAGB are highlighted by red, green, red, and purple, respectively. CCA: Compositionally complex alloy; ECC: electron channeling contrast; EBSD: electron backscattered diffraction; KAM: kernel average misorientation; FCC: face-centered cubic; HCP: hexagonal close-packed; HAGB: high-angle grain boundary.

RESULTS AND DISCUSSION

Figure 1A shows an ECC image of the non-equiatomic CCA. After the annealing treatment, a fully recrystallized CCA with an equiaxed-grained microstructure was obtained. The correlative EBSD data [Figure 1B], including boundary and orientation maps, illustrate that the recrystallized CCA has an average grain size larger than 10 μm with a large amount of annealing twin boundaries (over 42.8 area.%). Further EBSD phase and kernel average misorientation (KAM) maps [Figure 1C and D] show that the CCA has a dual-phase structure containing the FCC γ (69 area.%) and HCP ε (31 area.%) phases with an extremely low dislocation density due to complete recrystallization at high temperature (e.g., 900 °C for 60 min). Upon such a high-temperature recrystallization process, the annealing twins randomly distribute in the FCC γ matrix, while the HCP ε phase is heterogeneously nucleated within the FCC matrix due to the thermal stress induced by the water quenching[8,9,21]. This nucleation behavior of the HCP ε phase may have an intimate connection with the annealing twin boundaries during phase transformation. Further tensile deformation confirms that the annealing twin boundaries are inversely proportional to the HCP ε phase (i.e., Σ3↑; ε↓), as shown in Supplementary Material Figure 1.

Figure 2A shows a representative bright-field TEM image of the CCA containing an annealing twin. The red dashed lines indicate the position of the coherent Σ3 boundaries parallel to the {111} habit plane.

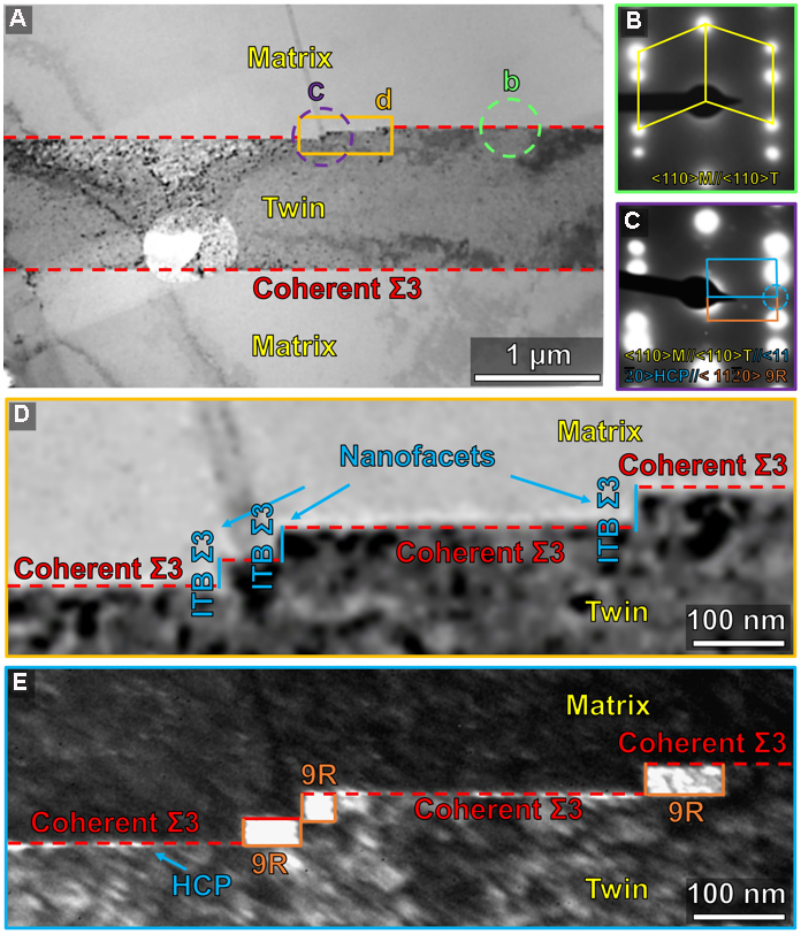

Figure 2. TEM analysis of $Fe_{50}Mn_{30}Co_{10}Cr_{10}$ (at.%) CCA after water quenching. (A) Low-magnification bright-field TEM image of a Σ3 twin within the CCA matrix. The Σ3 twin consists of two coherent Σ3 boundaries (indicated by red dashed lines) and three nanofacets (marked by orange solid square). (B and C) Corresponding SAEDs along the <110>γ zone axis taken from the green and purple dashed circles in (A), respectively. (D) High-magnification bright-field TEM image of Σ3 twin boundary from (A). Three nanofacets are referred to as incoherent Σ3 boundary boundaries (ITBs) and highlighted in blue. (E) Corresponding dark-field TEM image of (D) obtained using the reflection marked by the blue dashed circle in (C). TEM: Transmission electron microscopy; CCA: compositionally complex alloy; SAEDs: selected area electron diffractions.

Figure 2B and C show the corresponding SAEDs of the regions marked by green and purple dashed circles, respectively, in Figure 2A. Different from the coherent Σ3 boundary in Figure 2B, Figure 2C shows a special Σ3 boundary with mixed diffractions composed of the twin, 9R structure and HCP ε phase. The orientation relationships among the matrix, twin, 9R structure and HCP ε phase are determined to be $\{111\}_{matrix}//\{111\}_{twin}//\{0001\}_{9R}//\{0001\}_{HCP}$;$<110>_{matrix}//<011>_{twin}//<11\text{-}20>_{9R}//<11\text{-}20>_{HCP}$[22,23]. Figure 2D presents an enlarged area of this abnormal Σ3 boundary cropped by an orange solid square in Figure 2A. From this image, there are three obvious steps, i.e., nanofacets (~30 nm), visible within the coherent Σ3 boundaries. These nanofacets are parallel to the {112} habit plane, which corresponds to the incoherent Σ3 boundary[21]. Using one of the diffraction spots marked by a blue dashed circle in Figure 2C, a corresponding dark-field TEM image of the 9R structure is obtained from the same position in Figure 2D, as shown in Figure 2E. From this image, it is observed that the 9R structures (~30-80 nm) extend from the incoherent Σ3 boundaries, indicating that they are formed by partial dislocation movement[21]. Furthermore, a weak contrast from the HCP ε phase is found around the coherent Σ3 boundary near the 9R structure. This can be confirmed by further high-resolution STEM analysis in the next section.

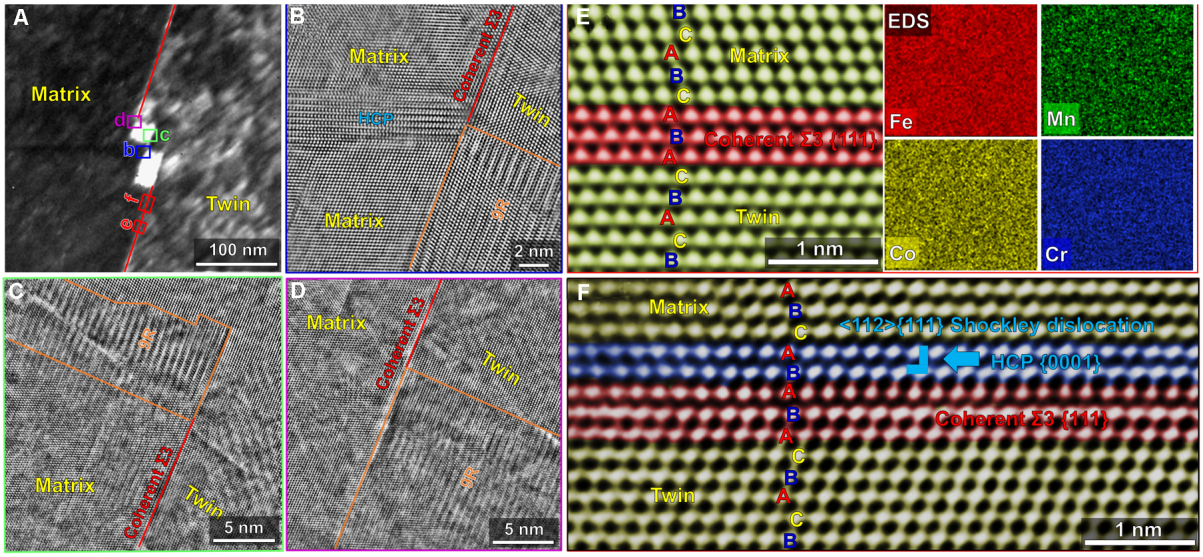

Figure 3. (A) Dark-field TEM image of region shown in Figure 2D. (B-D) High-resolution HAADF-STEM images of Σ3 twin boundary from three different positions, b-d marked in (A). (E) High-resolution HAADF-STEM image from (A) showing a triple atomic layer of a coherent Σ3 boundary with ABA stacking sequence. The corresponding EDS maps indicate a homogenous distribution of the four principle elements, i.e., Fe, Mn, Co and Cr. (F) High-resolution HAADF-STEM image from (A) showing a double atomic layer of HCP ε phase with BA stacking sequence formed by gliding of a leading Shockley partial dislocation. The matrix, coherent Σ3 boundary, 9R structure and HCP ε phase are highlighted by yellow, red, orange, and blue, respectively, in all HAADF-STEM images. TEM: Transmission electron microscopy; HCP: hexagonal close-packed; HAADF: high-angle annular dark-field; STEM: scanning transmission electron microscopy; EDS: X-ray spectroscopy.

Figure 3 shows the TEM/STEM analysis of the nanofacets in Figure 2. For the sample regions marked by blue, green and purple solid squares in the dark-field TEM image [Figure 3A], high-resolution HAADF-STEM is utilized to characterize the atomic configuration at the corresponding positions [Figure 3A-D] near the nanofacets. In these regions, the 9R structures are bounded by two phase boundaries and their atomic stacking parallels to the {0001} habit plane. In addition, the direct proximity of the 9R structures to incoherent Σ3{112} boundaries indicates that they have nucleated from there and then grow along the direction parallel to the {111} coherent Σ3 boundary. This suggests that the formation of the 9R structures stems from the emission of partial dislocations from the incoherent Σ3 boundary under the thermal stresses imposed by water quenching[21,22,27]. Figure 3E and F show high-resolution HAADF-STEM images of the coherent twin boundary for the positions ~50 and ~20 nm away from the 9R structure, respectively. As shown in Figure 3E, a perfect twin structure with …ABCABACBA… stacking[28] is observed ~50 nm away from the 9R structure. Further STEM-EDS analysis [Figure 3E] shows that four principle elements (Fe, Mn, Co and Cr) are homogeneously distributed. However, the Σ3 boundary in close proximity to the 9R structure (…ABCBCACAB…) [Figure 3B-D] only ~20 nm away adopts a different atomic arrangement with …ABCABABACBA… stacking [Figure 3F]. The additional BA stacking around the coherent Σ3 boundary corresponds to one stacking fault or one unit of the HCP ε phase[1]. The presence of this additional HCP ε phase indicates that the phase transformation from the FCC γ to HCP ε phase at the coherent Σ3 boundary initiates from the 9R structure and its phase boundary, which is composed of an array of partial dislocations[21,22,27].

We now discuss the details of the phase transformations at the annealing twin boundaries after the high-temperature treatment. Figure 4 shows an overview of the displacive transformations at different stages. Initially, nanoscale incoherent twin boundaries [Figure 4A] with {112} habit planes are either generated by twin growth or detwinning by the gliding of partial dislocations (i.e., processes with a set of partial

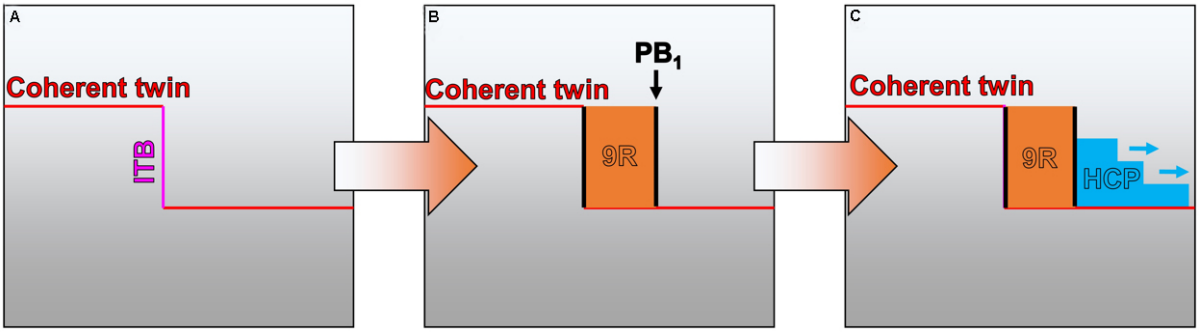

Figure 4. Schematic mechanism of detwinning/twin growth-induced phase transformations at a Σ3 boundary after water quenching. (A) Formation of incoherent twin boundary along the coherent twin boundary. (B) Generation of 9R structure from incoherent twin boundary. (C) Promotion of HCP phase near 9R structure. HCP: Hexagonal close-packed.

dislocations: b_1-edge dislocation; b_2-screw dislocation; b_3-screw dislocation)[21]. Since the mobility of the edge dislocation, b_1 is higher than that of the screw dislocations, b_2 and b_3[22], the 9R structure can be spontaneously formed from the incoherent Σ3 boundary by the motion of b_1 during water quenching (i.e., thermal stresses), as shown in Figure 4B. Such a 9R structure is bounded by two-phase boundaries, which effectively are an array of regularly spaced partial dislocations[21,22]. Such dislocations can actively promote the formation of stacking faults (i.e., Shockley partial dislocations) around the phase boundary of the 9R structure and eventually produce the HCP ε phase via the overlapping of stacking faults [Figure 4C]. From a thermodynamic perspective, the 9R structure usually has a higher Gibbs free energy than that of the matrix (e.g., 357-484 mJm^{-2} in Al and 590-714 mJm^{-2} in Cu)[29]. Such a significant energy difference can be a driving force to promote the formation of the HCP ε phase. Furthermore, based on ab initio calculations of a CrCoNi medium entropy alloy, it is argued that the metastable 9R phase (with a formation energy of -4.809 eV) can induce the stable HCP ε phase (with a formation energy of -4.815 eV) inside the FCC matrix (with a formation energy of -4.808 eV)[30]. Different from the incoherent Σ3 boundary with the 9R structure, the coherent Σ3 boundary is not an ideal nucleation site for the phase transformation from the FCC γ to the HCP ε phase, owing to its perfect coincidence site lattice and low energy state[13,31,32]. This suggests that the HCP ε phase observed along the coherent Σ3 boundary is generally originating from the 9R structure rather than the coherent Σ3 boundary itself. This also clarifies why the HCP ε phase mainly forms along one side of the coherent Σ3 boundary rather than both sides [Figure 4C]. This phase transformation mechanism is thus fundamentally different from those induced by grain orientation, chemical segregation, internal stress and temperature[1,14,15,17].

CONCLUSIONS

In this study, we revealed and discussed the phase transformation around annealing twins in a metastable compositionally complex alloy after water quenching via a systematic high-resolution scanning transmission electron microscopy analysis. The main conclusions are summarized as follows:

1. The FCC γ matrix can be transformed to the HCP ε phase (as small as one unit) around an incoherent Σ3 boundary (~30 nm), i.e., the facet of the coherent Σ3 boundary.

2. The incoherent Σ3 boundary and associated 9R structures (~30-80 nm) can serve as nucleation sites for such a γ→ε phase transformation.

3. The phase transformation is assisted by the detwinning/twin growth of a coherent Σ3 boundary during annealing treatment (900 °C for 60 min).

4. This finding provides novel insights into the nature of phase transformations at twin boundaries in a non-equiatomic dual-phase compositionally complex alloy.

DECLARATIONS

Authors' contributions

Design: Lu W
Experiments: Lu W
Data analysis: Lu W
Manuscript writing: Lu W, An F, Liebscher CH
Manuscript revision and supervising: Lu W, Liebscher CH

Availability of data and materials

Not applicable.

Financial support and sponsorship

Wenjun Lu is grateful for financial support from the open research fund of Songshan Lake Materials Laboratory (2021SLABFK05) and the Shenzhen Science and Technology Program (JCYJ20210324104404012). The authors acknowledge the use of the facilities at the Southern University of Science and Technology Core Research Facility.

Conflicts of interest

All authors declared that there are no conflicts of interest.

Ethical approval and consent to participate

Not applicable.

Consent for publication

Not applicable.

REFERENCES

1. Koizumi Y, Suzuki S, Yamanaka K, et al. Strain-induced martensitic transformation near twin boundaries in a biomedical Co-Cr-Mo alloy with negative stacking fault energy. *Acta Materialia* 2013;61:1648-61.
2. Harjo S, Tsuchida N, Abe J, Gong W. Martensite phase stress and the strengthening mechanism in TRIP steel by neutron diffraction. *Sci Rep* 2017;7:15149. DOI PubMed PMC
3. Sohn SS, Song H, Jo MC, Song T, Kim HS, Lee S. Novel 1.5 GPa-strength with 50%-ductility by transformation-induced plasticity of non-recrystallized austenite in duplex steels. *Sci Rep* 2017;7:1255. DOI PubMed PMC
4. Ding L, Hilhorst A, Idrissi H, Jacques P. Potential TRIP/TWIP coupled effects in equiatomic CrCoNi medium-entropy alloy. *Acta Materialia* 2022;234:118049.
5. Chandan AK, Kishore K, Hung PT, et al. Effect of nickel addition on enhancing nano-structuring and suppressing TRIP effect in Fe40Mn40Co10Cr10 high entropy alloy during high-pressure torsion. *Int J Plast* 2022;150:103193.
6. Zhang Z, Jiang Z, Xie Y, Chan SLI, Liang J, Wang J. Multiple deformation mechanisms induced by pre-twinning in CoCrFeNi high entropy alloy. *Scripta Materialia* 2022;207:114266.
7. Fu Y, Liu J, Shi J, Cao W, Dong H. Effects of cold rolling reduction on retained austenite fraction and mechanical properties of high-Si TRIP steel. *J Iron Steel Res Int* 2013;20:50-6. DOI
8. Li Z, Pradeep KG, Deng Y, Raabe D, Tasan CC. Metastable high-entropy dual-phase alloys overcome the strength-ductility trade-off.

Nature 2016;534:227-30. DOI PubMed
9. Li Z, Tasan CC, Pradeep KG, Raabe D. A TRIP-assisted dual-phase high-entropy alloy: grain size and phase fraction effects on deformation behavior. *Acta Materialia* 2017;131:323-35.
10. Li Z, Körmann F, Grabowski B, Neugebauer J, Raabe D. Ab initio assisted design of quinary dual-phase high-entropy alloys with transformation-induced plasticity. *Acta Materialia* 2017;136:262-70.
11. Lu W, Liebscher CH, Dehm G, Raabe D, Li Z. Bidirectional transformation enables hierarchical nanolaminate dual-phase high-entropy alloys. *Adv Mater* 2018;30:e1804727. DOI PubMed
12. Gao X, Liu T, Zhang X, Fang H, Qin G, Chen R. Precipitation phase and twins strengthening behaviors of as-cast non-equiatomic CoCrFeNiMo high entropy alloys. *J Alloys Comp* 2022;918:165584. DOI
13. Lu K, Lu L, Suresh S. Strengthening materials by engineering coherent internal boundaries at the nanoscale. *Science* 2009;324:349-52. DOI PubMed
14. Ma L, Wang L, Nie Z, et al. Reversible deformation-induced martensitic transformation in Al0.6CoCrFeNi high-entropy alloy investigated by in situ synchrotron-based high-energy X-ray diffraction. *Acta Materialia* 2017;128:12-21.
15. Moon J, Qi Y, Tabachnikova E, et al. Deformation-induced phase transformation of Co20Cr26Fe20Mn20Ni14 high-entropy alloy during high-pressure torsion at 77 K. *Mater Lett* 2017;202:86-8.
16. Hou J, Li J, Lu W. Twin boundary-assisted precipitation of sigma phase in a high-entropy alloy. *Mater Lett* 2021;300:130198.
17. Heinz A, Neumann P. Crack initiation during high cycle fatigue of an austenitic steel. *Acta Metallurgica Materialia* 1990;38:1933-40.
18. García ADJ, Medrano AM, Rodríguez AS. Formation of hcp martensite during the isothermal aging of an fcc Co-27Cr-5Mo-0.05C orthopedic implant alloy. *Metall Mat Trans A* 1999;30:1177-84.
19. Hung CY, Shimokawa T, Bai Y, Tsuji N, Murayama M. Investigating the dislocation reactions on Σ3{111} twin boundary during deformation twin nucleation process in an ultrafine-grained high-manganese steel. *Sci Rep* 2021;11:19298. DOI PubMed PMC
20. Zhu Q, Kong L, Lu H, et al. Revealing extreme twin-boundary shear deformability in metallic nanocrystals. *Sci Adv* 2021;7:eabe4758. DOI PubMed PMC
21. Wang J, Anderoglu O, Hirth JP, Misra A, Zhang X. Dislocation structures of Σ3 {112} twin boundaries in face centered cubic metals. *Appl Phys Lett* 2009;95:021908.
22. Liu L, Wang J, Gong SK, Mao SX. High resolution transmission electron microscope observation of zero-strain deformation twinning mechanisms in Ag. *Phys Rev Lett* 2011;106:175504. DOI PubMed
23. Li Q, Xue S, Wang J, et al. High-strength nanotwinned Al alloys with 9R phase. *Adv Mater* 2018;30:1704629. DOI PubMed
24. Zhang Y, Li G, Yuan F, et al. Atomic scale observation of FCC twin, FCC→9R and 9R→12R' transformations in cold-rolled Hafnium. *Scripta Materialia* 2022;207:114284.
25. Liebscher C, Radmilović V, Dahmen U, et al. A hierarchical microstructure due to chemical ordering in the bcc lattice: early stages of formation in a ferritic Fe-Al-Cr-Ni-Ti alloy. *Acta Materialia* 2015;92:220-32.
26. Lu W, Herbig M, Liebscher C, et al. Formation of eta carbide in ferrous martensite by room temperature aging. *Acta Materialia* 2018;158:297-312.
27. Wang J, Li N, Anderoglu O, et al. Detwinning mechanisms for growth twins in face-centered cubic metals. *Acta Materialia* 2010;58:2262-70.
28. Zhu Q, Huang Q, Tian Y, et al. Hierarchical twinning governed by defective twin boundary in metallic materials. *Sci Adv* 2022;8:eabn8299. DOI PubMed PMC
29. Tschopp MA, Coleman SP, Mcdowell DL. Symmetric and asymmetric tilt grain boundary structure and energy in Cu and Al (and transferability to other fcc metals). *Integr Mater Manuf Innov* 2015;4:176-89.
30. Zhang Z, Sheng H, Wang Z, et al. Dislocation mechanisms and 3D twin architectures generate exceptional strength-ductility-toughness combination in CrCoNi medium-entropy alloy. *Nat Commun* 2017;8:14390. DOI PubMed PMC
31. Lu L, Shen Y, Chen X, Qian L, Lu K. Ultrahigh strength and high electrical conductivity in copper. *Science* 2004;304:422-6. DOI PubMed
32. Lu L, Chen X, Huang X, Lu K. Revealing the maximum strength in nanotwinned copper. *Science* 2009;323:607-10. DOI PubMed

Zhou *et al. Microstructures* 2022;2:2022018
DOI: 10.20517/microstructures.2022.13

Microstructures

Research Article

Open Access

Check for updates

Tunable negative thermal expansion in $La(Fe, Si)_{13}$/resin composites with high mechanical property and long-term cycle stability

He Zhou[1], Yuwei Liu[1], Rongjin Huang[2], Bo Chen[3], Min Xia[1], Ziyuan Yu[1], Haodong Chen[1], Kaiming Qiao[1], Junzhuang Cong[4], Sergey V. Taskaev[5], Ke Chu[6], Hu Zhang[1]

[1]School of Materials Science and Engineering, University of Science and Technology Beijing, Beijing 100083, China.
[2]State Key Laboratory of Technologies in Space Cryogenic Propellants, Technical Institute of Physics and Chemistry, Chinese Academy of Sciences, Beijing 100049, China.
[3]Key Laboratory of Advanced Civil Engineering Materials (Ministry of Education), School of Materials Science and Engineering, Tongji University, Shanghai 201804, China.
[4]MultiFields Technologies (Beijing) Co. Ltd., Hengxing Building, Zhongguancun, Haidian Dist., Beijing 100190, China.
[5]Physics Faculty, Chelyabinsk State University, Chelyabinsk 454001, Russia.
[6]School of Materials Science and Engineering, Lanzhou Jiaotong University, Lanzhou 730070, Gansu, China.

Correspondence to: Prof. Hu Zhang, School of Materials Science and Engineering, University of Science and Technology Beijing, 30 Xueyuan Road, Haidian District, Beijing 100083, China. E-mail: zhanghu@ustb.edu.cn; Prof. Rongjin Huang, State Key Laboratory of Technologies in Space Cryogenic Propellants, Technical Institute of Physics and Chemistry, Chinese Academy of Sciences, 29 Zhongguancun East Road, Haidian District, Beijing 100049, China. E-mail: huangrongjin@mail.ipc.ac.cn; Dr. Bo Chen, Key Laboratory of Advanced Civil Engineering Materials (Ministry of Education), School of Materials Science and Engineering, Tongji University, 1239 Siping Road, Shanghai 201804, China. E-mail: bo.chen@tongji.edu.cn

How to cite this article: Zhou H, Liu Y, Huang R, Chen B, Xia M, Yu Z, Chen H, Qiao K, Cong J, Taskaev SV, Chu K, Zhang H. Tunable negative thermal expansion in $La(Fe, Si)_{13}$/resin composites with high mechanical property and long-term cycle stability. *Microstructures* 2022;2:2022018. https://dx.doi.org/10.20517/microstructures.2022.13

Received: 8 Jun 2022 **First Decision:** 14 Jul 2022 **Revised:** 4 Aug 2022 **Accepted:** 15 Aug 2022 **Published:** 17 Aug 2022

Academic Editors: Xiaozhou Liao, Yuzhu Song, Andrea Sanson **Copy Editor:** Fangling Lan **Production Editor:** Fangling Lan

Abstract

Materials with tunable negative thermal expansion (NTE) are highly demanded in various functional devices. $La(Fe, Si)_{13}$-based compounds are promising NTE materials due to their outstanding NTE properties. However, their poor mechanical properties and related short service life restrict their practical applications. In this work, epoxy resin with positive thermal expansion is used to synthesize La-Fe-Si/resin composites. The NTE of La-Fe-Si/resin composites can be manipulated by optimizing the La-Fe-Si particle size and resin content, and tailoring resin content could tune the NTE more effectively. The average linear coefficient of thermal expansion of the composites decreases from -275.0×10^{-6} K^{-1} to -4.9×10^{-6} K^{-1} over the magnetic transition temperature range as the resin

content increases from 3 wt.% to 80 wt.%. In addition, zero thermal expansion is achieved in the La-Fe-Si/resin composite with 20 wt.% resin. The resin would reinforce the binding force by filling the pores between the particles. The La-Fe-Si/resin composite with 80 wt.% resin exhibits highly improved mechanical properties; for example, its compressive strength of 205 MPa is 75% higher than that of the La-Fe-Si/resin composite with 3 wt.% resin. The prepared La-Fe-Si/resin composites can be machined into different shapes for practical applications, such as thin plates, strips, and rods. Furthermore, the La-Fe-Si/resin composites can undergo 1000 thermal cycles without NTE performance degradation and mechanical integrity loss, indicating durable cycle stability. Hence, significantly tunable NTE with high mechanical properties and long-term cycle stability makes La-Fe-Si/resin composites present great application potential as NTE materials.

Keywords: Negative thermal expansion (NTE), La-Fe-Si compounds, mechanical properties

INTRODUCTION

Most materials exhibit positive thermal expansion (PTE). However, various functional devices require precisely tailored thermal expansion or even zero thermal expansion (ZTE), such as high-precision optical mirrors, fiber reflective gratings, and printed circuit boards[1]. Therefore, materials with negative thermal expansion (NTE) have attracted increasing attention. This unusual volumetric effect can be used to regulate the coefficient of thermal expansion (CTE) and produce ZTE composites by mixing them with PTE materials. So far, a few kinds of materials have been reported as potential NTE material candidates, such as ZrW_2O_8[2], antiperovskite manganese nitrides[3], $AgB(CN)_4$[4], MM′X compounds[5], β-$Cu_{1.8}Zn_{0.2}V_2O_7$[6], (Hf, Nb)Fe_2[7], ScF_3-based compounds[8], and $PbTiO_3$-based compounds[9]. Nonetheless, most NTE materials cannot be used as thermal expansion compensators in practice because of their low NTE coefficient, limited NTE temperature window, and poor mechanical properties.

La(Fe, Si)$_{13}$-based compounds with a cubic $NaZn_{13}$-type structure (space group *Fm*3*c*) have been widely studied because of their giant magnetocaloric effect (MCE) and the application potential in magnetic refrigeration[10-12]. The large MCE of La(Fe, Si)$_{13}$-based compounds primarily originates from their itinerant electron metamagnetic (IEM) transition, that is, a field-induced first-order magnetic transition from the paramagnetic (PM) to ferromagnetic (FM) states[13]. Furthermore, La(Fe, Si)$_{13}$-based compounds have large magnetovolume effect (MVE); namely, the magnetic transition is accompanied by a distinct NTE behavior around the Curie temperature (T_C)[14]. Therefore, their isotropic and remarkable NTE suggests that La(Fe, Si)$_{13}$-based compounds could be excellent NTE materials for applications.

The NTE properties of La(Fe, Si)$_{13}$-based compounds have been reported in recent years. For example, the $LaFe_{10.5}Co_{1.0}Si_{1.5}$ compound exhibits a large NTE in a wide operation temperature window of 110 K, and its linear NTE coefficient reaches -26.1 × 10^{-6} K^{-1}[15]. However, previous research primarily focused on tuning the NTE properties of the La(Fe, Si)$_{13}$-based compounds by composition manipulation[16-19], while neglecting their poor mechanical properties. The intrinsic brittleness of La(Fe, Si)$_{13}$-based compounds will result in difficulty in shaping and machining them. Furthermore, their large NTE tends to cause fractures, causing materials and devices to fail[20]. These shortcomings significantly limit the application potential of La(Fe, Si)$_{13}$-based compounds as NTE materials. However, La(Fe, Si)$_{13}$ composites would be ideal candidates for NTE materials if excellent mechanical properties are obtained. Previous work has shown that epoxy resin-bonded magnetocaloric composites exhibit well-improved mechanical properties[21]. Since the epoxy resin exhibits PTE behavior [Supplementary Figure 1], it could be an effective way to obtain tunable NTE as well as high mechanical performance by producing the La(Fe, Si)$_{13}$/resin composites.

In this work, the $La_{0.7}Ce_{0.3}Fe_{11.51}Mn_{0.09}Si_{1.4}$ compound with strong first-order magnetic transition is chosen as an origin NTE material (hereafter refers to La-Fe-Si). Epoxy resin-bonded La-Fe-Si composites were successfully fabricated. The NTE of the La-Fe-Si/resin composites is manipulated by controlling the La-Fe-Si particle size and epoxy resin content. Reducing the particle size will weaken the first-order magnetic transition of the $La_{0.7}Ce_{0.3}Fe_{11.51}Mn_{0.09}Si_{1.4}$ compound, thereby decreasing the NTE of the composites. Tailoring the resin content is a more effective way to tune the NTE of La-Fe-Si/resin composites. The NTE of La-Fe-Si/resin composites gradually decreases as the resin content increases. The La-Fe-Si/resin composite with 20 wt.% resin exhibits ZTE behavior in a wide temperature range. Importantly, the La-Fe-Si/resin composites exhibit high mechanical properties and can maintain mechanical integrity and functional stability after 1000 thermal cycles. As a result, La-Fe-Si/resin composites with tunable NTE, excellent mechanical properties, and long-term cycle stability present great application potential as NTE materials.

MATERIALS AND METHODS

Sample preparation

$La_{0.7}Ce_{0.3}Fe_{11.51}Mn_{0.09}Si_{1.4}$ ingot was prepared by induction melting. Then, the ingot was processed into ribbons using the melt-spinning method. The ribbons were subsequently sealed in a quartz tube with an argon atmosphere and annealed at 1393 K for 20 h, followed by ice water quenching. A schematic illustration of $La_{0.7}Ce_{0.3}Fe_{11.51}Mn_{0.09}Si_{1.4}$ powder preparation is shown in Supplementary Figure 2A. The phase composition of the $La_{0.7}Ce_{0.3}Fe_{11.51}Mn_{0.09}Si_{1.4}$ compound is primarily 1:13 phase, accompanied by a very small amount of the α-Fe phase and La-rich phase [Supplementary Figure 2B and C]. The annealed $La_{0.7}Ce_{0.3}Fe_{11.51}Mn_{0.09}Si_{1.4}$ ribbons were broken and ground into powders by hand using an agate mortar. Then, the powders were separated into different groups according to their particle sizes using sieves as follows: 280-450 μm, 200-280 μm, 150-200 μm, 75-150 μm, 40-75 μm and < 10 μm. The particle size distribution of these powders was then re-checked by scanning electron microscopy (SEM). As shown in Supplementary Figure 3, the size distribution of these particles obtained from the SEM micrographs of these $La_{0.7}Ce_{0.3}Fe_{11.51}Mn_{0.09}Si_{1.4}$ powders is 397.9, 278.0, 180.4, 96.6, 45.2 and 3.6 μm, respectively (hereafter refers to P398, P278, P180, P97, P45, and P4). The $La_{0.7}Ce_{0.3}Fe_{11.51}Mn_{0.09}Si_{1.4}$ powders were mixed with multiple-component epoxy resin composed of E51 epoxy resin and T31 Mannich amide. The resin-mixed powders were pressed into cylinders of Φ10 mm under a pressure of 900 MPa and then solidified at room temperature for five days. Note that the resin must be precured before pressing for the composites with high resin content to prevent the resin from flowing out of the mold during pressing. The density of these La-Fe-Si/resin composites was estimated using the Archimedes method[12].

Sample characterization

The temperature-variation X-ray diffraction (XRD) measurement was performed by using Cu *Kα* radiation. The Rietveld refinement was performed on these XRD patterns to identify the phase composition and their crystal structure using the GSAS/EXPGUI software[22]. The microstructure was recorded by SEM, and elemental analysis was performed using energy-dispersive spectroscopy (EDS) equipped with SEM. The three-dimensional (3D) spatial distribution of the different phases of the samples was revealed by using high-resolution X-ray computed tomography (CT). The segmentation and quantitative analysis of the 3D structural images were performed using the Avizo software[23]. Compressive strength was measured by using cylindrical samples of Φ10 × 10 mm by a universal testing machine under ambient temperature. Magnetic measurements were performed using a vibrating sample magnetometer (VSM, Quantum Design, VersaLab). The differential scanning calorimetry (DSC) measurements were carried out using DSC 6220 with a ramp rate of 10 K/min. The linear thermal expansion ($\Delta L/L$) was measured using a thermo-dilatometer with a heating rate of 2 K/min.

RESULTS AND DISCUSSION

Tunable NTE via adjusting particle size

The NTE of La(Fe, Si)$_{13}$ compounds is closely related to the magnetic transition. The thermal and magnetic hysteresis decrease gradually with reducing particle size [Supplementary Figures 4 and 5], which implies the weakening of the first-order magnetic transition. The reduction in thermal and magnetic hysteresis can be ascribed to the partially-removed internal strain and grain boundaries as well as the significantly increased specific surface areas of the samples [Supplementary Figures for detailed analysis]. The weakening of first-order magnetic transition can also be confirmed by the Arrott plots [Supplementary Figure 6]. Moreover, the magnetic entropy change (ΔS_M) decreases gradually with reducing particle size owing to the weakening of the first-order magnetic transition [Supplementary Figure 7]. The maximum -ΔS_M value of the ribbon samples can reach as high as 21.5 J/kg K under a low magnetic field change of 0-1 T, and the La-Fe-Si powders with an average particle size of ~4 μm can still exhibit a giant magnetic entropy change of 10.1 J/kg K. This implies the strong first-order magnetic transition of the $La_{0.7}Ce_{0.3}Fe_{11.51}Mn_{0.09}Si_{1.4}$ compound. The strong first-order magnetic transition enables the La-Fe-Si compound to exhibit excellent NTE properties. The average CTE of the La-Fe-Si compound obtained from the temperature-variation XRD can reach -76.4 × 10^{-6} K^{-1} in the NTE region from 100 K to 180 K [Supplementary Figure 8].

To optimize the NTE properties of the La-Fe-Si/resin composites, 3 wt.% epoxy resin was mixed with the $La_{0.7}Ce_{0.3}Fe_{11.51}Mn_{0.09}Si_{1.4}$ powders of different particle sizes to produce a series of composites. The backscattered electron (BSE) image of a fabricated La-Fe-Si/resin composite with 3 wt.% resin and the corresponding elemental mapping of La, Ce, Fe, Mn, Si and C elements are shown in Supplementary Figure 9. La, Ce, Fe, Mn and Si elements are homogeneously distributed in the $La_{0.7}Ce_{0.3}Fe_{11.51}Mn_{0.09}Si_{1.4}$ particles, and the C originates from the epoxy resin. Figure 1A shows the BSE images of the P398, P278, P180, P97, P45 and P4 composites. The La-Fe-Si particle size gradually decreases in the P398 to P4 samples. The epoxy resin (black areas) with high fluidity is uniformly distributed around the particle boundaries and among their narrow gaps. The composites exhibit a denser microstructure with reduced particle sizes. Reducing the particle size could increase the surface area of the particles, so particles with smaller sizes can contact with the epoxy resin by a larger surface area, and hence, the total bonding force between La-Fe-Si particles and resin is enhanced. Namely, the La-Fe-Si/resin composites with smaller particle sizes have a denser structure in the case of the same amount of epoxy resin used. Moreover, a dense structure improves NTE and the mechanical properties of the La-Fe-Si/resin composites. The BSE and secondary electron (SE) images of the P180 composite are shown in Supplementary Figure 10. The resin regions and pores are present as black areas in the BSE image, but from the SE image, the pores are darker and bigger areas than the resin regions. The distribution of pores and resin will be further distinguished later by elemental mapping. To further study the densification of La-Fe-Si/resin composites with different particle sizes, the porosity of La-Fe-Si/resin composites with different particle sizes can be estimated using the following equation: porosity = $(\rho_{the} - \rho_{exp})/\rho_{the}$, where ρ_{the} and ρ_{exp} represent theoretical density and experimental density, respectively; ρ_{the} is calculated by $\rho_{the} = \rho_{La\text{-}Fe\text{-}Si}$ × La-Fe-Si content + ρ_{resin} × resin content, whereas ρ_{exp} is obtained using the Archimedes method. Figure 1B displays the porosity of La-Fe-Si/resin composites with different particle sizes. As the particle size decreases, the porosity of the composites first decreases from P398 to P180 samples, and then, porosity increases with reducing particle size. As mentioned above, the increasing surface areas of particles caused by the reduction in particle size can improve the densification of composites, thereby decreasing porosity at first. Nevertheless, while further reducing the particle size, the particles with smaller sizes are more likely to agglomerate during mixing. As shown in Figure 1A, fine La-Fe-Si particles with an average diameter of ~4 μm tend to clump together, forming many large epoxy resin regions in the La-Fe-Si/resin composites. In addition, with an increase in surface areas, more resin is required to cover all particle surfaces. Therefore, 3 wt.% epoxy resin may not be sufficient to cover the surface of all La-Fe-Si particles to bond them, thus leading to the formation of more pores. Consequently, once the average particle size is smaller than 180 μm, the porosity of composites

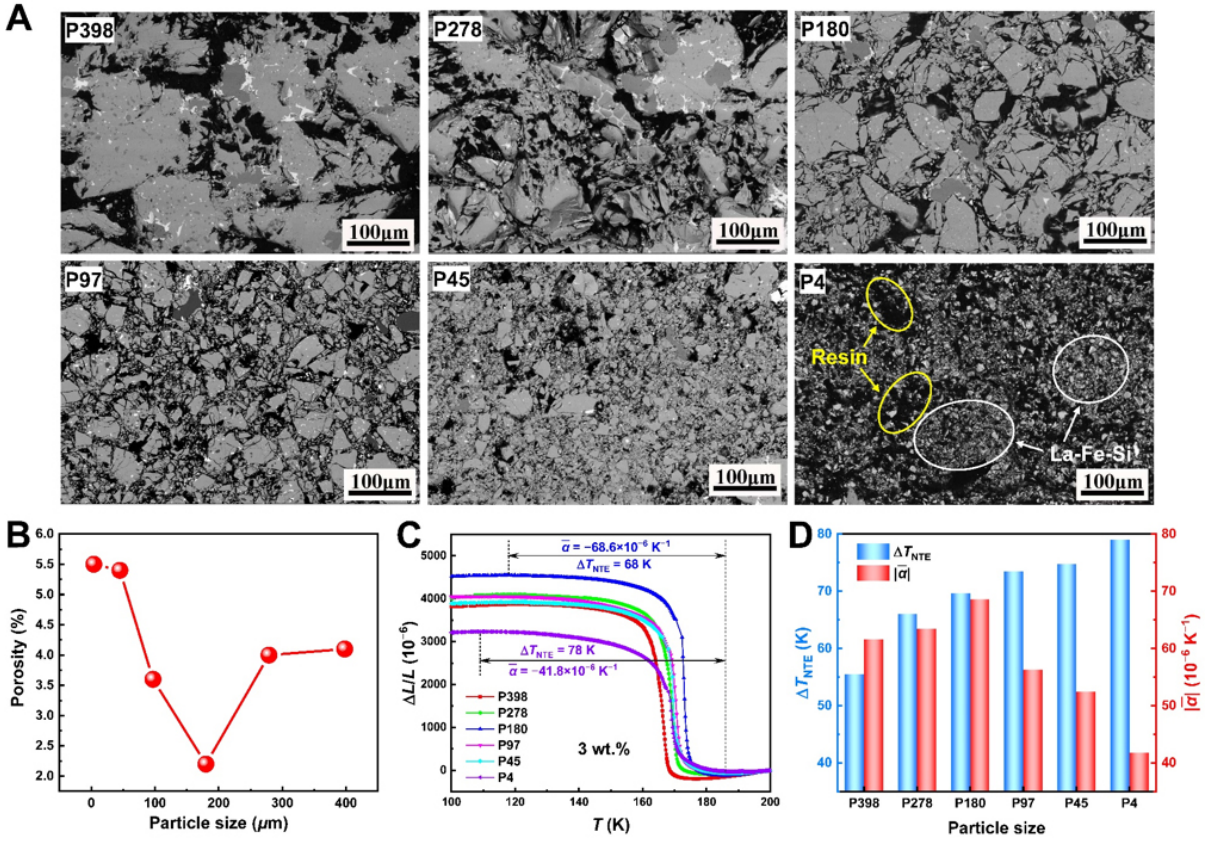

Figure 1. (A) BSE images of La-Fe-Si/resin composites with different particle sizes; (B) porosity of La-Fe-Si/resin composites with different particle sizes; (C) temperature dependence of linear thermal expansion ($\Delta L/L$) for La-Fe-Si/resin composites with different particle sizes; (D) NTE temperature range and average linear NTE coefficient of La-Fe-Si/resin composites with different particle sizes. BSE: Backscattered electron; NTE: negative thermal expansion.

increases with the further reduction in particle size.

Figure 1C presents the temperature dependence of the linear thermal expansion ($\Delta L/L$) of the La-Fe-Si/resin composites with 3 wt.% resin content with different particle sizes (the reference temperature is 200 K). The linear thermal expansion increases as the temperature decreases, which indicates the NTE of the La-Fe-Si/resin composites. Furthermore, the NTE property varies distinctly with the reduction in particle size. The NTE temperature region (ΔT_{NTE}) in which the composites exhibit NTE behavior and the average linear coefficient of thermal expansion ($\bar{\alpha} = \frac{(\Delta L/L)_{T_2} - (\Delta L/L)_{T_1}}{T_2 - T_1}$) in the ΔT_{NTE} as a function of particle size are shown in Figure 1D. ΔT_{NTE} increases monotonously with reducing particle size. As mentioned above, reducing particle size will weaken the first-order magnetic transition of the $La_{0.7}Ce_{0.3}Fe_{11.51}Mn_{0.09}Si_{1.4}$ compound. Therefore, the magnetic transition will become less sharp; that is, the transition temperature window will be widened. Unlike the monotonous variation of ΔT_{NTE}, $\bar{\alpha}$ first increases gradually with the reduction in particle size while the average particle size is larger than 180 μm. However, $\bar{\alpha}$ decreases remarkably with the reduction in particle size as the particle size is further reduced, which is consistent with the opposite variation trend of porosity [Figure 1B]. We assume that the reduction in particle size would lead to two effects on the NTE of La-Fe-Si/resin composites. First, the first-order magnetic transition will be weakened by reducing the particle size, thereby leading to a lower $\bar{\alpha}$; second, the reduction in particle size decreases or

increases porosity [Figure 1B], which would then increase or decrease $\bar{\alpha}$. When the average particle size is larger than 180 μm, the reduction in particle size weakens the first-order magnetic transition as well as lowers porosity, which has opposite effects on the NTE of La-Fe-Si/resin composites. The increase in $\bar{\alpha}$ implies that the latter factor plays a predominant role. When the particle size is further reduced to lower than 180 μm, both weakening of first-order magnetic transition and an increase in porosity will lower the NTE of La-Fe-Si/resin composites, thereby decreasing $\bar{\alpha}$. This result suggests that porosity is a more important factor that affects the NTE of La-Fe-Si/resin composites. Among the composites, the P180 composite exhibits the highest NTE property because it has the lowest porosity. Its $\bar{\alpha}$ is estimated to be -68.6 × 10^{-6} K^{-1} in the NTE temperature region from 120 to 185 K, which can be comparable to those of some typical NTE materials, such as $Fe_{41.5}Mn_{28}Ga_{30.5}$ (-59.8 × 10^{-6} K^{-1}, 136-220 K)[24], $LaFe_{11.2}Al_{1.3}Si_{0.5}$ (-28.3 × 10^{-6} K^{-1}, 150-200 K)[25], $Mn_{0.97}In_{0.03}CoGe$ (-66.6 × 10^{-6} K^{-1}, 58-230 K)[5], and $Ag_{0.5}NMn_{3.5}$ (-5.14 × 10^{-6} K^{-1}, 135-185 K)[26]. When the average particle size decreases to ~4 μm, the P4 composite can still obtain a large $\bar{\alpha}$ of -41.8 × 10^{-6} K^{-1}. These results demonstrate that controlling the particle size is an effective way to tune the NTE of La-Fe-Si/resin composites. However, by only tuning the La-Fe-Si particle size, it is very difficult to reach precisely tailored NTE properties, and a ZTE case can barely be achieved.

Microstructure of La-Fe-Si/resin composites

Owing to the excellent NTE performance of the P180 composite, the P180 powder is chosen to further optimize La-Fe-Si/resin composites with different resin contents to better tune their NTE and to obtain ZTE composites. The proportions of the epoxy resin are 3, 10, 20, 30, 40, 50, 60, 70 and 80 wt.%, respectively (hereafter refers to Resin3, Resin10, Resin20, Resin30, Resin40, Resin50, Resin60, Resin70, and Resin80). The La-Fe-Si/resin composites are composed of La-Fe-Si phase and resin, and no impurity phase is observed, indicating that the pressing process does not cause the instability of the La-Fe-Si phase [Supplementary Figure 11]. Figure 2A shows the optical morphologies of La-Fe-Si/resin composites with different resin contents. As shown in the magnified image of the Resin80 composite, the white areas represent $La_{0.7}Ce_{0.3}Fe_{11.51}Mn_{0.09}Si_{1.4}$ particles, and the gray areas represent the epoxy resin. The composite gradually changes from metallic luster to a transparent state when the epoxy resin content increases from 3 wt.% to 80 wt.%, indicating that the matrix of La-Fe-Si/resin composites changes from La-Fe-Si powders to epoxy resin. When the epoxy resin content is 3 wt.%, the epoxy resin is used as a binder to bond La-Fe-Si particles. Conversely, when the epoxy resin content is more than the La-Fe-Si content, the epoxy resin will wrap La-Fe-Si particles; that is, La-Fe-Si particles are evenly distributed in the resin matrix. This structure can increase the densification of La-Fe-Si/resin composites, thereby improving their mechanical properties. In addition, the DSC curves of La-Fe-Si powders and La-Fe-Si/resin composites indicate that the La-Fe-Si powders and composites with different resin contents exhibit consistent DSC peaks, which implies that the epoxy resin will not affect the first-order magnetic transition of La-Fe-Si compound. However, the Resin20 and Resin80 composites show wider DSC peaks, which may be attributed to the poor thermal conductivity of the Resin20 and Resin80 composites [Supplementary Figure 12].

Figure 2B shows the BSE images of La-Fe-Si/resin composites with different resin contents. The gray areas represent the La-Fe-Si phase, and the black areas represent the epoxy resin and pores. La-Fe-Si particles have a homogeneous particle size, and the epoxy resin is primarily distributed among La-Fe-Si particles because of high fluidity. Moreover, La-Fe-Si particles are uniformly distributed in the epoxy resin matrix without segregation. When the resin content reaches 80 wt.%, the resin will become the matrix of La-Fe-Si/resin composites, whereas La-Fe-Si particles will be the additive phase. Therefore, the La-Fe-Si/resin composite is presumed to exhibit positive thermal expansion.

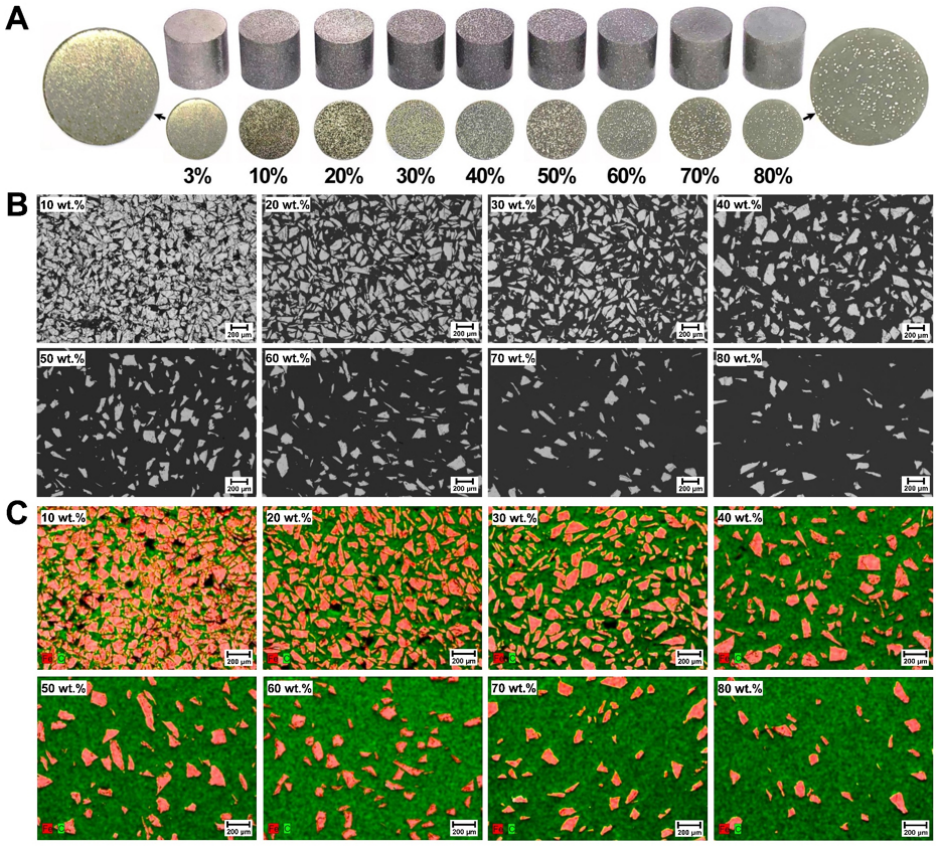

Figure 2. (A) Images of La-Fe-Si/resin composites with different resin contents; (B) BSE images of La-Fe-Si/resin composites with different resin contents; (C) elemental mapping of Fe and C for La-Fe-Si/resin composites with different resin contents. BSE: Backscattered electron.

Since both the epoxy resin and pores are represented as black areas in the obtained SEM images, to further distinguish the epoxy resin and pores, the elemental mapping of Fe and C in La-Fe-Si/resin composites is performed and shown in Figure 2C. The orange areas (Fe element) represent $La_{0.7}Ce_{0.3}Fe_{11.51}Mn_{0.09}Si_{1.4}$ particles, the green areas (C element) represent the epoxy resin, and the black areas represent the pores. A large number of pores can be observed in the Resin10 composite, and these pores are primarily distributed in the particle boundaries. With an increase in resin content, the number of pores gradually decreases and eventually disappears when the resin content is greater than 30 wt.%. For La-Fe-Si/resin composites, increasing epoxy resin content will fill more pores during compressing, thereby decreasing porosity and improving densification. Such a compact structure improves mechanical and NTE properties. Moreover, during the SEM sample preparation, sanding may cause La-Fe-Si particles to fall off the La-Fe-Si/resin composites, leading to the appearance of pores in the La-Fe-Si/resin composites. With increasing resin content, the disappearance of pores further indicates the enhancement of the bonding force between the epoxy resin and La-Fe-Si particles.

High-resolution X-ray CT is performed to further investigate the internal spatial structure of La-Fe-Si/resin composites. Figure 3A-C show the 3D rendered volume images of each component for Resin3, Resin20 and Resin80 composites, respectively. A central region with a volume of 1000 × 1000 × 1000 μm^3 of the sample was chosen for 3D rendering and analysis. The blue parts represent La-Fe-Si particles, the red parts represent the epoxy resin, and the green parts represent pores. The leftmost full 3D structural images in

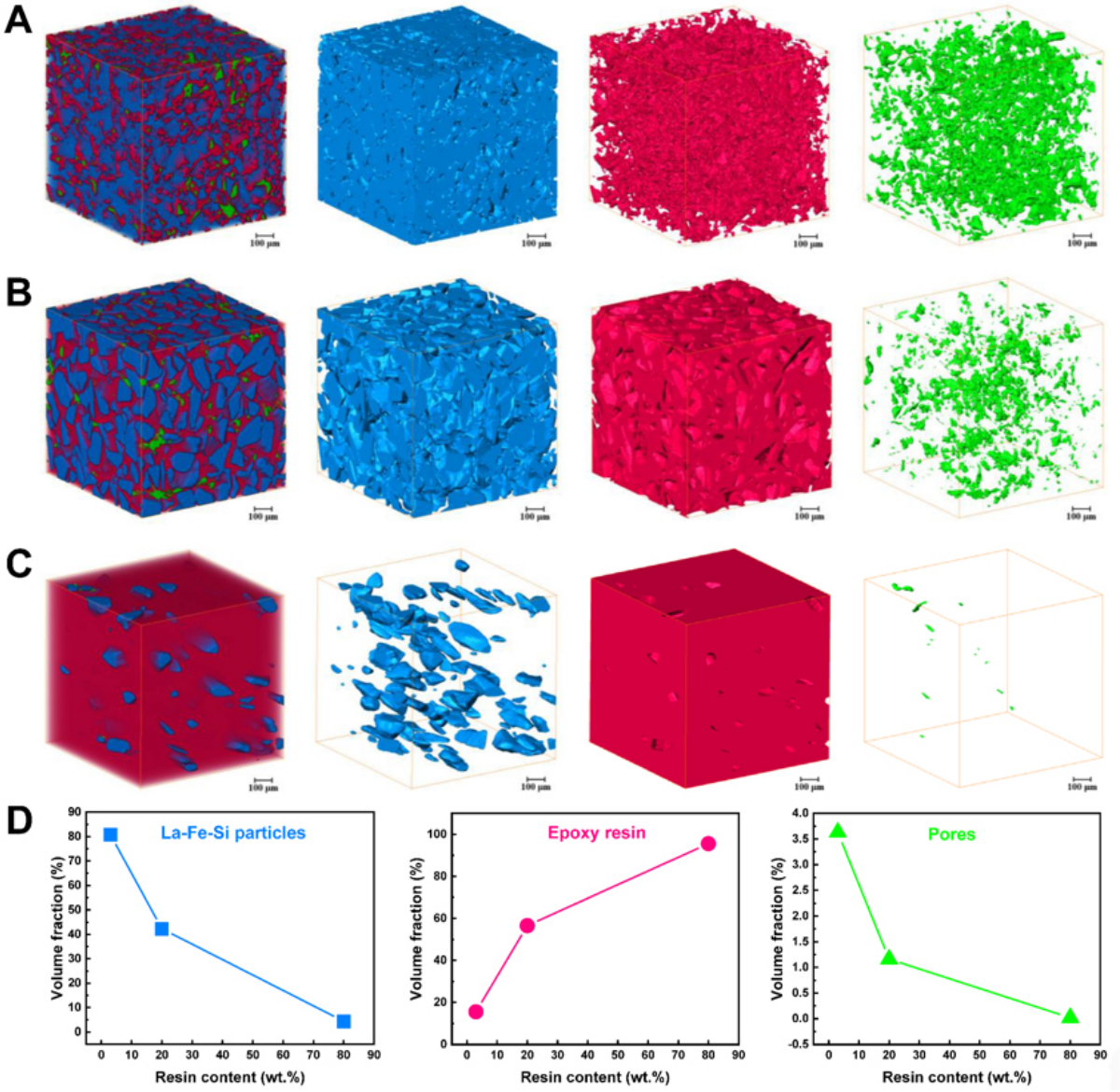

Figure 3. 3D rendering images of each phase for (A) Resin3; (B) Resin20; and (C) Resin80 composites. From left to right: the overlapping configuration, La-Fe-Si phase, epoxy resin and pores; (D) volume fraction of La-Fe-Si particle, epoxy resin and pore.

Figure 3A-C show that the resin (red region) tends to be among La-Fe-Si particles (blue region) and dispersive pores (green region). The stereo structure of La-Fe-Si particles, resin and pores reveals the homogeneity of the spatial structure. For the Resin3 composite, the resin exists in an irregular shape due to high fluidity. With increasing resin content, the resin will wrap La-Fe-Si particles and further fill the pores. According to the quantitative analysis of the Avizo software, the volume fraction of each component in the composites is obtained and shown in Figure 3D. The volume fractions of the epoxy resin in Resin3, Resin20 and Resin80 composites are 15.54 %, 56.55 % and 95.57 %, respectively. Since the epoxy resin exhibits PTE behavior, an increase in resin fraction would lower the NTE of the La-Fe-Si/resin composites, exhibiting ZTE behavior at a certain resin content. In addition, further resin addition will fill the pores, improving densification; for example, the porosity of the Resin3, Resin20 and Resin80 composites is determined to be 3.63%, 1.16% and 0.02%, respectively. The denser the structure of La-Fe-Si/resin composites, the better their

mechanical properties.

High mechanical properties

Figure 4A presents the compressive stress-strain curves of the Resin3, Resin20, and Resin80 composites. Note that the stress-strain curve of the pure $La_{0.7}Ce_{0.3}Fe_{11.51}Mn_{0.09}Si_{1.4}$ compound cannot be obtained because it is in the form of ribbons. According to previous reports, the compressive stress-strain curves of bulk La-Fe-Si compounds drop sharply without further plastic deformation[27], indicating the brittleness of these compounds. Nevertheless, the Resin3 composite exhibits a short yield stage before reaching the maximum compressive strength [Figure 4A], which is due to the densification of the porous architecture under stress. With increasing resin content, more pores can be filled, thereby reinforcing the binding force between La-Fe-Si particles. As a result, the compressive strength increases gradually with increasing resin content. The Resin80 composite exhibits compressive strength of 205 MPa, which is 75% higher than that of the Resin3 composite. The enhanced mechanical properties guarantee the integration of materials when La-Fe-Si/resin composites are used as NTE materials. Moreover, the obtained Resin20 composite can be easily machined into different shapes for practical applications, such as thin plates, strips, and rods, as shown in Figure 4B. In addition, Figure 4C shows the temperature dependence of thermal conductivity for Resin3 composite. It can be found that the Resin3 composite shows relatively high thermal conductivity, which can be comparable with some pure La(Fe, $Si)_{13}$-based compounds[15,28]. This facilitates the practical application of the composites as NTE materials.

Tunable NTE via adjusting resin contents

Figure 5A presents the temperature dependence of linear thermal expansion ($\Delta L/L$) for La-Fe-Si/resin composites with different resin contents. With increasing resin contents, La-Fe-Si/resin composites exhibit a distinct decrease in NTE, which is more remarkable than that tuned by particle size as observed in Figure 1C. The $\Delta L/L$ below T_C gradually changes from a large positive value to a large negative value, which confirms our speculation that the resin with PTE will compensate for the NTE of La-Fe-Si particles, thereby gradually tuning La-Fe-Si/resin composites from NTE materials to PTE materials. This result also proves that adjusting the resin content is more effective for adjusting the NTE of La-Fe-Si/resin composites than adjusting the La-Fe-Si particle size. Note that the Resin20 composite exhibits ZTE behavior in a wide temperature range below T_C. The $\bar{\alpha}$ of the Resin20 composite is estimated to be 0.8×10^{-6} K^{-1} in the temperature range of 100-165 K, which is comparable to other ZTE materials, such as $LaFe_{10.0}Si_{3.0}C_{0.4}$ (-0.4×10^{-6} K^{-1}, 120-229 K)[29], $Gd_{0.25}Dy_{0.75}Co_{1.93}Fe_{0.07}$ (-0.61×10^{-6} K^{-1}, 98-270 K)[30] and $Tb(Co_{1.9}Fe_{0.1})$ (0.48×10^{-6} K^{-1}, 123-307 K)[31]. Although composites with high resin content exhibit a distinct PTE behavior below T_C, the NTE property can still be observed around T_C, even in the Resin80 composite. The $\bar{\alpha}$ of the Resin80 composite is -8.1×10^{-6} K^{-1} in the NTE temperature range from 168 K to 180 K. This fact suggests the strong intrinsic NTE property of La-Fe-Si compound due to the magnetic transition from the PM phase with a small lattice to the FM phase with a large lattice.

Figure 5B shows the NTE temperature region as a function of the resin content. The wide NTE temperature region from 118 K to 186 K for the Resin3 composite indicates that the $La_{0.7}Ce_{0.3}Fe_{11.51}Mn_{0.09}Si_{1.4}$ compound not only exhibits a significant NTE property around T_C, but also exhibits NTE behavior in a wide temperature range below T_C. This NTE below T_C can be confirmed by the variation of $\Delta a/a$ as shown in Supplementary Figure 8C. This fact also suggests that there still exists strong magnetoelastic coupling below T_C for the $La_{0.7}Ce_{0.3}Fe_{11.51}Mn_{0.09}Si_{1.4}$ compound. With increasing resin content, the lower limit temperature of NTE increases largely, whereas the upper limit temperature gradually decreases. In particular, the NTE temperature range decreases significantly from 68 K for the Resin3 composite to 19 K for the Resin30 composite. The significant increase in the lower limit temperature suggests that the NTE below T_C caused by

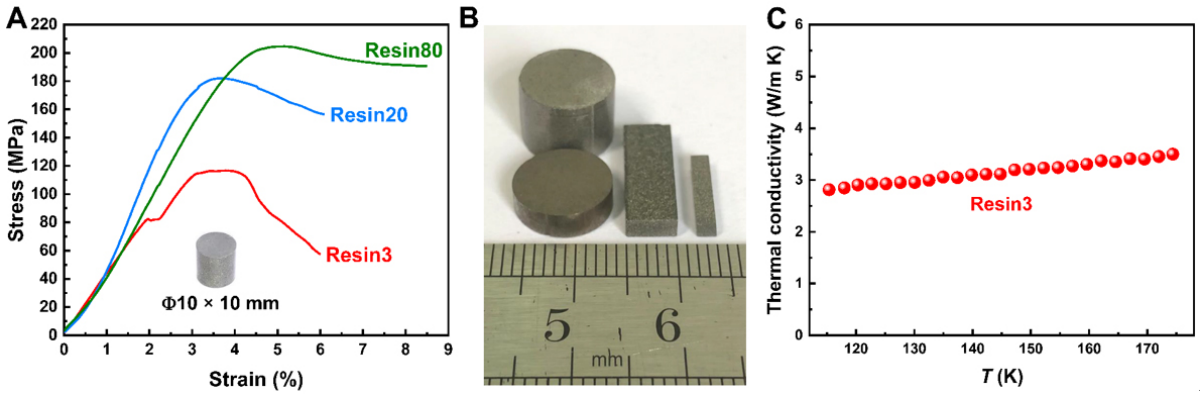

Figure 4. (A) Compressive stress-strain curves for Resin3, Resin20 and Resin80 composites; (B) different shapes machined from the Resin20 composite; (C) temperature dependence of thermal conductivity for Resin3 composite.

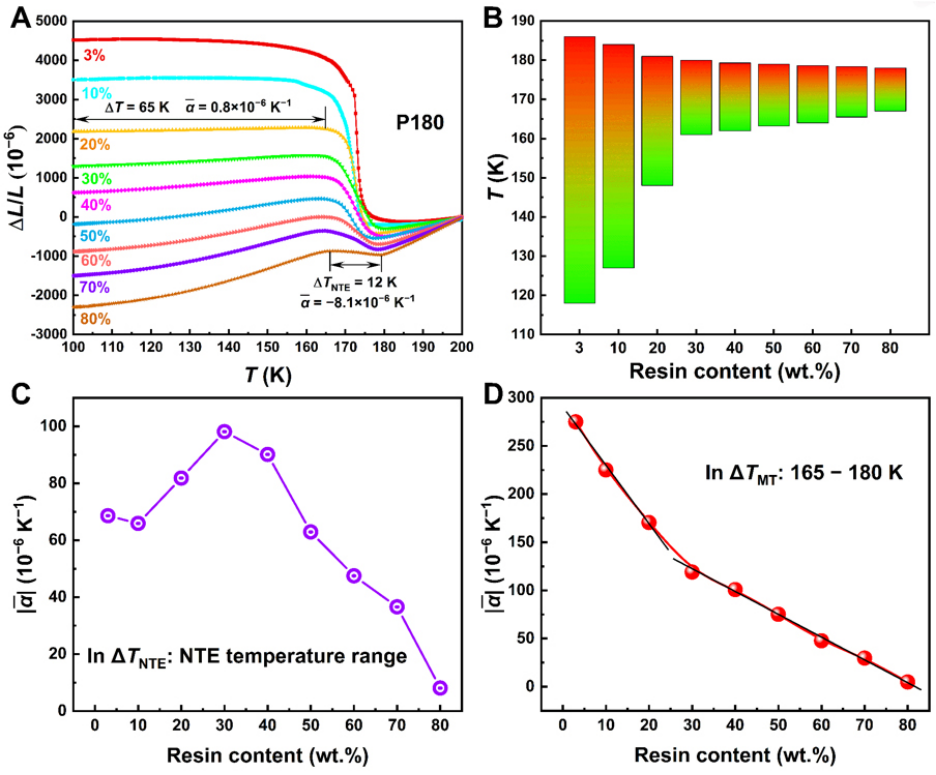

Figure 5. (A) Temperature dependence of linear thermal expansion ($\Delta L/L$) for La-Fe-Si/resin composites with different resin contents; (B) NTE temperature range as a function of resin content; Average linear NTE coefficient as a function of resin content in the (C) NTE temperature range and (D) magnetic transition temperature range. NTE: Negative thermal expansion.

the magnetoelastic coupling is compensated by the PTE of the resin. However, the NTE originating from the magnetic transition is significantly stronger; thus, the NTE temperature region remains until the resin content even reaches 80 wt.%.

Figure 5C shows the average NTE coefficient of La-Fe-Si/resin composites with different resin contents in their respective NTE temperature ranges (ΔT_{NTE}). The average NTE coefficient of the La-Fe-Si/resin composites increases and then decreases with increasing resin content. Similarly, an increase in resin

content also has two opposite effects on the average NTE coefficient. First, increasing the resin content can improve the densification of composites, thereby improving NTE; second, the PTE of the epoxy resin will compensate for the NTE of La-Fe-Si particles, decreasing NTE. This result suggests that the first effect plays a predominant role if the resin content is lower than 30 wt.%, whereas the second effect becomes more prominent if the resin content is higher than 30 wt.%. Furthermore, the average NTE coefficient of the La-Fe-Si/resin composites with different resin contents in the magnetic transition temperature range (ΔT_{MT}: 165-180 K) is determined to further investigate the variation of NTE during the phase transition, as shown in Figure 5D. $\bar{\alpha}$ first decreases significantly from -275.0 × 10^{-6} K^{-1} for the Resin3 composite to -119.0 × 10^{-6} K^{-1} for the Resin30 composite, and then, the slope becomes lower, and $\bar{\alpha}$ decreases gradually to -4.9 × 10^{-6} K^{-1} for the Resin80 composite. As mentioned above, the PTE of the resin and pores in the composites can weaken the NTE of the composites. Figure 2C shows that the number of pores gradually decreases as the resin content increases; for example, porosity decreases from the Resin3 composite's 3.63% to the Resin20 composite's 1.16% [Figure 3D]. Then, the pores in the composites almost disappear [Figure 2C]. This reveals that the NTE of La-Fe-Si/resin composites will be less affected by pores if the resin content is more than 20 wt.%, thereby leading to the change of slope. In addition, although the resin has become the matrix of the La-Fe-Si/resin composites when the resin content reaches 80 wt.%, the Resin80 composite still exhibits significant NTE in the magnetic transition temperature range. This result further proves the strong intrinsic NTE properties of the $La_{0.7}Ce_{0.3}Fe_{11.51}Mn_{0.09}Si_{1.4}$ compound during the PM-FM magnetic transition. Furthermore, the theoretical thermal expansion of La-Fe-Si/resin composites with different resin contents can be obtained based on the thermal expansion of the epoxy resin and La-Fe-Si compound [Supplementary Figure 13A]. Then, the coefficient of thermal expansion of La-Fe-Si/resin composites with different resin contents can be calculated. The experimental and theoretical values of coefficients of thermal expansion of the composites in the magnetic transition temperature range are shown in Supplementary Figure 13B. It can be seen that both theoretical and experimental values gradually decrease with the increase of resin content. Moreover, the experimental values are lower than the theoretical values. The thermal expansion obtained from the temperature-variation XRD measurement may deviate from the actual thermal expansion of the La-Fe-Si compound. In addition, the existence of pores in the composites will affect the thermal expansion of the composites. Therefore, the experimental values of coefficients of thermal expansion are different from the theoretical values.

Long-term cycle stability

The strong NTE behavior, particularly the remarkable NTE during the magnetic transition, can cause microcracks in La-Fe-Si/resin composites during their cycling service due to the repeated shrinkage and expansion, leading to material failure. Therefore, long-term cycle stability is a vital prerequisite for the applications of NTE materials. Here, the Resin3 composite is chosen to conduct the thermal cycle test around the transition temperature. As shown in Figure 6A, the Resin3 composite is thermally cycled in liquid nitrogen and hot water (~358 K) to investigate its cycle stability. Figure 6B shows that the Resin3 composite still maintains decent integrity after 1000 thermal cycles, which means that it has excellent mechanical properties. Figure 6B shows the surface morphology obtained by optical microscopy and SEM before and after 1000 thermal cycles. After undergoing 1000 thermal cycles, the Resin3 composite maintains its original macro- and micro-structure without significant differences and does not exhibit any visible cracks, which suggests that La-Fe-Si/resin composites have long-term cycle stability. In addition, Figure 6C compares the compressive stress-strain curves of the Resin3 composite before and after the thermal cycle test. It can be found that the compressive strength of the Resin3 composite after cycle stability test is 119.9 MPa, which is close to that of Resin3 composite before cycle stability test (116.6 MPa). Therefore, the mechanical properties of the composites do not show significant changes after the long-term cycle stability test.

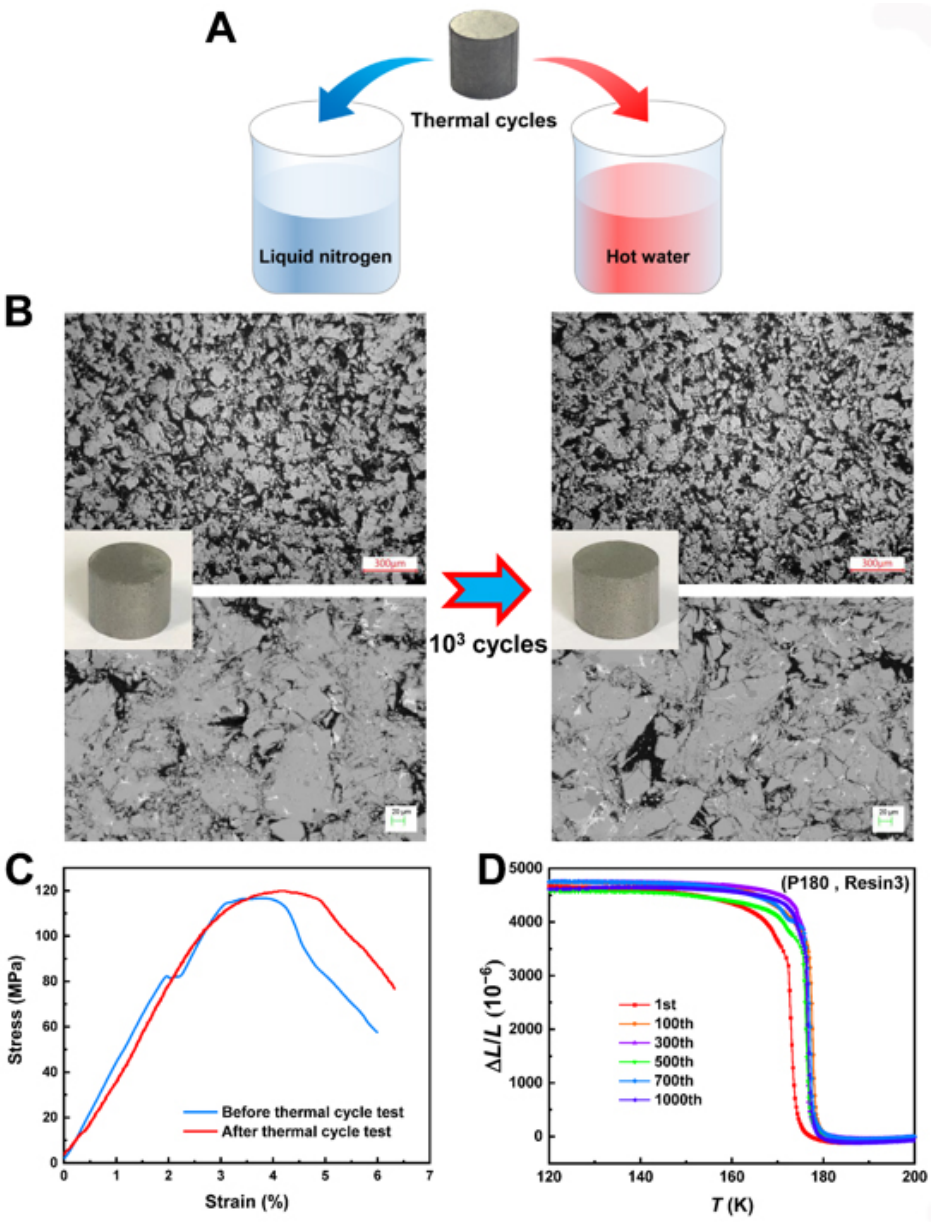

Figure 6. (A) Schematic illustration of thermal cycles; (B) surface morphology (upper) and SEM images (lower) of the Resin3 composite before and after 1000 thermal cycles; (C) compressive stress-strain curves of the Resin3 composite before and after cycle stability test; (D) temperature dependence of linear thermal expansion ($\Delta L/L$) for the Resin3 composite at the selected thermal cycles. SEM: Scanning electron microscopy.

Figure 6D shows the temperature dependence of the linear thermal expansion ($\Delta L/L$) for the Resin3 composite at some selected cycles. Note that the transition temperature increases after the first cycle. For La(Fe, Si)$_{13}$ compounds, the hydrostatic pressure can change the curve of the free energy $E(M, T)$ by the renormalization effect of spin fluctuations, thereby decreasing T_C[32]. Moreover, the internal constraints can also reduce the T_C[33]. Since La-Fe-Si/resin composites are prepared by compaction, the residual stress after the compaction and constraints from the surrounding epoxy resin will decrease the transition temperature of the $La_{0.7}Ce_{0.3}Fe_{11.51}Mn_{0.09}Si_{1.4}$ compound. During the thermal cycle, the cyclic MVE will drive $La_{0.7}Ce_{0.3}Fe_{11.51}Mn_{0.09}Si_{1.4}$ particles to shrink and expand repeatedly. This process will gradually release the residual stress

and surrounding constraints, increasing the transition temperature. After the 100th cycle, the release of residual stress and constraints is completed; thus, the transition temperature will no longer change. In addition, the NTE performance of the Resin3 composite undergoing different thermal cycles does not exhibit obvious variations, which proves its robust functional stability. These results strongly suggest that the fabricated La-Fe-Si/resin composites are highly suitable for practical applications as NTE materials.

CONCLUSIONS

In summary, epoxy resin-bonded La-Fe-Si/resin composites are fabricated, and their NTE is tuned by controlling the La-Fe-Si particle size and epoxy resin content. The reduction in particle size weakens the first-order magnetic transition of the $La_{0.7}Ce_{0.3}Fe_{11.51}Mn_{0.09}Si_{1.4}$ compound, which reduces NTE and the thermal/magnetic hysteresis. Meanwhile, the reduction in particle size first decreases porosity, which increases NTE until the average particle size of 180 μm. Then, the NTE decreases significantly with a further reduction in particle size caused by the weakening of the first-order magnetic transition and the increase in porosity. Furthermore, tailoring the epoxy resin content can tune the NTE of La-Fe-Si/resin composites more effectively. An increase in resin content also has two opposite effects on NTE. The La-Fe-Si/resin composite with 80 wt.% resin still exhibits significant NTE during the magnetic transition, which suggests that the $La_{0.7}Ce_{0.3}Fe_{11.51}Mn_{0.09}Si_{1.4}$ compound has strong NTE properties because of its magnetoelastic coupling effect. Moreover, the La-Fe-Si/resin composite with 20 wt.% resin exhibits ZTE behavior in a wide temperature range. Further microstructure analysis indicates that increasing the resin content can fill more pores, leading to a compact structure and enhancing the mechanical properties significantly. La-Fe-Si/resin composites can still maintain their mechanical integrity and excellent NTE properties after 1000 thermal cycles, which proves their excellent cycle stability. Consequently, with the excellent mechanical properties, durable cycle stability, and tunable NTE properties, the fabricated epoxy resin-bonded La-Fe-Si/resin composites could be an attractive candidate for NTE materials.

DECLARATIONS

Authors' contributions

Conceived the idea: Zhang H
Performed the experiments and data analysis: Zhou H, Liu Y, Xia M, Yu Z, Chen H, Qiao K, Cong J
Provided the technical support: Huang R, Chen B, Taskaev SV, Chu K
Wrote the manuscript: Zhou H, Zhang H

Availability of data and materials

Not applicable.

Financial support and sponsorship

This work was supported by the National Natural Science Foundation of China (Grant Nos.: 52171169, 52101210, 51971160, and 52142305); the National Key Research and Development Program of China (Grant No.: 2021YFB3501204); the Fundamental Research Funds for the Central Universities and the Youth Teacher International Exchange & Growth Program (Grant Nos.: FRF-GF-20-08B and QNXM20210014).

Conflicts of interest

All authors declared that there are no conflicts of interest.

Ethical approval and consent to participate

Not applicable.

Consent for publication

Not applicable.

REFERENCES

1. Evans JSO, Hu Z, Jorgensen JD, Argyriou DN, Short S, Sleight AW. Compressibility, phase transitions, and oxygen migration in zirconium tungstate, ZrW_2O_8. *Science* 1997;275:61-5. DOI PubMed
2. Mary TA, Evans JSO, Vogt T, Sleight AW. Negative thermal expansion from 0.3 to 1050 kelvin in ZrW_2O_8. *Science* 1996;272:90-2. DOI
3. Iikubo S, Kodama K, Takenaka K, Takagi H, Takigawa M, Shamoto S. Local lattice distortion in the giant negative thermal expansion material $Mn_3Cu_{1-x}Ge_xN$. *Phys Rev Lett* 2008;101:205901. DOI PubMed
4. Gao Q, Wang J, Sanson A, et al. Discovering large isotropic negative thermal expansion in framework compound $AgB(CN)_4$ via the concept of average atomic volume. *J Am Chem Soc* 2020;142:6935-9. DOI PubMed
5. Zhao YY, Hu FX, Bao LF, et al. Giant negative thermal expansion in bonded MnCoGe-based compounds with Ni_2In-type hexagonal structure. *J Am Chem Soc* 2015;137:1746-9. DOI PubMed
6. Katayama N, Otsuka K, Mitamura M, Yokoyama Y, Okamoto Y, Takenaka K. Microstructural effects on negative thermal expansion extending over a wide temperature range in β-$Cu_{1.8}Zn_{0.2}V_2O_7$. *Appl Phys Lett* 2018;113:181902. DOI
7. Song Y, Shi N, Deng S, Xing X, Chen J. Negative thermal expansion in magnetic materials. *Progr Mater Sci* 2021;121:100835. DOI
8. Li CW, Tang X, Muñoz JA, et al. Structural relationship between negative thermal expansion and quartic anharmonicity of cubic ScF_3. *Phys Rev Lett* 2011;107:195504. DOI PubMed
9. Chen J, Xing X, Sun C, et al. Zero thermal expansion in $PbTiO_3$-based perovskites. *J Am Chem Soc* 2008;130:1144-5. DOI PubMed
10. Shen BG, Sun JR, Hu FX, Zhang HW, Cheng ZH. Recent Progress in exploring magnetocaloric materials. *Adv Mater* 2009;21:4545-64. DOI
11. Liu Y, Fu X, Yu Q, Zhang M, Liu J. Significant reduction of phase-transition hysteresis for magnetocaloric $(La_{1-x}Ce_x)_2Fe_{11}Si_2H_y$ alloys by microstructural manipulation. *Acta Materialia* 2021;207:116687. DOI
12. Wang Y, Zhang H, Liu E, et al. Outstanding comprehensive performance of $La(Fe, Si)_{13}H_y$/In composite with durable service life for magnetic refrigeration. *Adv Electron Mater* 2018;4:1700636. DOI
13. Fujita A, Fujieda S, Hasegawa Y, Fukamichi K. Itinerant-electron metamagnetic transition and large magnetocaloric effects in $La(Fe_xSi_{1-x})_{13}$ compounds and their hydrides. *Phys Rev B* 2003;67:104416. DOI
14. Jia L, Sun JR, Zhang HW, Hu FX, Dong C, Shen BG. Magnetovolume effect in intermetallics $LaFe_{13-x}Six$. *J Phys Condens Matter* 2006;18:9999-10007. DOI
15. Huang R, Liu Y, Fan W, et al. Giant negative thermal expansion in $NaZn_{13}$-type $La(Fe, Si, Co)_{13}$ compounds. *J Am Chem Soc* 2013;135:11469-72. DOI PubMed
16. Li W, Huang R, Wang W, et al. Enhanced negative thermal expansion in $La_{(1-x)}Pr_xFe_{10.7}Co_{0.8}Si_{1.5}$ compounds by doping the magnetic rare-earth element praseodymium. *Inorg Chem* 2014;53:5869-73. DOI PubMed
17. Li S, Huang R, Zhao Y, Wang W, Han Y, Li L. Zero thermal expansion achieved by an electrolytic hydriding method in $La(Fe,Si)_{13}$ compounds. *Adv Funct Mater* 2017;27:1604195. DOI
18. Li S, Huang R, Zhao Y, Wang W, Li L. Cryogenic abnormal thermal expansion properties of carbon-doped $La(Fe,Si)_{13}$ compounds. *Phys Chem Chem Phys* 2015;17:30999-1003. DOI PubMed
19. Li S, Huang R, Zhao Y, et al. Broad negative thermal expansion operation-temperature window achieved by adjusting Fe-Fe magnetic exchange coupling in $La(Fe,Si)_{13}$ compounds. *Inorg Chem* 2015;54:7868-72. DOI PubMed
20. Wang J, Gong Y, Liu J, et al. Balancing negative and positive thermal expansion effect in dual-phase $La(Fe,Si)_{13}$/α-Fe in-situ composite with improved compressive strength. *J Alloys Compd* 2018;769:233-8. DOI
21. Zhang H, Sun Y, Niu E, Hu F, Sun J, Shen B. Enhanced mechanical properties and large magnetocaloric effects in bonded $La(Fe, Si)_{13}$ -based magnetic refrigeration materials. *Appl Phys Lett* 2014;104:062407. DOI
22. Toby BH. EXPGUI, a graphical user interface for GSAS. *J Appl Crystallogr* 2001;34:210-3. DOI
23. Bird M, Butler S, Hawkes C, Kotzer T. Numerical modeling of fluid and electrical currents through geometries based on synchrotron X-ray tomographic images of reservoir rocks using Avizo and COMSOL. *Comput Geosci* 2014;73:6-16. DOI
24. Sun XM, Cong DY, Ren Y, et al. Giant negative thermal expansion in Fe-Mn-Ga magnetic shape memory alloys. *Appl Phys Lett* 2018;113:041903. DOI
25. Li S, Huang R, Li W, Wang W, Zhao Y, Li L. Low-temperature negative thermal expansion behavior of LaFe11.2Al1.8-xSix compounds. *J Alloys Compd* 2015;646:119-23. DOI
26. Lin JC, Tong P, Tong W, et al. Tunable negative thermal expansion related with the gradual evolution of antiferromagnetic ordering in antiperovskite manganese nitrides $Ag_{1-x}NMn_{3+x}$ ($0 \leq x \leq 0.6$). *Appl Phys Lett* 2015;106:082405. DOI
27. Xia W, Huang J, Sun N, Lui C, Ou Z, Song L. Influence of powder bonding on mechanical properties and magnetocaloric effects of

$La_{0.9}Ce_{0.1}(Fe,Mn)_{11.7}Si_{1.3}H_{1.8}$. *J Alloys Compd* 2015;635:124-8. DOI

28. Shao Y, Liu J, Zhang M, et al. High-performance solid-state cooling materials: Balancing magnetocaloric and non-magnetic properties in dual phase La-Fe-Si. *Acta Materialia* 2017;125:506-12. DOI
29. Wang W, Huang R, Dai H, et al. Tunable near-zero thermal expansion in the C-doped La(Fe, $Si)_{13}$ compounds at cryogenic temperatures. *Mater Lett* 2019;237:26-8. DOI
30. Hu J, Lin K, Cao Y, et al. Adjustable magnetic phase transition inducing unusual zero thermal expansion in cubic RCO_2-based intermetallic compounds (R = rare earth). *Inorg Chem* 2019;58:5401-5. DOI PubMed
31. Song Y, Chen J, Liu X, et al. Zero Thermal expansion in magnetic and metallic $Tb(Co,Fe)_2$ intermetallic compounds. *J Am Chem Soc* 2018;140:602-5. DOI PubMed
32. Fujita A, Fukamichi K, Yamada M, Goto T. Influence of pressure on itinerant electron metamagnetic transition in $La(Fe_xSi_{1-x})_{13}$ compounds. *J Appl Phys* 2003;93:7263-5. DOI
33. Lyubina J, Schäfer R, Martin N, Schultz L, Gutfleisch O. Novel design of $La(Fe,Si)_{13}$ alloys towards high magnetic refrigeration performance. *Adv Mater* 2010;22:3735-9. DOI PubMed

Huang *et al. Microstructures* 2022;2:2022019
DOI: 10.20517/microstructures.2022.17

Microstructures

Research Article

Open Access

Check for updates

Effects of processing parameters on a β-solidifying TiAl alloy fabricated by laser-based additive manufacturing

Danni Huang[1,2], Yangping Dong[2], Hancong Chen[2], Yinghao Zhou[2], Ming-Xing Zhang[1], Ming Yan[2]

[1]School of Mechanical and Mining Engineering, The University of Queensland, Queensland 4072, Australia.
[2]Department of Materials Science and Engineering and Shenzhen Key Laboratory for Additive Manufacturing of High-Performance Materials, Southern University of Science and Technology, Shenzhen 518055, Guangdong, China.

Correspondence to: Prof. Ming-Xing Zhang, School of Mechanical and Mining Engineering, The University of Queensland, St. Lucia, Queensland 4072, Australia. E-mail: mingxing.zhang@uq.edu.au; Prof. Ming Yan, Department of Materials Science and Engineering and Shenzhen Key Laboratory for Additive Manufacturing of High-Performance Materials, Southern University of Science and Technology, 1088 Xueyuan Blvd, Nanshan, Shenzhen 518055, Guangdong, China. E-mail: yanm@sustech.edu.cn

How to cite this article: Huang D, Dong Y, Chen H, Zhou Y, Zhang MX, Yan M. Effects of processing parameters on a β-solidifying TiAl alloy fabricated by laser-based additive manufacturing. *Microstructures* 2022;2:2022019. https://dx.doi.org/10.20517/microstructures.2022.17

Received: 30 Jul 2022 **First Decision:** 31 Aug 2022 **Revised:** 13 Sep 2022 **Accepted:** 22 Sep 2022 **Published:** 28 Sep 2022

Academic Editor: Ting Zhu **Copy Editor:** Fangling Lan **Production Editor:** Fangling Lan

Abstract

β-solidifying TiAl alloys are considered as promising candidate materials for high-temperature structural applications. Laser-based additive manufacturing (LAM) enables the fabrication of components with geometrical complexity in near-net shape, leading to time and feedstock savings. In this study, a gas-atomized Ti-44Al-4Nb-1Mo-1Cr powder is used as a feedstock material for LAM. However, the LAM of TiAl alloys remains a challenge due to serious cracking during the printing process. To minimize the cracking, the optimization of the LAM processing parameters is essential. Hence, the effects of the LAM processing parameters on the cracking susceptibility and microstructure are studied here. Our experimental results show that the cracking susceptibility can be mitigated by increasing the laser power. Accordingly, the microstructure transforms from the dominating α_2 grains to a near-lamellar microstructure with an increment in laser power, leading to a reduction in microhardness, even though it is still higher than that of its as-cast counterparts. It is concluded that changes in the laser power can directly tailor the microstructure, phase composition and microhardness of LAM-fabricated TiAl alloys.

Keywords: β-solidifying TiAl alloy, laser-based additive manufacturing, phase, microstructural evolution, microhardness

INTRODUCTION

Intermetallic TiAl alloys are considered as excellent candidates for replacing Ni- and Ti-based alloys in aerospace applications due to their attractive properties, including low densities (3.8-4.2 g/cm^3), which are around half those of Ni-based alloys (8-9 g/cm^3)[1], high specific strength and creep resistance at elevated temperatures and better oxidation resistance than conventional Ti alloys, particularly at 600-800 °C[2,3]. After several years of fundamental research, novel β-solidifying TiAl alloys have been developed, which offer opportunities for weight reduction and an operating temperature of increase up to 850 °C[4,5]. These TiAl alloys are characterized by a high content of β-stabilizing elements, such as Nb and Mo, and composed of complex multi-phases[5], including the existence of a high volume fraction of β phase or its ordered counterparts, β_0[6].

In contrast to conventional TiAl alloys, which solidify via a peritectic solidification path (i.e., L → L + β → α→…), resulting in significant texture and segregation, β-solidifying TiAl alloys solidify via the β phase (i.e., L → L + β → β→…), showing an isotropic microstructure with modest segregation[7]. The principal constituents in β-solidifying TiAl alloys at room temperature are γ-TiAl (an ordered face-centered tetragonal $L1_0$ structure, P4/mmm, a = 0.3997 nm and c = 0.4062 nm), α_2-Ti_3Al (an ordered hexagonal $D0_{19}$ structure, $P6_3/mmc$, a = 0.5765 nm and c = 0.46833 nm) and β_0 (an ordered body-centered B2 structure, $Pm\bar{3}m$)[8]. However, due to the development of a long-range ordering of intermetallics, TiAl alloys exhibit intrinsic brittleness, meaning their development has been further impeded by a lack of design practice and processing difficulties[9]. A conventional casting process has been established for the mass production of TiAl components, but this is time-consuming, and its coarse as-cast microstructure is prone to causing microstructural inhomogeneity and poor room-temperature mechanical properties[10].

Additive manufacturing (AM) enables the fabrication of near-net-shape components with complex geometries at higher efficiency and lower costs, compared with conventional manufacturing technologies[11,12]. Thus, AM has significant potential for manufacturing TiAl alloys and is of technical and economic interest. So far, several works have demonstrated that electron beam melting (EBM) is capable of directly making TiAl near-net-shape parts[13-15]. However, significant Al loss and inhomogeneous microstructures were found in TiAl alloys produced from EBM[16,17], which are inevitably detrimental to the mechanical properties of the alloys. Compared to EBM, laser-based additive manufacturing (LAM) exhibits superior dimensional and surface finish qualities and lower machine costs due to the use of a finer laser beam and feedstock powder[18]. However, the major problem encountered during LAM is cracking[19]. In LAM, the high energy input and small heat-affected zone result in a high cooling rate (10^4-10^6 K/s) and the generation of high thermal stress[20], which brittle TiAl alloys cannot accommodate, leading to cracking and distortion. Due to the nature of the additive layers, the LAM process experiences a complex thermal history involving melting, subsequent solidification and numerous lower temperature reheating cycles, which lead to very specific microstructures[21]. Most published works have shown that the adjustment of processing parameters can alleviate the internal defects and tailor the microstructure[22,23], since the properties of TiAl alloys are strongly dependent on the microstructure[24-26].

To incorporate advanced manufacturing technology using novel materials, knowledge of processing-related properties is of great importance. Thus, in this study, the microstructural characterization of a β-solidifying TiAl alloy fabricated by LAM with different laser powers is presented. The influence of laser power on the

internal defects, microstructural features and microhardness are evaluated to better understand the effects of processing parameters on the LAM-based β-solidifying TiAl alloy.

EXPERIMENTAL PROCEDURE

The β-solidifying TiAl alloy with nominal composition Ti-44Al-4Nb-1Mo-1Cr (at.%) was used as the feedstock for LAM in the present study. The pre-alloyed spherical powder with particle sizes ranging from 47.8 to 130.0 μm was supplied by Xi'an Sailong Metal Materials Co., Ltd. The powder morphology is depicted in Figure 1A. Prior to printing, the powder was dried at 80 °C for 2 h under a vacuum to remove moisture.

An Optomec LENS 450 machine was used to print the TiAl alloy samples on Ti-6Al-4V substrates. The laser power was altered while other parameters were kept constant, as listed in Table 1. Basically, the LENS 450 machine uses a 1064 nm wavelength Nd:YAG laser, a four-nozzle coaxial powder feeder, a controlled environment chamber and a motion control system. During the printing process, a high-powered laser beam is focused onto the substrate while the alloy powders are injected into the substrate from the powder delivery nozzles[27]. Upon interaction with the energy source, the powder was melted almost instantly, creating melt pools and then solidifying rapidly as the energy source moved away[11]. Successive layers are sequentially deposited to build the designed geometry. The printing process was conducted in an Ar-purged processing chamber where an oxygen content of less than 10 ppm was maintained to avoid oxidation. The cubic parts (10 mm × 10 mm × 10 mm) were built for further metallographic characterization. The printing scheme used in this study was a bi-directional scan in the X-Y plane without rotation between the layers.

The as-printed samples were sectioned along the longitudinal planes, which were parallel to the building direction, followed by mechanically grinding and polishing and chemically etching with Keller's reagent (4 vol.% HNO_3, 2 vol.% HF and 94 vol.% H_2O) to reveal the general structure[28]. An optical microscope (Zeiss Axio Observer 3) was used to investigate the defects. The microstructures of the pre-alloyed powder and as-printed samples were characterized by a Zeiss Merlin field-emission scanning electron microscope (SEM). The grain morphologies of the as-printed samples were observed using electron backscattered diffraction (EBSD, Zeiss Merlin, operated at 20 kV and 5 nA). The phase identification of the as-printed samples was performed with X-ray diffraction (XRD, Bruker D8) using Cu Kα radiation. The diffraction angle ranged from 20° to 100° with a step size of 0.01°. XRD analysis was carried out on the longitudinal planes of the alloys produced from LAM. The binary phase diagram of the Ti-Al system provides effective guidance for studying the phase transformation process. The binary Ti-Al phase diagram was calculated with the aid of Thermo-Calc software on the basis of a commercially available thermodynamic database.

The Vickers microhardness was measured on a microhardness tester (HXD-1000TMC, Shanghai Taiming Optical Instrument Corporation, China) with a 300 g load held for 15 s. At least ten measurements were taken for each sample.

RESULTS AND DISCUSSION

LAM-based β-solidifying TiAl alloy

The scanning electron microscope-energy dispersive X-ray spectroscopy (SEM-EDS) measured elemental concentrations of the pre-alloyed powder and the as-printed samples fabricated with different laser power inputs are listed in Table 2. Negligible changes in the chemical composition of the as-printed alloys after LAM were detected in comparison to the original pre-alloyed powder. Hence, the chemical composition of the as-printed samples was not affected by the LAM process in this study.

Table 1. Design of LAM processing parameters for β-solidifying TiAl alloy

Parameters	Value
Laser power (W)	230, 260, 290, 320, 350 and 380
Laser scan speed (mm/min)	650
Powder feeder rate (rpm)	4
Layer thickness (inches)	0.01
Hatching spacing (inches)	0.015
Argon	99.999% purity

LAM: Laser-based additive manufacturing.

Table 2. EDS analysis results showing elemental concentrations for pre-alloyed powder used and as-printed samples

Sample	Ti (wt.%)	Al (wt.%)	Nb (wt.%)	Mo (wt.%)	Cr (wt.%)
Powder	58.18	29.93	8.23	2.33	1.35
230 W	59.23	30.11	7.69	1.61	1.37
260 W	57.32	31.79	7.91	1.67	1.32
290 W	58.21	30.96	7.77	1.79	1.29
320 W	58.15	30.90	7.89	1.73	1.34
350 W	57.94	31.02	8.02	1.71	1.31
380 W	58.09	31.21	7.65	1.61	1.34

EDA: Energy dispersive X-ray spectroscopy.

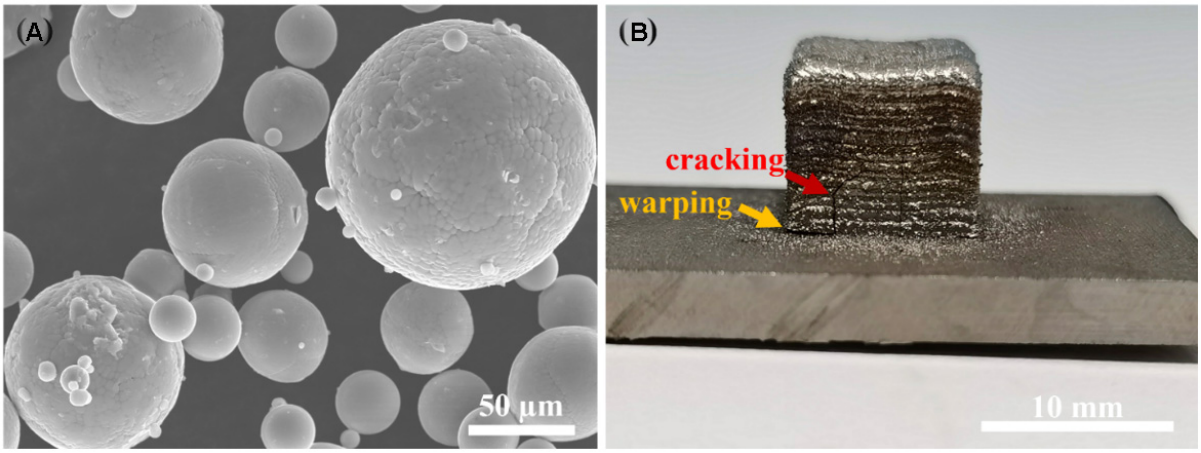

Figure 1. (A) Pre-alloyed Ti-44Al-4Nb-1Mo-1Cr powder morphology. (B) Representative image showing macrographs of as-printed specimens built with a laser power of 320 W.

The typical appearance of the LAM-fabricated β-solidifying TiAl samples with dimensions of 10 mm × 10 mm × 10 mm is shown in Figure 1B. The surface of the as-printed sample is metallic and shiny, which implies that oxidation is negligible during the printing processing. However, visual observation of as-printed sample shows that the samples contain obvious surface defects, cracks and warping. Those are common defects encountered in additive manufacturing. During the printing process, the material experiences a large thermal gradient, leading to residual thermal stresses. The brittle TiAl alloy is unable to tolerate such high stresses, resulting in cracking and warping. Moreover, warping usually starts from the corner. With each newly deposited layer, the residual stresses accumulate, finally resulting in the part peeling away from the substrate[29]. The separation of the printed sample from the substrate is emphasized

by the orange arrow in Figure 1B. The most critical issue is the occurrence of cracking associated with the LAM of the TiAl alloy, which usually originates from the edge of the sample and at the interface between the sample and substrate. This observation agrees with previous studies of the LAM of TiAl alloys[19,30].

The relationship between cracking susceptibility and laser power was further investigated. All as-printed samples produced with different laser powers contain cracks, as indicated by the red arrows in Figure 2. At a very low laser power of 230 W, the long and deep cracks originated from the edge of the sample and propagated along the building direction of the as-printed sample, as shown in Figure 2A. However, increasing the laser from 230 to 380 W led to alleviation of the cracking in the as-printed samples, as shown in Figure 2B-F. Only short cracks were observed as the laser increased to 380 W [Figure 2F]. The cracking in LAM is ascribed to the generation of thermal stress, which is caused by a large thermal gradient during laser heating. The extent of cracking is expected to be severe because brittle TiAl alloys cannot accommodate such high stress through deformation. The energy density input is defined as the energy per unit area, which is calculated by[30]:

$$E = \frac{P}{\upsilon D} \tag{1}$$

where P is the laser power, υ is the scanning speed and D is the laser beam diameter. The cooling rate during the printing process is dependent on the energy input based on Rosenthal's three-dimensional solution[31], which can be expressed as follows:

$$\frac{\partial T}{\partial t} \propto \frac{k\,(T-T_0)^2}{P/v} \tag{2}$$

where k is the thermal conductivity of the material and T_0 is the substrate temperature. The cooling rate is inversely proportional to the energy density. A higher energy density can increase the width of the melt pool's contact with the substrate, thereby producing a larger melt pool that can maintain fluidity for a long period and prevent a high cooling rate[25]. Therefore, the mitigation of the cracking is attributed to the lower cooling rate resulting from the higher energy input.

Microstructure and phase analysis

XRD was used to determine the phase constituents of the LAM-based samples fabricated with different laser powers. To better understand the phase transformation during the solidification process, a calculated Ti-Al phase diagram is provided in Figure 3B. The XRD patterns obtained across the building direction confirm the existence of three phases. The results, as presented in Figure 3A, reveal that the diffraction peaks belong to the α_2, γ and β_0 phases in the as-printed samples. There is a slight deviation at a few peaks, which is ascribed to the change in the size of the tested specimens and the lattice imperfection caused by the high cooling rate and complex thermal history during the LAM process. It is noteworthy that more diffraction peaks of the γ phase could be detected with increasing laser power. This result illustrates that the content of the γ phase gradually increases with enhanced laser power.

The general microstructure appears to be refined in comparison to the conventionally processed TiAl alloys[4] due to the higher cooling rate. Different microstructures could be observed for the as-printed alloys depending on the laser power. The microstructures of the as-printed TiAl alloys manufactured with low laser power consist of mostly α_2 phases [Figure 4A and B], which are not typical for TiAl alloys. These are related to the high cooling rates, which suppress the formation of lamellar, because the diffusion-controlled

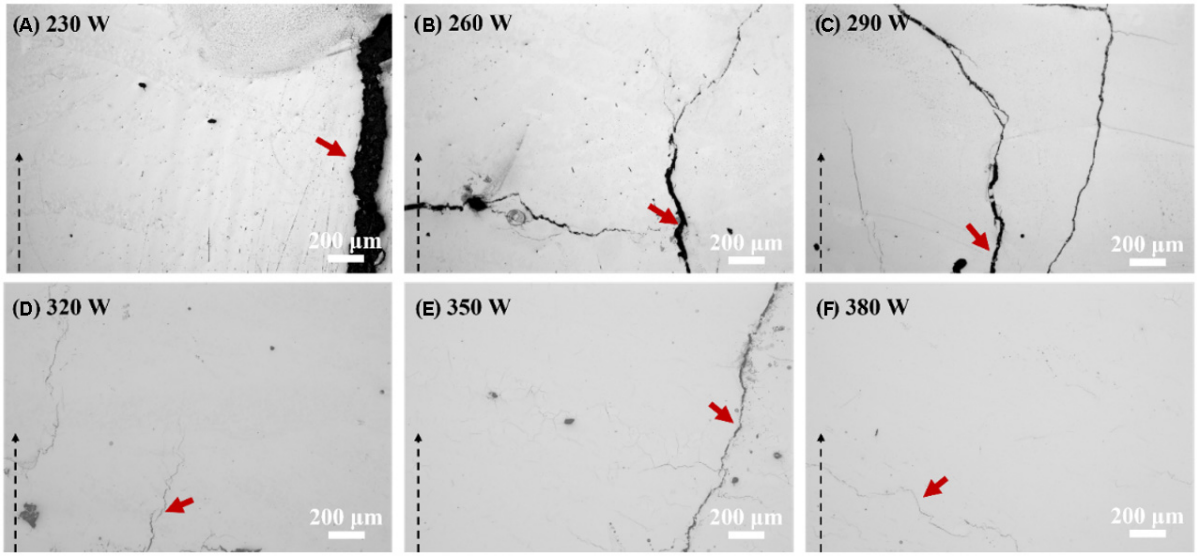

Figure 2. Cross-section views of as-printed samples with different laser powers: (A) 230; (B) 260; (C) 290; (D) 320; (E) 350; (F) 380 W. Internal defects are observed on the ground and polished samples. Dashed arrows indicate the build direction.

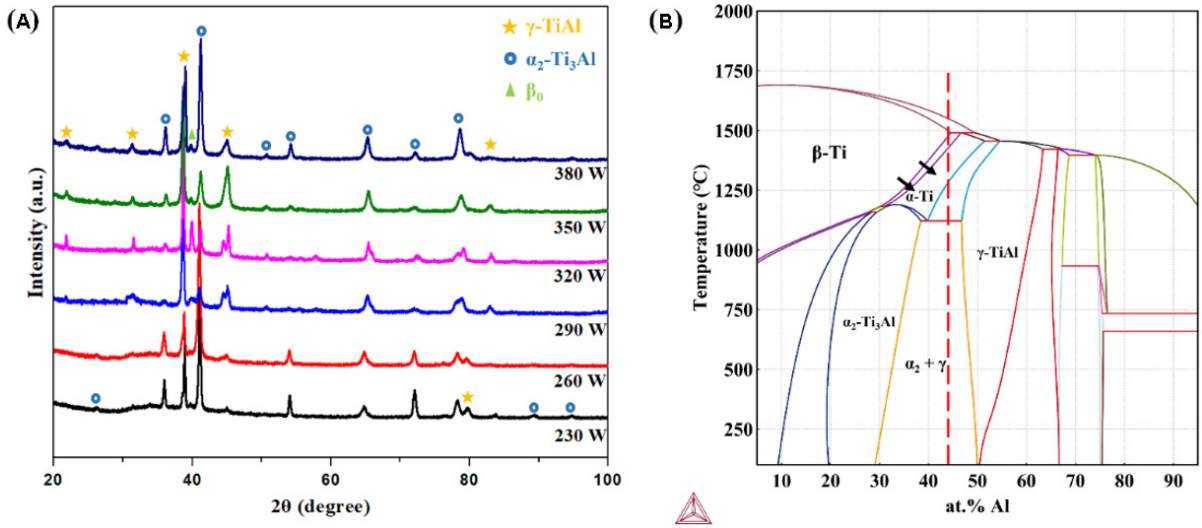

Figure 3. (A) XRD patterns of as-printed samples fabricated by different laser powers of 230, 260, 290, 320, 350 and 380 W. (B) Phase diagram for Ti-Al alloy (at.%). The arrows indicate the movement of the phase boundaries for β-stabilizing element additions. XRD: X-ray diffraction.

phase transformation of $\alpha \rightarrow \alpha_2 + \gamma$ is sensitive to the cooling rate[32]. For the as-printed specimens fabricated using laser powers of 230 and 260 W, the cooling rate is high enough that the $\alpha \rightarrow \alpha_2$ transformation took place. The lamellar colonies could be recognized in some regions with the intermediate laser power of 290 W [Figure 4C]. A very fine irregular near-lamellar structure formed as the laser power increased to 320 W.

The equiaxed γ (dark) grains and β_0 (bright) phase decorate the α_2/γ colony boundaries, as indicated by the green and blue arrows, respectively, in Figure 4D. Since the strong β-stabilizing elements of Nb and Mo concentrated in the primary β phase at high temperature and were hard to diffuse during a shorter time, the

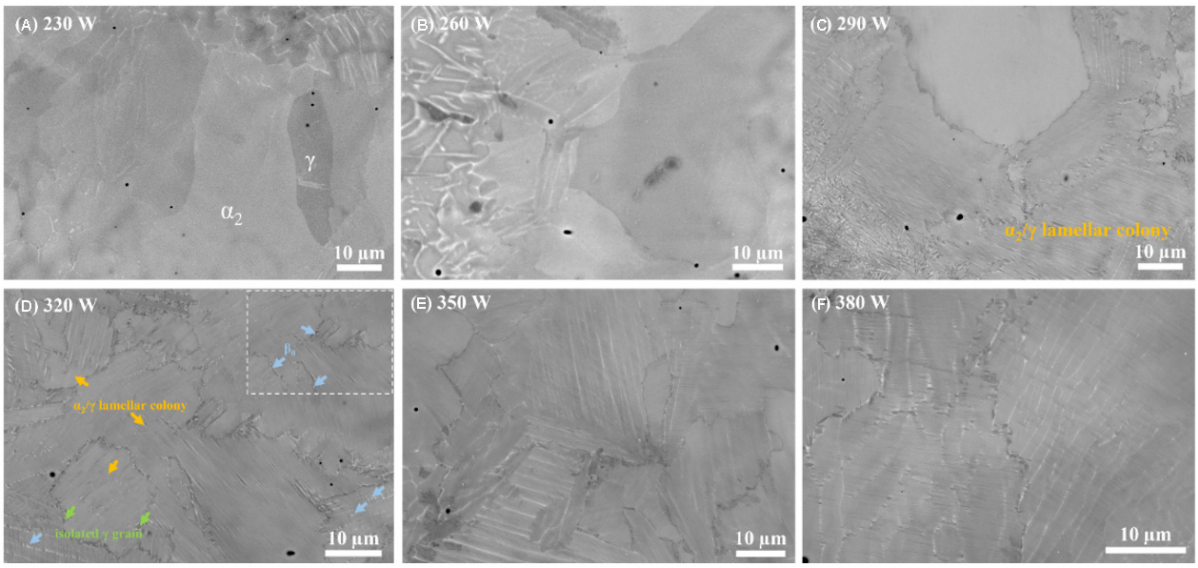

Figure 4. SEM-BSE images showing the effect of laser power on microstructures of LAM-based TiAl alloys: (A) 230; (B) 260; (C) 290; (D) 320; (E) 350; (F) 380 W. The insert shows the details at higher magnification. SEM: Scanning electron microscope.

primary β phase could not completely decompose into the α phase. Part of the primary β phase would be retained and directly ordered to the β_0 phase upon the further cooling process, which was distributed along the grain boundary, as indicated in Figure 4D. Moreover, it can be found that the β_0 phase can be identified within the lamellar colonies, which is consistent with the previous works of Xu *et al.*[33] and Schwaighofer *et al.*[34]. They demonstrated that the β_0 phase formed from the reaction $\alpha \rightarrow \beta + \gamma$, which also confirmed the existence of the $(\beta + \alpha + \gamma)$ phase field and no single α phase region was observed in the currently studied alloy. When further increasing the laser power, no obvious morphology change was observed, as depicted in Figure 4E and F.

To understand the formation of the microstructure, the Ti-Al binary phase diagram is provided, as shown in Figure 3B, which is calculated by the Thermo-Calc analysis. However, in the case of the β-solidifying TiAl alloy, due to the existence of β-stabilizing elements, Nb, Mo and Cr in this study shift the single β-Ti phase boundaries to a higher Al content regime, thus expanding the β-Ti phase field, as indicated by the black arrow in Figure 3B. Since the β-solidifying TiAl alloy contains sufficient β-stabilizing elements, the solidification pathway would be more complicated than the conventional casting of the TiAl alloy[33]. Therefore, the solidification pathway in our study takes place completely via the β phase following the sequence: $L \rightarrow L + \beta \rightarrow \beta \rightarrow \beta + \alpha \rightarrow \beta + \alpha + \gamma \rightarrow \beta + \alpha_2 + \gamma \rightarrow \beta_0 + \alpha_2/\gamma + \gamma$. The α_2 and β_0 phases are ordered α and β phases, respectively, at low temperatures[35]. After solidification and upon further cooling, the disordered hexagonal α nucleates following the Burgers orientation relationship as $(0001)_\alpha||\{110\}_\beta$ and $<11\bar{2}0>_\alpha||<1\bar{1}1>_\beta$[36]. Upon continuous cooling, the α phases transform to either α_2, γ or a mixture of both, depending on the cooling rate[37]. The $\alpha \rightarrow \alpha_2 + \gamma$ solid-state transformation is sensitive to the cooling rate[38]. The formation of γ lath in the α phase is controlled by the long-range diffusion process[39]. At a lower cooling rate, the γ/α_2 lamellar structure could be observed in some regions, which resulted from precipitation of γ lamellae in the α matrix, obeying the Blackburn orientation relationship. At the higher cooling rate, the high-temperature α phase is only ordered into α_2 instead of decomposing to the γ phase[24,40]. The brittle α_2 phases, which are unable to withstand the deformation, are supposed to be responsible for the cracking.

The lamellar colony consists of α_2-Ti_3Al and γ-TiAl, which stems from the solid-state phase transformation. The ultrafine and closely packed lamellae, which are alternating α_2-Ti_3Al and γ-TiAl, are further characterized by TEM in detail, as shown in Figure 5. According to the TEM bright-field images in Figure 5A, fine lamellar with an average lamellar spacing on a nanoscale (44 nm) is presented, while the lamellar spacing is 1-2 μm in the case of conventionally processed TiAl alloys[41]. The insert selected area electron diffraction proved the Blackburn orientation relationship between the α_2/γ lamellae, which is $(111)_\gamma \,||(0001)_{\alpha 2}$ and $<110>_\gamma \,||<11\bar{2}0>_{\alpha 2}$[42]. Several studies found that fined-grained lamellar colonies with few soft γ grains at the colony boundaries performed good creep strength, high fracture toughness and adequate ductility for as-cast TiAl alloys[43,44].

Grain features

EBSD was introduced and conducted on the representative LAM-based TiAl alloy samples fabricated by different laser powers of 230, 290 and 350 W to characterize the influence of laser power on grain features, which are relevant to the energy density inputs[24,45]. The EBSD phase map of the as-printed TiAl alloy fabricated at 230 W, as shown in Figure 6A, demonstrates that the microstructure is dominated by the α_2 phase (green) and a small amount of γ (red) and β_0 (yellow). The content of the γ phase increases with the reduction of the α_2 phase with increasing laser power. This phenomenon is ascribed to the competition between $\alpha \rightarrow \alpha + \gamma \rightarrow \alpha_2 + \gamma$ transformation and the direct-ordering $\alpha \rightarrow \alpha_2$ reaction[46]. According to Equation (2), a lower laser power resulted in a higher cooling rate, in which case the growth of γ lamellae was suppressed because of a shorter time for passing through the $(\alpha + \gamma)$ phase region. The direct-ordering $\alpha \rightarrow \alpha_2$ reaction was more favored under faster cooling conditions. Therefore, the microstructure built with a lower laser power was dominated by the α_2 phase. The microstructure was then dominated by the γ phase as the laser power increased to 290 W [Figure 6B]. The EBSD results are in good agreement with the XRD patterns. The detected β_0 phase is mainly distributed along the grain boundary. It should be noted that the β_0 phase located within lamellar colonies is on the nanoscale and the α_2 lamellae are extremely thin (~10 nm). Thus, some α_2 and β_0 phases in Figure 6C are underdetected due to the resolution limit of EBSD.

EBSD inverse pole figure maps are presented for each specimen in Figure 7A-C. The different colors correspond to different orientations in grains with respect to the crystal lattice. A multi-orientation of grains is distributed along the building direction. To measure the grain size, the representative band contrast maps, which provide higher contrast for counting, are shown in Figure 7D-F. Moreover, the average grain sizes of the as-presented samples were calculated to be 10.68, 14.50 and 25.77 μm, respectively. The grain size increases with increasing laser power. Figure 8 presents the grain misorientation angle map. The grain boundaries were categorized as low-angle grain boundaries (< 15°, LAGBs) and high-angle grain boundaries (> 15°, HAGBs). Obviously, the as-printed alloys are dominated by HAGBs with percentages of 92.12%, 97.68% and 98.54%, respectively. HAGBs are generally caused by dynamic recrystallization[4]. Because LAM is a layer-wise addition process, this process involves several reheating cycles due to successive laser track and laser deposition. The previously solidified layers would be inevitably reheated when making a new layer. This phenomenon is similar to the annealing heat treatment in which recrystallization would take place[47]. Furthermore, the content of HAGBs is observed to increase with increasing laser power. An increase in laser power will result in a lower solidification rate and provide a longer time for remelting and recrystallization. Therefore, the grain features could be tailored by varying the applied laser power.

Microhardness

To investigate the role of the processing parameters in determining the mechanical properties, microhardness measurements were conducted on the LAM-based TiAl alloys fabricated with different laser powers. The results are presented in Figure 9. The microhardness of the samples varies in the range of 475.1 to 534.8 HV, much higher than the corresponding as-cast counterparts reported in the literature, which are

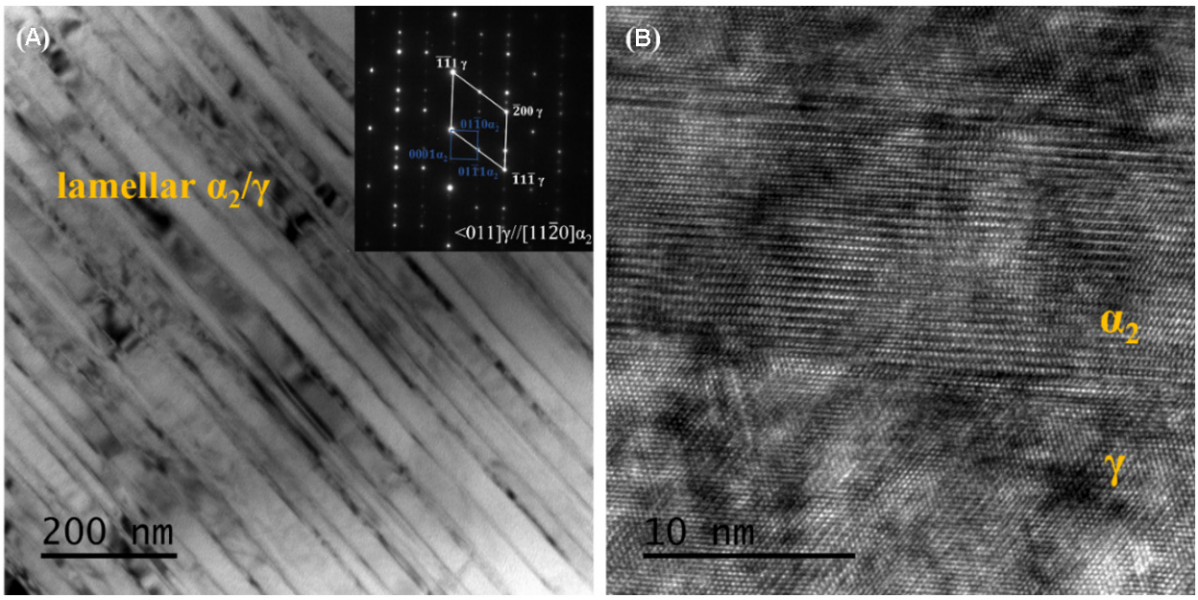

Figure 5. Structural details of lamellar colony characterized via TEM, showing an ultrafine lamellar structure. (A) TEM bright-field image showing the lamellae. The insert SADP showing the Blackburn orientation relationship followed by α_2/γ lamellae. (B) HRTEM image presenting α_2 and γ plates.

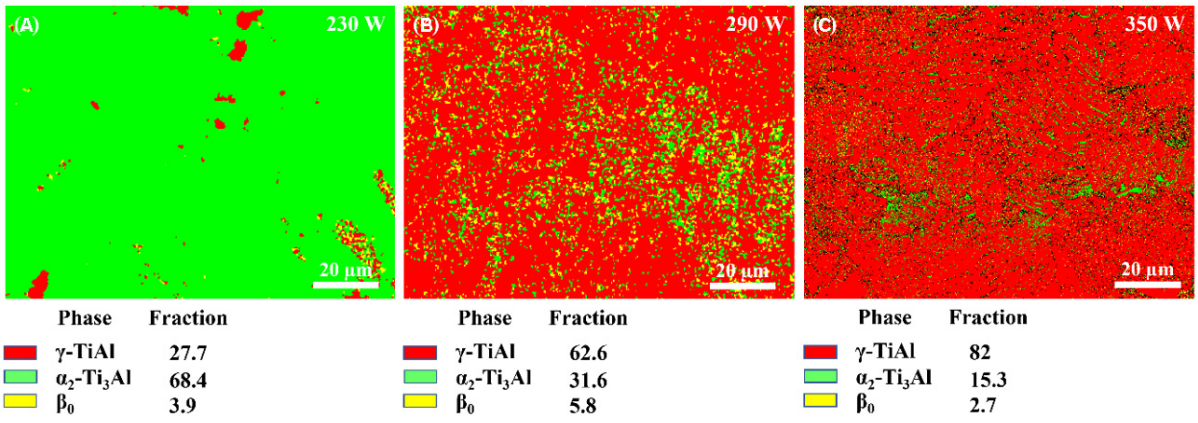

Figure 6. Phase maps from EBSD analysis showing the phase distribution and phase fraction of typical as-printed TiAl alloys fabricated by different laser powers: (A) 230; (B) 290; (C) 350 W. Red, green and yellow represent the γ, α_2 and β_0 phases, respectively. EBSD: Electron backscattered diffraction.

generally less than 351 HV[34]. In addition, it is evident that the microhardness is reduced with increasing laser power from 230 to 380 W. The reduction of the microhardness is mainly attributed to the following two reasons. At lower laser power, the phase composition is dominated by the α_2 phase. The α_2 phase was found to be harder than the γ phase and lamellar colony[4]. Therefore, the reduction in the α_2 phase decreases the microhardness. Furthermore, according to the Hall-Petch relation equation, the hardness of a material is dependent on its grain size. Thus, the hardness-grain size relation is described as[48]:

$$H = H_0 + K_H d^{-1/2} \quad (3)$$

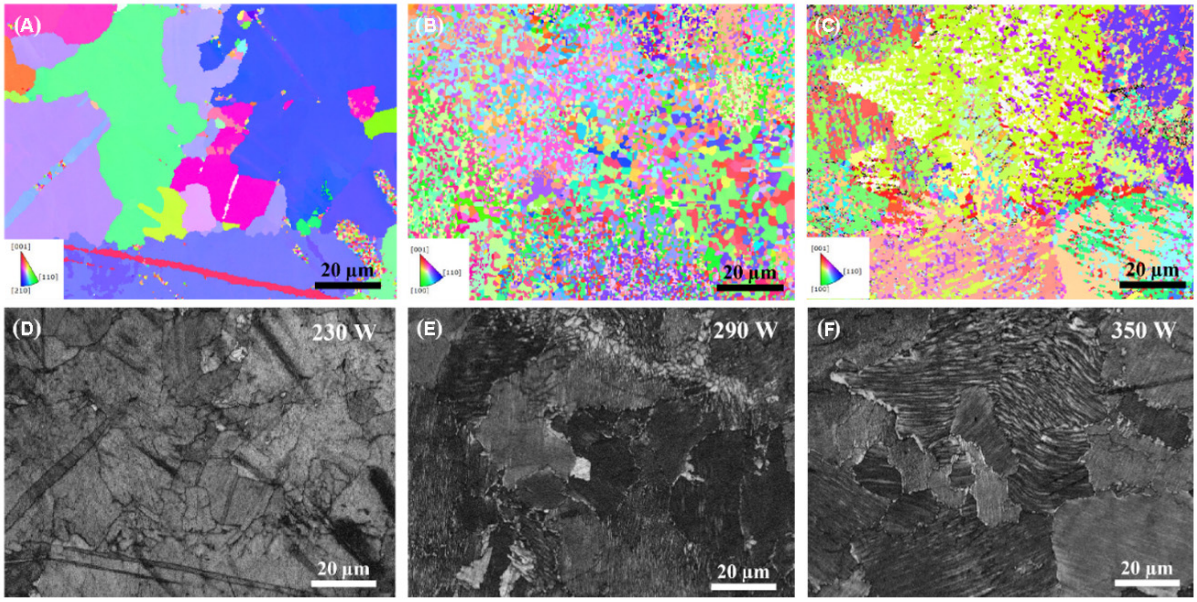

Figure 7. EBSD inverse pole figure maps and image quality maps showing grain orientation and distribution of as-printed TiAl alloys fabricated by different laser powers of (A) and (D) 230, (B) and (E) 290 and (C) and (F) 350 W. EBSD: Electron backscattered diffraction.

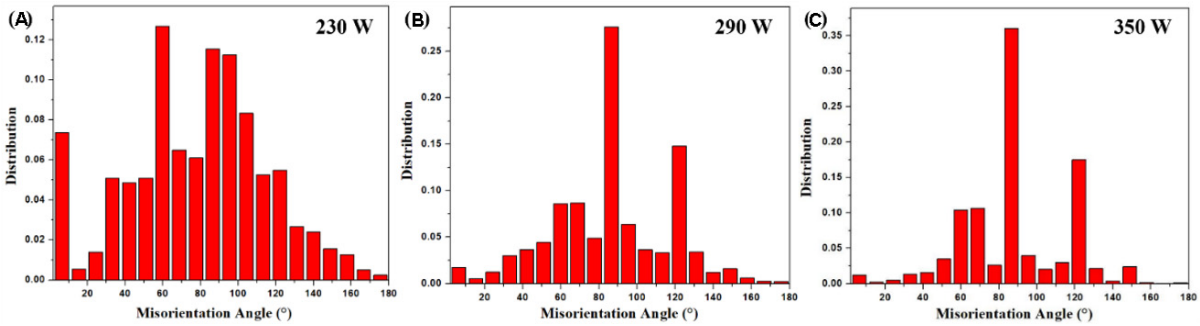

Figure 8. Grain orientation maps of as-printed TiAl samples fabricated by different laser powers of (A) 230, (B) 290 and (C) 350 W.

where H_0 and K_H are constants. As discussed above, the grain size generally increases with increasing laser power, thus leading to the reduction in microhardness. In addition, due to the rapid cooling rate during the printing process, the LAM-based specimens exhibited refined grain size than the casting counterparts, contributing to the increase of microhardness in the as-printed state.

CONCLUSION

In this study, a β-solidifying TiAl alloy, Ti-44Al-4Nb-1Mo-1Cr, was fabricated by LAM with different laser powers. Due to the complex thermal history during the LAM process, the as-printed intermetallic TiAl alloy samples showed susceptibility to cracking. Our work proved that the cracking problem could be mitigated by increasing the incident laser power to control the cooling rate. Nevertheless, the optimized process parameters could not suppress it totally. Therefore, future work is necessary to explore effective methods to achieve crack-free specimens. Several methods are worthy of investigation. For example, the optimized processing parameters combined with an external heating source can slow down the cooling rate and prevent cracking, or incorporation with hot isostatic pressing is possible to heal short cracks. Moreover, in

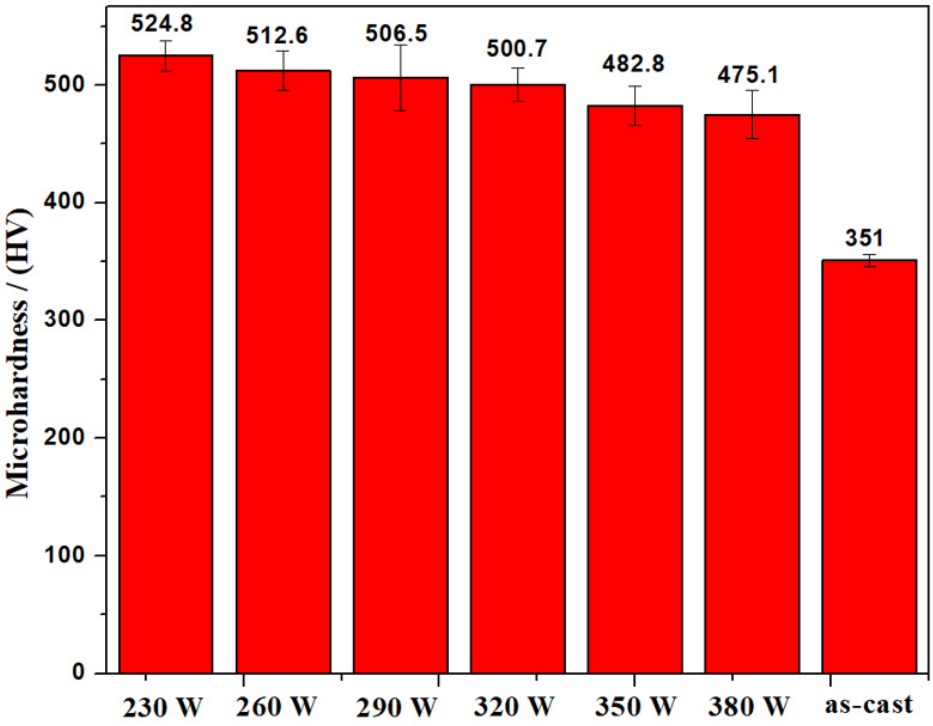

Figure 9. Microhardness of as-printed samples fabricated by different laser powers in comparison with the as-cast counterparts.

the present study, the operation parameter (laser power) has a significant effect on the microstructural evolution of the as-printed samples. The microstructure is dominated by brittle α_2 phase with lower laser power, while the microstructure exhibits a near-lamellar structure with an ultrafine lamellar spacing as the laser power increases to 380 W. The as-printed specimens all exhibited higher microhardness compared with that fabricated by casting.

DECLARATIONS

Acknowledgments

The authors would like to acknowledge the technical assistance of SUSTech Core Research Facilities.

Authors' contributions

Contributed to conception and design of the study, data collection and analysis, manuscript drafting: Huang D
Contributed to the material characterization: Dong Y
Helped with material preparation: Chen H
Contributed to mechanism explanation: Zhou Y
Supervised the overall project: Zhang MX
Supervised the overall project: Yan M

Availability of data and materials

Not applicable.

Financial support and sponsorship

This study is supported by Research and Development Program Project in Key Areas of Guangdong Province (Grants No. 2019B090907001 and 2019B010943001), Natural Science Foundation of Guangdong

Province (2020A1515011373), the Central Guidance on Local: Construction of regional innovation system - Cross Regional R & D cooperation projects (20221ZDH04054) and ARC DP program (DP210103162).

Conflicts of interest

All authors declared that there are no conflicts of interest.

Ethical approval and consent to participate

Not applicable.

Consent for publication

Not applicable.

Copyright

REFERENCES

1. Perrut M, Caron P, Thomas M, Couret A. High temperature materials for aerospace applications: Ni-based superalloys and γ-TiAl alloys. *Comptes Rendus Physique* 2018;19:657-71. DOI
2. Dimiduk DM. Gamma titanium aluminide alloys-an assessment within the competition of aerospace structural materials. *Mater Sci Eng* 1999;263:281-8. DOI
3. Wu X. Review of alloy and process development of TiAl alloys. *Intermetallics* 2006;14:1114-22. DOI
4. Niu HZ, Chen YY, Xiao SL, Xu LJ. Microstructure evolution and mechanical properties of a novel beta γ-TiAl alloy. *Intermetallics* 2012;31:225-31. DOI
5. Clemens H, Mayer S. Design, processing, microstructure, properties, and applications of advanced intermetallic TiAl alloys. *Adv Eng Mater* 2013;15:191-215. DOI
6. Kartavykh A, Asnis E, Piskun N, Statkevich I, Gorshenkov M, Korotitskiy A. A promising microstructure/deformability adjustment of β-stabilized γ-TiAl intermetallics. *Mater Lett* 2016;162:180-4. DOI
7. Clemens H, Wallgram W, Kremmer S, Güther V, Otto A, Bartels A. Design of novel β-solidifying TiAl alloys with adjustable β/B2-phase fraction and excellent hot-workability. *Adv Eng Mater* 2008;10:707-13. DOI
8. Mayer S, Erdely P, Fischer FD, et al. Intermetallic β-solidifying γ-TiAl based alloys - from fundamental research to application: intermetallic β-solidifying γ-TiAl based alloys. *Adv Eng Mater* 2017;19:1600735. DOI
9. Kothari K, Radhakrishnan R, Wereley NM. Advances in gamma titanium aluminides and their manufacturing techniques. *Prog Aerosp Sci* 2012;55:1-16. DOI
10. Thomas M, Raviart JL, Popoff F. Cast and PM processing development in gamma aluminides. *Intermetallics* 2005;13:944-51. DOI
11. Sahasrabudhe H, Bose S, Bandyopadhyay A. Laser-based additive manufacturing processes. *Adva Laser Mater Proc* 2018:507-39. DOI
12. Li S, Li J, Jiang Z, et al. Controlling the columnar-to-equiaxed transition during directed energy deposition of inconel 625. *Addit Manufact* 2022;57:102958. DOI
13. Narayana P, Li C, Kim S, et al. High strength and ductility of electron beam melted β stabilized γ-TiAl alloy at 800 °C. *Mater Sci Eng* 2019;756:41-5. DOI
14. Wartbichler R, Clemens H, Mayer S. Electron beam melting of a β-solidifying intermetallic titanium aluminide alloy. *Adv Eng Mater* 2019;21:1900800. DOI
15. Baudana G, Biamino S, Klöden B, et al. Electron beam melting of Ti-48Al-2Nb-0.7Cr-0.3Si: feasibility investigation. *Intermetallics* 2016;73:43-9. DOI
16. Lin B, Chen W, Yang Y, Wu F, Li Z. Anisotropy of microstructure and tensile properties of Ti-48Al-2Cr-2Nb fabricated by electron beam melting. *J Alloys Compd* 2020;830:154684. DOI
17. Schwerdtfeger J, Körner C. Selective electron beam melting of Ti-48Al-2Nb-2Cr: microstructure and aluminium loss. *Intermetallics* 2014;49:29-35. DOI
18. Bhavar PKV, Patil V, Khot S, Gujar K, Singh R. A review on powder bed fusion technology of metal additive manufacturing, In 4th international conference and exhibition on additive manufacturing technologies-AM-2014, 1-2 Septeber 2014, Banglore, India. DOI
19. Sharman A, Hughes J, Ridgway K. Characterisation of titanium aluminide components manufactured by laser metal deposition. *Intermetallics* 2018;93:89-92. DOI
20. Yan Z, Liu W, Tang Z, et al. Review on thermal analysis in laser-based additive manufacturing. *Opt Laser Technol* 2018;106:427-41. DOI
21. Zheng B, Zhou Y, Smugeresky J, Schoenung J, Lavernia E. Thermal behavior and microstructural evolution during laser deposition

with laser-engineered net shaping: part I. numerical calculations. *Metall Mat Trans A* 2008;39:2228-36. DOI

22. Srivastava D, Chang ITH, Loretto MH. The effect of process parameters and heat treatment on the microstructure of direct laser fabricated TiAl alloy samples. *Intermetallics* 2001;9:1003-13. DOI
23. Balla VK, Das M, Mohammad A, Al-ahmari AM. Additive manufacturing of γ-TiAl: processing, microstructure, and properties: additive manufacturing of γ-TiAl: processing. *Adv Eng Mater* 2016;18:1208-15. DOI
24. Li W, Liu J, Zhou Y, et al. Effect of laser scanning speed on a Ti-45Al-2Cr-5Nb alloy processed by selective laser melting: microstructure, phase and mechanical properties. *J Alloys Compd* 2016;688:626-36. DOI
25. Löber L, Schimansky FP, Kühn U, Pyczak F, Eckert J. Selective laser melting of a beta-solidifying TNM-B1 titanium aluminide alloy. *J Mater Proc Technol* 2014;214:1852-60. DOI
26. Biamino S, Penna A, Ackelid U, et al. Electron beam melting of Ti-48Al-2Cr-2Nb alloy: microstructure and mechanical properties investigation. *Intermetallics* 2011;19:776-81. DOI
27. Huang SH, Liu P, Mokasdar A, Hou L. Additive manufacturing and its societal impact: a literature review. *Int J Adv Manuf Technol* 2013;67:1191-203. DOI
28. Zhou Y, Li W, Wang D, et al. Selective laser melting enabled additive manufacturing of Ti-22Al-25Nb intermetallic: excellent combination of strength and ductility, and unique microstructural features associated. *Acta Mater* 2019;173:117-29. DOI
29. Brion DA, Shen M, Pattinson SW. Automated recognition and correction of warp deformation in extrusion additive manufacturing. *Addit Manuf* 2022;56:102838. DOI
30. Abdulrahman KO, Akinlabi ET, Mahamood RM. Characteristics of laser metal deposited titanium aluminide. *Mater Res Express* 2019;6:046504. DOI
31. Liu W, Dupont JN. Fabrication of carbide-particle-reinforced titanium aluminide-matrix composites by laser-engineered net shaping. *Metall Mater Trans A* 2004;35:1133-40. DOI
32. Li W, Liu J, Wen S, Wei Q, Yan C, Shi Y. Crystal orientation, crystallographic texture and phase evolution in the Ti-45Al-2Cr-5Nb alloy processed by selective laser melting. *Maters Charact* 2016;113:125-33. DOI
33. Xu H, Li X, Xing W, Shu L, Ma Y, Liu K. Solidification pathway and phase transformation behavior in a beta-solidified gamma-TiAl based alloy. *J Mater Sci Technol* 2019;35:2652-7. DOI
34. Schwaighofer E, Clemens H, Mayer S, et al. Microstructural design and mechanical properties of a cast and heat-treated intermetallic multi-phase γ-TiAl based alloy. *Intermetallics* 2014;44:128-40. DOI
35. Ramanujan R. Phase transformations in γ based titanium aluminides. *Int Mater Rev* 2000;45:217-40. DOI
36. Yang G, Ren W, Liu Y, et al. Effect of pre-deformation in the β phase field on the microstructure and texture of the α phase in a boron-added β-solidifying TiAl alloy. *J Alloys Compd* 2018;742:304-11. DOI
37. Hu D, Huang A, Wu X. On the massive phase transformation regime in TiAl alloys: the alloying effect on massive/lamellar competition. *Intermetallics* 2007;15:327-32. DOI
38. Sankaran A, Bouzy E, Humbert M, Hazotte A. Variant selection during nucleation and growth of γ-massive phase in TiAl-based intermetallic alloys. *Acta Materialia* 2009;57:1230-42. DOI
39. Sun YQ. Surface relief and the displacive transformation to the lamellar microstructure in TiAl. *Philosopy Magaz Lett* 1998;78:297-305. DOI
40. Chaturvedi M, Xu Q, Richards N. Development of crack-free welds in a TiAl-based alloy. *J Mater Proc Technol* 2001;118:74-8. DOI
41. Srivastava D, Chang I, Loretto M. The optimisation of processing parameters and characterisation of microstructure of direct laser fabricated TiAl alloy components. *Mater Design* 2000;21:425-33. DOI
42. Denquin A, Naka S. Phase transformation mechanisms involved in two-phase TiAl-based alloys-I. lambellar structure formation. *Acta Materialia* 1996;44:343-52. DOI
43. Kastenhuber M, Rashkova B, Clemens H, Mayer S. Enhancement of creep properties and microstructural stability of intermetallic β-solidifying γ-TiAl based alloys. *Intermetallics* 2015;63:19-26. DOI
44. Bernal D, Chamorro X, Hurtado I, Madariaga I. Evolution of lamellar microstructures in a cast TNM alloy modified with boron through single-step heat treatments. *Intermetallics* 2020;124:106842. DOI
45. Song B, Dong S, Zhang B, Liao H, Coddet C. Effects of processing parameters on microstructure and mechanical property of selective laser melted Ti6Al4V. *Mater Design* 2012;35:120-5. DOI
46. Berteaux O, Popoff F, Thomas M. An experimental assessment of the effects of heat treatment on the microstructure of Ti-47Al-2Cr-2Nb powder compacts. *Metall Mat Trans A* 2008;39:2281-96. DOI
47. Li M, Wu X, Yang Y, et al. TiAl/RGO (reduced graphene oxide) bulk composites with refined microstructure and enhanced nanohardness fabricated by selective laser melting (SLM). *Mater Charact* 2018;143:197-205. DOI
48. Taha AS, Hammad FH. Application of the hall-petch relation to microhardness measurements on Al, Cu, Al-MD 105, and Al-Cu alloys. *Physica Status Solidi* 1990;119:455-62. DOI

Wang *et al. Microstructures* 2022;2:2022020
DOI: 10.20517/microstructures.2022.19

Microstructures

Research Article

Open Access

Check for updates

Chemical unit co-substitution enabling broadband and tunable near-infrared emission in garnet-type $Lu_3Sc_2Ga_3O_{12}:Cr^{3+}$ phosphors

Taoze Wang[1], Gaochao Liu[1], Zhiguo Xia[1,2]

[1]The State Key Laboratory of Luminescent Materials and Devices, Guangdong Provincial Key Laboratory of Fiber Laser Materials and Applied Techniques, School of Materials Science and Engineering, South China University of Technology, Guangzhou 510640, Guangdong, China.
[2]School of Physics and Optoelectronics, South China University of Technology, Guangzhou 510641, Guangdong, China.

Correspondence to: Dr. Zhiguo Xia, The State Key Laboratory of Luminescent Materials and Devices, South China University of Technology, No. 381, Wushan Road, Guangzhou 510641, Guangdong, China. E-mail: xiazg@scut.edu.cn

How to cite this article: Wang T, Liu G, Xia Z. Chemical unit co-substitution enabling broadband and tunable near-infrared emission in garnet-type $Lu_3Sc_2Ga_3O_{12}:Cr^{3+}$ phosphors. *Microstructures* 2022;2:2022020. https://dx.doi.org/10.20517/microstructures.2022.19

Received: 1 Aug 2022 **First Decision:** 1 Sep 2022 **Revised:** 24 Sep 2022 **Accepted:** 27 Sep 2022 **Published:** 10 Oct 2022

Academic Editor: Xiaozhou Liao **Copy Editor**: Fangling Lan **Production Editor:** Fangling Lan

Abstract

Although near-infrared phosphor-converted light-emitting diodes (NIR pc-LEDs) are desired for non-visible light source applications, the design of broadband NIR phosphors remains a challenge. Inspired by the chemical unit co-substitution strategy for the modification of composition and local structure, we realize a tunable redshift emission from 706 to 765 nm in garnet-type $Lu_3Sc_2Ga_3O_{12}:Cr^{3+}$ with a broadened full width at half maximum and enhanced photoluminescence intensity by introducing a [Mg^{2+}-Si^{4+}] unit into the [Sc^{3+}-Ga^{3+}] couple. Structural and spectral analyzes demonstrate that the co-substitution reduces the local symmetry and crystal field strength of the [CrO_6] octahedra, thus leading to inhomogeneous widening of the $^4T_2 \rightarrow {}^4A_2$ emission and enhanced blue absorption. Furthermore, the $^4T_2 \rightarrow {}^4A_2$ emission exhibits a phonon-assisted character at low temperatures due to the thermal coupling effect with the ^2E level. The fabricated NIR pc-LED based on the optimized NIR phosphor exhibits excellent potential in night vision and imaging applications.

Keywords: Near-infrared (NIR), garnet structure, Cr^{3+}-doped phosphor, co-substitution

INTRODUCTION

Broadband near-infrared (NIR, 700-2500 nm) light sources are urgently needed for a variety of applications, including component detection[1], phototherapy[1], agricultural plant lighting[2,3], bioimaging[4], night vision illumination[5] and iris recognition[6]. Among various NIR light sources, however, traditional halogen tungsten lamps suffered from high-power dissipation[7]. Electroluminescent semiconductors, such as GaAs, are inappropriate for various applications due to their narrow emission band[8,9]. Furthermore, organic light-emitting diodes (LEDs) suffer from low hydrothermal stability[10]. In contrast, NIR phosphor-converted (pc)-LEDs that are encapsulated by blue light InGaN chips and NIR-emitting phosphors are emerging as promising candidates to achieve the desired broadband NIR emission. Owing to the commercialization of high-efficiency blue chips[11,12], the development of NIR phosphors pumped by blue light with broadband and tunable emission has become a research priority[13].

So far, several types of NIR phosphors have been explored by doping Eu^{2+}[14,15], Bi[16], Ni^{2+}[17], Mn^{4+}[18] and Cr^{3+} into inorganic hosts. Among these dopants, Cr^{3+} has gradually become the focus of attention for practical applications due to its high photoluminescence quantum yield[19-21], broadband and tunable emission[22,23] and high thermal stability[24-26]. In addition, the $^4A_2 \rightarrow {}^4T_1$ transition of Cr^{3+} perfectly matches the blue light chip, as well as a narrowband or tunable broadband emission sensitive to the crystal environment due to the $3d^3$ electronic configuration. Among the different hosts for Cr^{3+} doping, garnet-type compounds possess a compact structure with high symmetry belonging to the cubic system[27] and have been extensively studied for high-performance NIR phosphors.

The garnet-type structure is composed of three kinds of polyhedra, namely, dodecahedra, mainly occupied by elements with large radii, such as rare earth elements and alkali and alkaline earth metals, octahedra, occupied by transition and main group metals with small radii, and tetrahedra, usually occupied by Ga, Si, Ge, Al, V and P. In recent years, Cr^{3+}-doped garnet phosphors with high internal quantum efficiency (IQE) have been reported and studied. However, owing to the parity-forbidden character of *d-d* transitions, Cr^{3+}-doped phosphors suffer from a low absorption coefficient (Abs) and narrow emission band. This is particularly true for highly symmetrical lattices, including $Ca_3Sc_2Si_3O_{12}:Cr^{3+}$ (IQE/Abs = 92.3%/27.6%, FWHM = 110 nm)[28] and $Gd_3Sc_2Ga_3O_{12}:Cr^{3+}$ (IQE/Abs = 98.6%/21.0%, FWHM = 120 nm)[29], which limits the further application of NIR pc-LEDs. Although the Abs can be raised by increasing the concentration of Cr^{3+}, excessive dopants usually lead to serious concentration quenching effects and stronger electron-phonon coupling, resulting in damage to the thermal stability and IQE in the garnet structure[30,31]. Although Cr^{3+} and Yb^{3+} co-doping may benefit the broadening emission spectrum and enhance the thermal stability, it has little effect on improving the Abs[32]. It has been reported that introducing the odd-parity crystal field by lattice distortion can partly release the parity-forbidden character of Cr^{3+} ions so that an improved Abs is expected[33].

In recent years, the chemical unit co-substitution strategy, i.e., the simultaneous substitution of two kinds of chemical units in a crystal structure, has been used to realize structural evolution and the regulation of luminescence properties, as proposed by our group and successfully adopted by many different research teams[34]. Benefitting from the high structural tolerance of the garnet structure, chemical units can enter the cell in large quantities to realize the distortion of the polyhedra and the disorder of the local crystal environment, further breaking the reverse symmetry of the crystal site, where Cr^{3+} is located. Thus it leads to a strong crystal field splitting and contributes to the photoluminescence tuning of the emission band.

In this work, an enhanced NIR emission of Cr^{3+} ions with a broadened FWHM is realized by co-substituting [Mg^{2+}-Si^{4+}] for [Sc^{3+}-Ga^{3+}] in garnet-type $Lu_3Sc_{1.98-x}Mg_xGa_{3-x}Si_xO_{12}:0.02Cr^{3+}$ phosphors. The luminescence

properties and crystal field strength of the phosphors are further studied as a function of *x*. We find that the thermal coupling effect of the $^4T_2$ and ^2E levels and the electron-phonon coupling effect are enhanced with increasing *x* and the related luminescence mechanism is proposed. Finally, a broadband NIR pc-LED is designed and fabricated using the composition-optimized phosphor $Lu_3Sc_{1.38}Mg_{0.6}Ga_{2.4}Si_{0.6}O_{12}$:0.02$Cr^{3+}$ (LSMGS:Cr) and its applications in imaging and night vision illuminating are demonstrated.

MATERIALS AND METHODS

Materials and preparation

The $Lu_3Sc_{1.98-x}Mg_xGa_{3-x}Si_xO_{12}$:0.02$Cr^{3+}$ samples (x = 0.0, 0.30, 0.45, 0.60, 0.75 or 0.90) were prepared by a conventional high-temperature solid-state method. Lu_2O_3 (99.9%, Aladdin), Sc_2O_3 (99.9%, Aladdin), MgO (99.9%, Aladdin), Ga_2O_3 (99.99%, Aladdin), SiO_2 (99.99%, Macklin) and Cr_2O_3 (99.95%, Aladdin) were used as the starting materials and weighed according to stoichiometric proportions, with 2 wt.% H_3BO_3 (99.5%, Aladdin) added as the flux. After being mixed and grounded thoroughly using ethanol in an agate mortar, the mixtures were transferred into alumina crucibles (Kaiping Shengxing Chemical Porcelain Factory, Tangshan, 16 × 28 mm) and then placed in a box furnace for sintering at 1450 °C for 6 h in air. Finally, the phosphors were ground in an agate mortar for 3 min after cooling to room temperature.

Characterization

Powder X-ray diffraction patterns were measured using a diffractometer (PANalytical Corporation, Netherlands) with a Cu Kα radiation source (λ = 1.5406 Å) and the operating voltage and current set as 40 kV and 15 mA, respectively. Room-temperature photoluminescence (PL) and photoluminescence excitation (PLE) spectra were recorded using an FLS1000 fluorescence spectrophotometer (Edinburgh Instruments, UK) equipped with a continuous xenon lamp (450 W) as the excitation source and a liquid-nitrogen cooled NIR photomultiplier tube as the detector (Hamamatsu, R5509, InP/InGaAsP). Low-temperature spectra were measured using the same spectrophotometer equipped with a Cryo-77 low-temperature fluorescence instrument (Tian Jin Orient - KOJI Instrument Co., Ltd.). The PL decay curve was also measured using the same spectrophotometer with a microsecond flash lamp (μF900) as the excitation source. High-temperature spectra were measured by a fiber spectrophotometer (NOVA high-sensitivity spectrometer, Idea Optics, China) equipped with a TAP-02 high-temperature fluorescence instrument (Tian Jin Orient - KOJI Instrument Co., Ltd.) and a 450 nm laser diode as the excitation source. Diffuse reflection (DR) spectra were collected using a UV-Vis-NIR spectrophotometer (Hitachi UH4150) and $BaSO_4$ was used as the reference standard. The quantum efficiency at room temperature was measured by an absolute PL quantum yield spectrometer (Quantaurus-QY Plus C13534-12, Hamamatsu Photonics).

LED device fabrication and performance measurements

The pc-NIR LED device was designed and made by coating the as-prepared phosphor on a blue LED (X1901, 5 W, Guangzhou LEDteen Optoelectronics Co., Ltd., China) and fully blending with an epoxy resin. The electroluminescence of the fabricated NIR pc-LED was measured by Optical & Electrical Fast Meters For LEDS (Hangzhou Hopoo Optoelectronics Technology Co., Ltd., China).

RESULTS AND DISCUSSION

Crystal structure of $Lu_3(Sc, Mg)_2(Ga, Si)_3O_{12}:Cr^{3+}$

The phase and purity of the as-prepared powder samples were examined by X-ray diffraction and the results are shown in Figure 1A. The *x* value reflects the degree of co-substitution of [Mg^{2+}-Si^{4+}] for [Sc^{3+}-Ga^{3+}]. All diffraction peaks were well matched with the standard data of the $Lu_3Sc_2Ga_3O_{12}$ cubic phase (PDF No. 54-1252, space group *Ia*-3*d*) and no obvious impurity phases were observed, indicating that the phase of the samples was not affected by a certain amount of chemical unit co-substitution due to the high structural tolerance of garnet-type compounds as shown in Figure 1C.

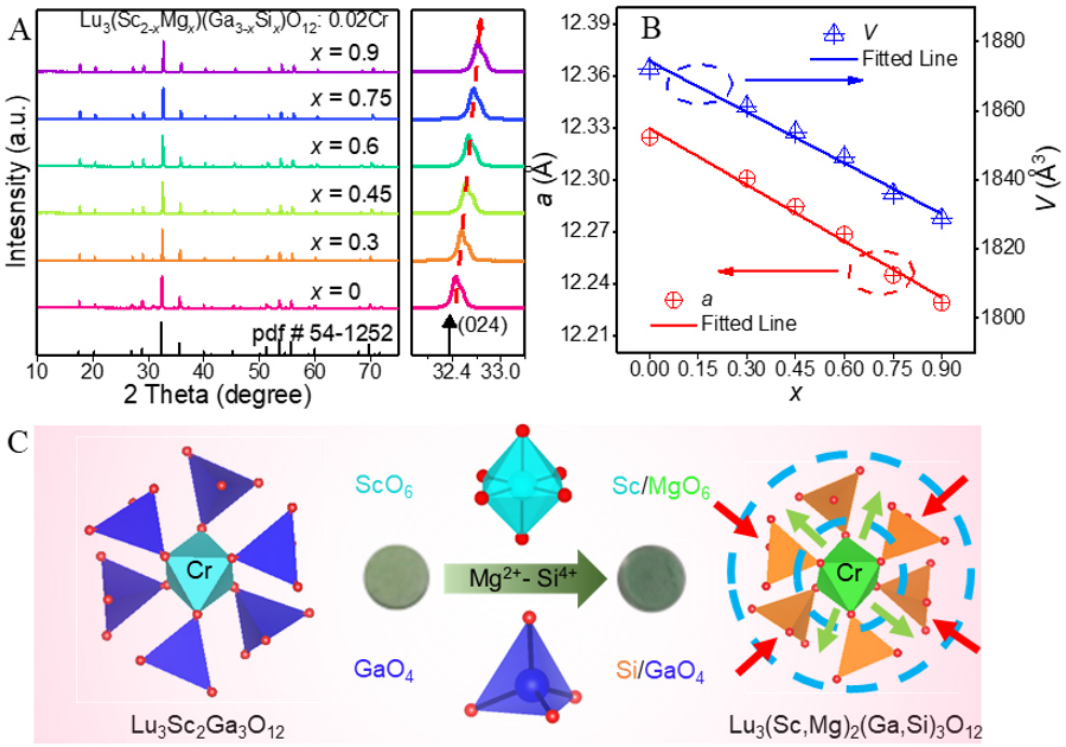

Figure 1. (A) XRD patterns of $Lu_3Sc_{1.98-x}MgxGa_{3-x}SixO_{12}$:0.02$Cr^{3+}$ (x = 0.0-0.9) with selected diffraction peak near 32.7°. (B) Calculated lattice parameters of $Lu_3Sc_{1.98-x}MgxGa_{3-x}SixO_{12}$:0.02$Cr^{3+}$ (x = 0.0-0.9). (C) Crystal structure of $Lu_3Sc_{1.98-x}MgxGa_{3-x}SixO_{12}$:0.02$Cr^{3+}$.

The shift of the strongest diffraction peak to a higher angle, as shown in Figure 1A, indicates that the cell shrinks with increasing x. With the substitution of [Mg^{2+}-Si^{4+}] for [Sc^{3+}-Ga^{3+}], the diffraction peak near 32.7° shifts slightly toward a higher angle [Figure 1A] due to the ionic radii of Mg^{2+} [0.72 Å, coordination number (CN) = 6] and Si^{4+} (0.26 Å, CN = 4) being smaller than that of Sc^{3+} (0.745 Å, CN = 6) and Ga^{3+} (0.47 Å, CN = 4), respectively[35]. The lattice parameter of the phosphors in the cubic system was calculated using the Bragg equation:

$$2d\sin\theta = \lambda \quad (1)$$

$$\frac{1}{d^2} = \frac{h^2+k^2+l^2}{a^2} \quad (2)$$

where d and a represent the interplanar spacing and lattice parameter, respectively. The wavelength of the incidence X-ray λ was 1.5406 Å. The diffraction peak position θ originating from the crystal face (hkl) was obtained from the strongest diffraction peak near 32.7° in Figure 1A, where h, k and l are the Miller indices, namely, 0, 2 and 4, respectively, in the calculation. The lattice parameter decreased from 12.32 to 12.23 Å with increasing x, as shown in Figure 1B. This indicates that the [Mg^{2+}-Si^{4+}] chemical unit had been successfully incorporated into the garnet-type structure. The shrinkage of the crystal cell usually enhances the crystal field strength of the octahedrally-coordinated Cr^{3+} center with a blueshift and narrowed emission band. In contrast, a completely opposite phenomenon in $Lu_3Sc_2Ga_3O_{12}$:Cr^{3+} can be observed after the [Mg^{2+}-Si^{4+}] chemical unit was introduced, as discussed below.

Photoluminescence properties of $Lu_3(Sc, Mg)_2(Ga, Si)O_{12}:Cr^{3+}$

The room-temperature emission (PL) and excitation (PLE) spectra of $Lu_3Sc_{1.98}Ga_3O_{12}:0.02Cr^{3+}$ are shown in Figure 2A. Under the excitation of 440 nm blue light, $Lu_3Sc_{1.98}Ga_3O_{12}:0.02Cr^{3+}$ exhibits a dark-red emission with a FWHM of 88 nm centered at 706 nm, which is attributed to the $^2E \rightarrow {}^4A_{2g}$ transition of Cr^{3+}. When monitored at the 706 nm emission, $Lu_3Sc_{1.98}Ga_3O_{12}:0.02Cr^{3+}$ gave three excitation bands in the UV, blue and red regions, which were assigned to the $^4A_2 \rightarrow {}^4T_1$ (^4P), $^4A_2 \rightarrow {}^4T_1$ (^4F) and $^4A_2 \rightarrow {}^4T_2$ (^4F) transitions of Cr^{3+}, respectively. After the [Mg^{2+}-Si^{4+}] unit replaces the [Sc^{3+}-Ga^{3+}] couple in the structure, the emission band position gradually shifts from 706 to 765 nm. Furthermore, the FWHM is doubled to 176 nm [Figure 2B]. The $Lu_3Sc_{1.38}Mg_{0.6}Ga_{2.4}Si_{0.6}O_{12}:0.02Cr^{3+}$ phosphor has a broadband NIR emission with stronger penetrability and crypticity, which is more conducive to its application in biological imaging and component analysis compared to $Lu_3Sc_{1.98}Ga_3O_{12}:0.02Cr^{3+}$ with a narrowband visible dark-red emission.

The change in the spectrum can be divided into two stages, as shown in Figure 2C. In the first stage (x = 0.0-0.45), the emission band position rapidly redshifts and the FWHM increases significantly, mainly as a result of the enhancement of the broadband $^4T_2 \rightarrow {}^4A_2$ emission, indicating that the excited electrons gradually tend to populate at the $^4T_2$ state rather than the ^2E state. The enhancement of the parity-forbidden $^4T_2 \rightarrow {}^4A_2$ transition is a common phenomenon in garnet oxide solid solutions[36] and is usually caused by the disordered local crystal environment of Cr^{3+} due to the introduction of the chemical unit. In the second stage (x = 0.6-0.9), the values of the emission band position and FWHM increased slowly and finally converged to a constant. This may be caused by two competing factors. The first is the crystal field enhancement caused by the lattice contraction discussed previously, which usually engenders the blueshift and sharpens the Cr^{3+} emission. The second factor is the disordered local crystal environment, which usually engenders the redshift and broadens the Cr^{3+} emission.

Because of the lack of protection from an external shell, the orbital energy levels of the *d* orbital of Cr^{3+} are very sensitive to the influence of the host lattice. Therefore, to explore the further influence of the [Mg^{2+}-Si^{4+}] chemical unit substitution on the emission properties of Cr^{3+}, it is necessary to quantitatively calculate the crystal field splitting parameters, including *Dq*, *B* and *C*. According to crystal field theory, the crystal field strength parameter *Dq* and Racah parameter *B* can be approximated by the following equations[37]:

$$10Dq = E(^4T_{2g}) \tag{3}$$

$$\frac{Dq}{B} = \frac{15(\Delta E / Dq - 8)}{(\Delta E / Dq)^2 - 10(\Delta E / Dq)} \tag{4}$$

$$\Delta E = E(^4T_{1g}) - E(^4T_{2g}) \tag{5}$$

Finally, the Racah parameter *C* can be calculated by:

$$E(^2E) = 3.05C + 7.9B - 1.8B^2 / Dq \tag{6}$$

where $E(^4T_{1g})$ and $E(^4T_{2g})$ are the energy levels of $^4T_{1g}(^4F)$ and $^4T_{2g}(^4F)$ for Cr^{3+}, respectively, which can be obtained from the PLE spectra, and $E(^2E)$ is the equilibrium position of the sharp zero-photon line (ZPL) obtained from the PL spectra.

The Racah parameter *B* represents the repulsion between electrons in the 3*d* orbital of Cr^{3+}. The value of the Racah parameter *B* of Cr^{3+} in the host is usually lower than in the free environment (B_0 = 918 cm^{-1}) and

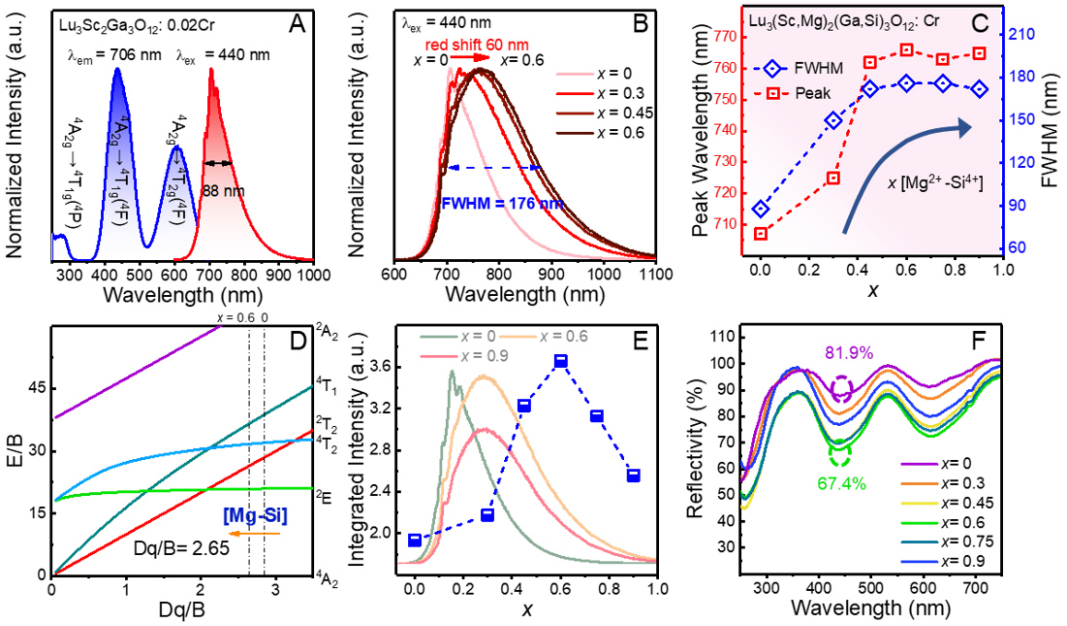

Figure 2. (A) Room-temperature PLE (blue) and PL (red) spectra of $Lu_3Sc_{1.98}Ga_3O_{12}$:0.02Cr^{3+} phosphor. (B) Normalized PL spectra of $Lu_3Sc_{1.98-x}MgxGa_{3-x}SixO_{12}$:0.02$Cr^{3+}$ (x = 0.0-0.6) excited by 440 nm light. (C) Peak wavelength and FWHM of $Lu_3Sc_{1.98-x}MgxGa_{3-x}SixO_{12}$:0.02$Cr^{3+}$ (x = 0.0-0.9). (D) Tanabe-Sugano diagram of Cr^{3+} in the perfect octahedral environment. (E) Integrated intensity of PL spectra of $Lu_3Sc_{1.98-x}MgxGa_{3-x}SixO_{12}$:0.02$Cr^{3+}$ (x = 0.0-0.9) excited by 440 nm light. (F) DR spectra of $Lu_3Sc_{1.98-x}MgxGa_{3-x}SixO_{12}$:0.02 Cr^{3+} (x = 0.0-0.9).

strongly depends on the covalency of the host. Accordingly, the specific crystal field parameters of $Lu_3Sc_{1.98-x}Mg_xGa_{3-x}Si_xO_{12}$:0.02$Cr^{3+}$ (x = 0.0, 0.6 or 0.9) were calculated, as listed in Table 1. The value of *Dq/B* decreases from 2.85 to 2.65 with increasing x value, thus reducing the energy separation between $^4T_{2g}$ and ^2E [Figure 2D]. The decreased *B* values indicate that the ionic character of the octahedra in which Cr^{3+} is located is enhanced due to the enlargement of the [Sc/MgO_6] octahedra, even though the whole crystal cell shrinks under co-substitution[38]. Therefore, the excited electrons will tend to reside in the gradually redshifted $^4T_{2g}$ level due to the weakening crystal field and induction of a broad NIR emission ($^4T_2 \rightarrow {}^4A_2$). As shown in Figure 2E, with increasing x, the integral intensity of $Lu_3Sc_{1.98-x}Mg_xGa_{3-x}Si_xO_{12}$:0.02$Cr^{3+}$ increased to 180% of the original value at first (x = 0.0-0.6) and then decreased (x = 0.6-0.9). Figure 2F shows the DR spectra of the $Lu_3Sc_{1.98-x}Mg_xGa_{3-x}Si_xO_{12}$:0.02$Cr^{3+}$ series. The three absorption bands of Cr^{3+} in the UV-Vis region fit well with the three excitation bands of the PLE spectra. With the introduction of [Mg^{2+}-Si^{4+}] chemical units in the structure (x = 0.0-0.6), the reflectance at 440 nm reduces from 81.9% for x = 0.0 to 67.4% for x = 0.6, which indicates that more blue light was absorbed by the optimized phosphor.

The external quantum efficiency (EQE) of the designed phosphors is crucial for high-performance NIR LEDs and is the product of the internal quantum efficiency (IQE) and Abs[39,40]. The quantum yield of the samples was measured and the values of the EQE, IQE and Abs are shown in Figure 3A. The matrix garnet phosphor (x = 0.0) shows a high IQE of up to 81.4% and a low Abs (0.257) due to the parity-forbidden transition of Cr^{3+}. The [Mg^{2+}-Si^{4+}] co-substituted phosphor (x = 0.6) demonstrated a higher EQE (28.1%) compared to the matrix phosphor (20.9%) on account of the improvement of the absorption ability from 25.7% (light green body color) to 38.4% (deep green body color). Excessive [Mg^{2+}-Si^{4+}] chemical units were harmful to the luminescence ability of the $Lu_3Sc_{1.98-x}Mg_xGa_{3-x}Si_xO_{12}$:0.02$Cr^{3+}$ phosphors (x = 0.75 or 0.90), which is consistent with the trend of the integral intensity of the PL spectra [Figure 2E]. The decreased trend of the Abs of $Lu_3Sc_{1.98-x}Mg_xGa_{3-x}Si_xO_{12}$:0.02$Cr^{3+}$ phosphors (x = 0.75 or 0.90) may be caused by more

Table 1. Crystal field parameters of $Lu_3Sc_{1.98-x}Mg_xGa_{3-x}Si_xO_{12}$:0.02$Cr^{3+}$ (x = 0.0, 0.6 or 0.9) phosphors

Host	*Dq* (cm^{-1})	*B* (cm^{-1})	*Dq/B*	*C* (cm^{-1})
x = 0	1514	531	2.85	3499
x= 0.6	1463	553	2.65	3445
x = 0.9	1460	556	2.62	3415

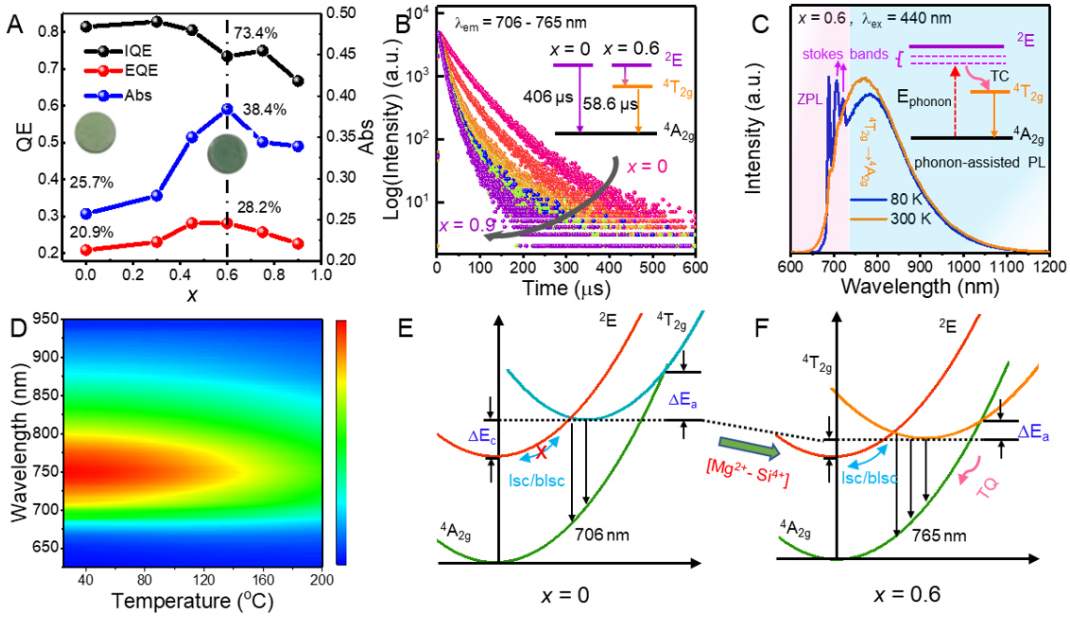

Figure 3. (A) IQE, Abs and EQE values of $Lu_3Sc_{1.98-x}MgxGa_{3-x}SixO_{12}$:0.02$Cr^{3+}$ phosphors. (B) Luminescence decay curves of $Lu_3Sc_{1.98-x}MgxGa_{3-x}SixO_{12}$:0.02$Cr^{3+}$ phosphors (x = 0.0-0.9) excited by 440 nm light and monitored at their strongest emission wavelength. (C) Temperature-dependent PL spectra and phonon-assisted PL mechanism of LSMGS:Cr excited by 440 nm light at 80 and 300 K. (D) PL/temperature correlation maps of LSMGS:Cr excited by 440 nm light. (E) and (F) Configuration coordinate diagrams of $Lu_3Sc_{1.98-x}MgxGa_{3-x}SixO_{12}$:0.02$Cr^{3+}$ (x = 0.0 or 0.6) showing level thermal coupling and temperature-quenching mechanisms.

serious diffuse reflection due to the mismatched refractive index between the garnet phase and the impurities.

The experiment results show that the PL decay curves can only be fitted with a bi-exponential function [Figure 3B]:

$$I(t) = A_1 e^{-\frac{t}{\tau_1}} + A_2 e^{-\frac{t}{\tau_2}} \quad (7)$$

where $I(t)$ represents the emission intensity at a certain time t, A_1 and A_2 are constants and τ_1 and τ_2 are the luminescence decay times. According to the above equation, the decay times were determined to be 406.1, 218.4 and 195.3 μs for τ_1 and 185.1, 58.6 and 56.0 μs for τ_2, corresponding to the x = 0.0, 0.6 or 0.9 samples, respectively. It is known that Cr^{3+} generally exists stably at octahedral sites. Although Cr^{3+} will occupy both octahedral and dodecahedral sites in some garnet oxides, the PL band of Cr^{3+} at dodecahedral sites usually exhibits longwave PL (> 800 nm) due to the larger radius of the polyhedra[31]. Thus, the bi-exponential PL decay was more likely caused by one crystallographic site with multiple local crystal environments.

The two lifetimes with different orders can be attributed to the $^2E \rightarrow {}^4A_{2g}$ and $^4T_{2g} \rightarrow {}^4A_{2g}$ transition, respectively. The $^2E \rightarrow {}^4A_{2g}$ transition is both parity-forbidden and spin-forbidden, while the $^4T_{2g} \rightarrow {}^4A_{2g}$ transition is parity-forbidden but spin-allowed, which causes the former to have a longer lifetime. The transition from the ^2E state becomes partially allowed due to the overlap between the wavefunctions of the ^2E and $^4T_2$ states, which explains the shorter decay time in the phosphors after co-substitution. This phenomenon suggests that the excited electrons are populated at both the ^2E and $^4T_{2g}$ levels, which further indicates that Cr^{3+} in $Lu_3Sc_{1.98-x}Mg_xGa_{3-x}Si_xO_{12}$ may possess more than one set of Dq/B values, which also explains why the total crystal field strength calculated in Figure 2D was not at a medium level and the inhomogeneous broadening in the PL spectra. The bi-exponential decay of the matrix may be caused by anti-site defects, which were previously reported in $Lu_3Sc_2Ga_3O_{12}:Cr^{3+}$[41]. Overall, co-substitution will induce a local structural distortion and then introduce sites with weaker crystal field strength, as well as the partial lifting of the forbidden $^4T_{2g} \rightarrow {}^4A_{2g}$ transition due to the high symmetry. The phenomenon where two luminescence components in the inhomogeneous broadening PL spectra can be detected when monitored at a certain wavelength, indicating the nonnegligible thermal coupling of the ^2E and $^4T_{2g}$ levels, as discussed below. The PL lifetimes decreased with increasing x [Supplementary Figure 1] due to the partial lifting of the restriction on the forbidden transition and the increase in the probability of the non-radiative transition.

To investigate the detailed luminescence mechanism herein, the low-temperature-dependent PL spectra and PL decay curves of LSMGS:Cr were recorded and compared in Figure 3C, Supplementary Figures 2 and 3. At 80 K, the PL spectra of LSMGS:Cr consist of a sharp ZPL, namely, the $^2E \rightarrow {}^4A_{2g}$ transition at 690 nm and the attached stokes sideband (705 and 720 nm) due to the participation of phonons. The $^4T_{2g} \rightarrow {}^4A_{2g}$ transition presented as a broadband emission centered at 785 nm. With increasing temperature, the intensity of the $^2E \rightarrow {}^4A_{2g}/{}^4T_{2g} \rightarrow {}^4A_{2g}$ transition enhanced at first and then decreased significantly when the temperature exceeded 125 K. This similar phenomenon related to the ZPL and Stokes sideband also exists in other transition metal-doped phosphors with the $3d^3$ electronic configuration, such as V^{2+} and Mn^{4+}[42,43]. The dopants in the host introduce point defects, which can accept energy from not only photons but also phonons in the host lattice to produce luminescence. The latter, known as phonon-assisted emission, will be enhanced by more phonons according to the Bose-Einstein distribution law when heating from a low temperature. When the temperature is raised to a specific level, the large number of phonons induces serious electron-phonon coupling, which leads to thermal quenching.

The $^4T_{2g} \rightarrow {}^4A_{2g}$ emission with the same behavior was abnormal compared to other Cr-doped phosphors. Generally, phosphors at low temperatures exhibit a stronger emission because the lattice vibration is inhibited, which weakens the electron-phonon coupling effect and causes a smaller probability of non-radiative transition. The abnormal $^4T_{2g} \rightarrow {}^4A_{2g}$ PL behavior related to the temperature indicates that the thermal coupling effect between the ^2E and $^4T_{2g}$ levels did exist in $Lu_3Sc_{1.98-x}Mg_xGa_{3-x}Si_xO_{12}:0.02Cr^{3+}$ so that the phonon energy can transfer between these two levels by back-intersystem crossing/intersystem crossing (blsc/lsc)[44]. The phonon-assisted emission was also present in the solid solution with $x = 0.45$, as shown in Supplementary Figure 4. In addition, the PL decay also can be fitted with a bi-exponential function with a reduced lifetime compared with that at 80 K due to the increasing portion of $^4T_{2g} \rightarrow {}^4A_{2g}$ emission during the blsc process and more serious electron-phonon coupling. In the Cr-doped phosphor, weakening of the crystal field strength caused by lattice thermal expansion with increasing temperature leads to a redshift in the PL spectra. In LSMGS:Cr, however, the emission center with a larger Stokes shift will suffer more serious thermal quenching, resulting in the 20 nm blueshift of the emission spectrum at high temperature, which is common in disordered local crystal environment, such as Cr-doped glasses[45], which further proves the disorder of the local structure in LSMGS:Cr. Even though the non-radiative transition to some extent exists in the LSMGS:Cr, it still retains 75% at 423 K of the initial intensity measured at room temperature

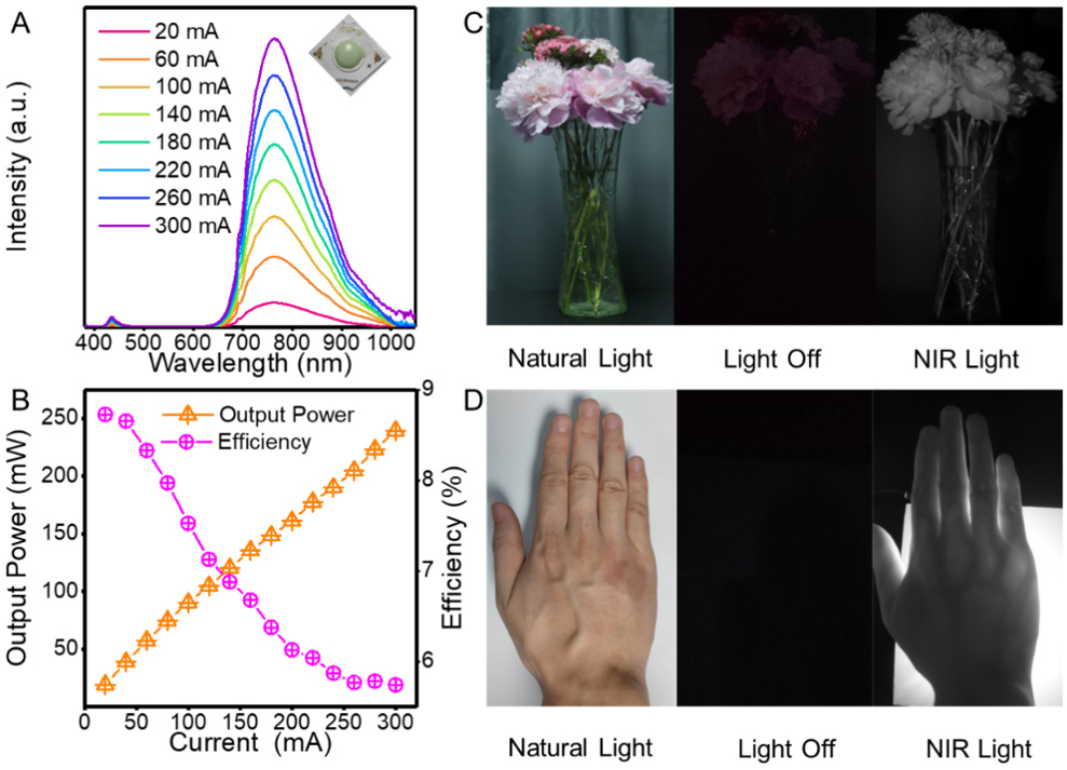

Figure 4. (A) Photograph and luminescence spectra of as-fabricated NIR pc-LED. (B) NIR output power and photoelectric efficiency of pc-LED measured at current from 20 to 300 mA. (C) Photographs of bouquet under natural and NIR light captured by different cameras. (D) Photographs of NIR light transilluminating human palm.

and maintains fine color stability [Figure 3D and Supplementary Figure 5], which benefits from the high structural rigidity of the garnet.

In summary, the mechanism of [Mg^{2+}-Si^{4+}] co-substitution on the regulation of optical properties can be qualitatively explained, as shown in Figure 3E and F. The [Mg^{2+}-Si^{4+}] chemical units not only introduce more multiple local crystal environments but also reduce the energy level gap ΔE_c between $^4T_{2g}$ and ^2E, which is closely related to the crystal field strength. Thus, the energy level thermal coupling enhances, which allows part of the excited electrons at the ^2E level can also populate into the $^4T_{2g}$ level through the back-intersystem crossing process with increasing x and eventually leads to the transition from a short wavelength sharp emission to a long wavelength broad emission. However, the weak crystal field strength simultaneously causes the reduction of the thermal activation barrier ΔE_a, which causes more serious electron-phonon coupling and thermal quenching, thereby weakening the luminescence performance, which is consistent with the results of the luminescence analysis and thermal stability [Figures 2E and 3A; Supplementary Figure 6].

Application in a NIR pc-LED

To demonstrate the potential application of NIR pc-LEDs in night vision illumination and the penetrating imaging of biological tissue, a broadband NIR pc-LED device was designed and fabricated using the LSMGS:Cr (x = 0.6) phosphor on a blue light-emitting InGaN chip (440 nm), as shown in Figure 4A. The NIR output power continuously increases with the drive current and reaches 90.3 mW at 100 mA. Furthermore, the photoelectric efficiency of pc-LED drops from 8.73% to 5.74% due to the efficiency drop of LED chips, as shown in Figure 4B. Figure 4C shows that a bouquet can be vividly captured by a NIR camera

using a 720 nm long-pass filter under the non-visible illumination of the NIR pc-LED, which shows the feasibility of its application in night vision. The veins of a human palm can be distinguished, as shown in Figure 4D, using NIR light to penetrate and a NIR camera to capture, because NIR light has a good penetrability through biological tissue and veins have a specific absorption of NIR light. This fundamental demonstration indicates that the LSMGS:Cr phosphors can be potentially applied in machine vision and non-destructive examination.

CONCLUSIONS

Broadband NIR phosphors $Lu_3Sc_{1.98-x}Mg_xGa_{3-x}Si_xO_{12}:0.02Cr^{3+}$ (x = 0.0-0.9) with tunable emission were successfully fabricated by a high-temperature solid-state method. The shrinkage of the crystal cell and pure phase were verified by XRD analysis. By co-substituting [Sc^{3+}-Ga^{3+}] with [Mg^{2+}-Si^{4+}] chemical units in the garnet host with high symmetry, the [CrO_6] octahedra were distorted, thus breaking the inversion symmetry and leading to the broadband $^4T_2 \rightarrow {}^4A_2$ emission. Furthermore, the [Mg^{2+}-Si^{4+}] pairs strengthened the thermal coupling between the $^4T_2$ and ^2E levels due to the weakened crystal field strength, resulting in both sharp ZPL and broad emissions. Under 440 nm blue light excitation, the composition-optimized garnet-type solid solution demonstrated an inhomogeneous widening NIR emission maximized at 765 nm, with a large FWHM of 176 nm and highest EQE/Abs of 28.2 %/38.4% for the composition of x = 0.6 ($Lu_3Sc_{1.38}Mg_{0.6}Ga_{2.4}Si_{0.6}O_{12}:0.02Cr^{3+}$). The fabricated broadband NIR pc-LED showed a light outpower of 90.3 mW at 100 mA with a photoelectric efficiency of 7.5%, demonstrating its application potential in multiple fields.

DECLARATIONS

Authors' contributions

Conceived and drafted the manuscript: Xia Z, Wang T
Prepared material and device, performed characterization: Wang T
Performed data analysis: Wang T, Liu G
Revised the manuscript: Xia Z

Availability of data and materials

The data that support the findings of this study are available from the corresponding author upon reasonable request.

Financial support and sponsorship

The work was supported by International Cooperation Project of National Key Research and Development Program of China (2021YFB3500400 and 2021YFE0105700), the National Natural Science Foundations of China (Grant Nos. 51972118), Guangzhou Science & Technology Project (202007020005), and the Local Innovative and Research Teams Project of Guangdong Pearl River Talents Program (2017BT01X137).

Conflicts of interest

All authors declared that there are no conflicts of interest.

Ethical approval and consent to participate

Not applicable.

Consent for publication

Not applicable.

REFERENCES

1. Liu G, Molokeev MS, Xia Z. Structural rigidity control toward Cr^{3+} -based broadband near-infrared luminescence with enhanced thermal stability. *Chem Mater* 2022;34:1376-84. DOI
2. Li J, Cui D, Huang J, et al. Organic semiconducting pro-nanostimulants for near-infrared photoactivatable cancer immunotherapy. *Angew Chem Int Ed Engl* 2019;58:12680-7. DOI PubMed
3. Zhang L, Wang D, Yang K, et al. Mitochondria-targeted artificial "nano-rbcs" for amplified synergistic cancer phototherapy by a single NIR irradiation. *Adv Sci (Weinh)* 2018;5:1800049. DOI PubMed PMC
4. Zou X, Wang X, Zhang H, et al. A highly efficient and suitable spectral profile Cr^{3+}-doped garnet near-infrared emitting phosphor for regulating photomorphogenesis of plants. *Chem Eng J* 2022;428:132003. DOI
5. Liu D, Li G, Dang P, et al. Simultaneous broadening and enhancement of Cr^{3+} photoluminescence in $LiIn_2$ SbO_6 by chemical unit cosubstitution: night-vision and near-infrared spectroscopy detection applications. *Angew Chem Int Ed Engl* 2021;60:14644-9. DOI PubMed
6. Nguyen DT, Baek NR, Pham TD, Park KR. Presentation attack detection for iris recognition system using NIR camera sensor. *Sensors (Basel)* 2018;18:1315. DOI PubMed PMC
7. Rajendran V, Chang H, Liu R. Recent progress on broadband near-infrared phosphors-converted light emitting diodes for future miniature spectrometers. *Opt Mater* 2019;1:100011. DOI
8. Zhang Y, Qiao J. Near-infrared emitting iridium complexes: molecular design, photophysical properties, and related applications. *iScience* 2021;24:102858. DOI PubMed PMC
9. Lukovic M, Lukovic V, Belca I, Kasalica B, Stanimirovic I, Vicic M. LED-based vis-NIR spectrally tunable light source - the optimization algorithm. *J Eur Opt Soc -Rapid Publ* 2016:12. DOI
10. Liu H, Zhong H, Zheng F, et al. Near-infrared lead chalcogenide quantum dots: synthesis and applications in light emitting diodes*. *Chin Phys B* 2019;28:128504. DOI
11. Liu G, Hu T, Molokeev MS, Xia Z. Li/Na substitution and Yb^{3+} co-doping enabling tunable near-infrared emission in $LiIn_2SbO_6$:Cr^{3+} phosphors for light-emitting diodes. *iScience* 2021;24:102250. DOI PubMed PMC
12. Qiao J, Zhou G, Zhou Y, Zhang Q, Xia Z. Divalent europium-doped near-infrared-emitting phosphor for light-emitting diodes. *Nat Commun* 2019;10:5267. DOI PubMed PMC
13. Dai D, Wang Z, Xing Z, et al. Broad band emission near-infrared material Mg3Ga2GeO8:Cr^{3+}: substitution of Ga-In, structural modification, luminescence property and application for high efficiency LED. *J Alloys Compd* 2019;806:926-38. DOI
14. Berezovskaya I, Dotsenko V, Voloshinovskii A, Smola S. Near infrared emission of Eu^{2+} ions in $Ca_3Sc_2Si_3O_{12}$. *Chem Phys Lett* 2013;585:11-4. DOI
15. Qiao J, Zhang S, Zhou X, Chen W, Gautier R, Xia Z. Near-infrared light-emitting diodes utilizing a Europium-activated calcium oxide phosphor with external quantum efficiency of up to 54.7%. *Adv Mater* 2022;34:e2201887. DOI PubMed
16. Xiong PX, Li YY, Peng MY. Recent advances in super broad infrared luminescence bismuth-doped crystals. *IScience* 2020;23:101578. DOI PubMed PMC
17. Matuszewska C, Marciniak L. The influence of host material on NIR II and NIR III emitting Ni^{2+}-based luminescent thermometers in $ATiO_3$: Ni^{2+} (A = Sr, Ca, Mg, Ba) nanocrystals. *J Lumin* 2020;223:117221. DOI
18. Du J, Poelman D. Near-infrared persistent luminescence in Mn^{4+} doped perovskite type solid solutions. *Ceram Int* 2019;45:8345-53. DOI
19. Nie W, Yao L, Chen G, et al. A novel Cr^{3+}-doped $Lu_2CaMg_2Si_3O_{12}$ garnet phosphor with broadband emission for near-infrared applications. *Dalton Trans* 2021;50:8446-56. DOI PubMed
20. Nie W, Li Y, Zuo J, et al. Cr^{3+}-activated Na_3 X_2 Li_3 F_{12} (X = Al, Ga, or In) garnet phosphors with broadband NIR emission and high luminescence efficiency for potential biomedical application. *J Mater Chem C* 2021;9:15230-41. DOI
21. You L, Tian R, Zhou T, Xie R. Broadband near-infrared phosphor BaMgAl10O17:Cr^{3+} realized by crystallographic site engineering. *Chem Eng J* 2021;417:129224. DOI
22. Zeng H, Zhou T, Wang L, Xie R. Two-site occupation for exploring ultra-broadband near-infrared phosphor-double-perovskite La_2 $MgZrO_6$:Cr^{3+}. *Chem Mater* 2019;31:5245-53. DOI
23. Yan W, Liu F, Lu YY, Wang XJ, Yin M, Pan Z. Near infrared long-persistent phosphorescence in $La_3Ga_5GeO_{14}$:Cr^{3+} phosphor. *Opt Express* 2010;18:20215-21. DOI PubMed
24. Xu X, Shao Q, Yao L, Dong Y, Jiang J. Highly efficient and thermally stable Cr^{3+}-activated silicate phosphors for broadband near-infrared LED applications. *Chem Eng J* 2020;383:123108. DOI
25. Huang D, Zhu H, Deng Z, et al. A highly efficient and thermally stable broadband Cr^{3+}-activated double borate phosphor for near-infrared light-emitting diodes. *J Mater Chem C* 2021;9:164-72. DOI
26. Lin Q, Wang Q, Liao M, et al. Trivalent chromium ions doped fluorides with both broad emission bandwidth and excellent luminescence thermal stability. *ACS Appl Mater Interfaces* 2021;13:18274-82. DOI PubMed
27. Bindhu A, Naseemabeevi JI, Ganesanpotti S. Distortion and energy transfer assisted tunability in garnet phosphors. *Crit Rev Solid*

State Mater Sci 2022;47:621-64. DOI

28. Jia Z, Yuan C, Liu Y, et al. Strategies to approach high performance in Cr^{3+}-doped phosphors for high-power NIR-LED light sources. *Light Sci Appl* 2020;9:86. DOI PubMed PMC
29. Basore ET, Xiao W, Liu X, Wu J, Qiu J. Broadband near-infrared garnet phosphors with near-unity internal quantum efficiency. *Adv Optical Mater* 2020;8:2000296. DOI
30. Mao N, Liu S, Song Z, Yu Y, Liu Q. A broadband near-infrared phosphor $Ca_3Y_2Ge_3O_{12}:Cr^{3+}$ with garnet structure. *J Alloys Comp* 2021;863:158699. DOI
31. Meng X, Zhang X, Shi X, et al. Designing a super broadband near infrared material $Mg_3Y_2Ge_3O_{12}:Cr^{3+}$ using cation inversion for future light sources. *RSC Adv* 2020;10:19106-16. DOI PubMed PMC
32. Dumesso MU, Xiao W, Zheng G, et al. Efficient, stable, and ultra-broadband near-infrared garnet phosphors for miniaturized optical applications. *Adv Opt Mater* 2022;10:2200676. DOI
33. Zhou JY, Zhuo Y, Du F, et al. Efficient and tunable luminescence in Ga_2-xInx$O_3:Cr^{3+}$ for near-infrared imaging. *ACS Appl Mater Interf* 2021;13:31835-42. DOI PubMed
34. Xia Z, Ma C, Molokeev MS, Liu Q, Rickert K, Poeppelmeier KR. Chemical unit cosubstitution and tuning of photoluminescence in the Ca_2(Al(1-x)Mg(x))(Al(1-x)Si(1+x))O7:Eu(2+) phosphor. *J Am Chem Soc* 2015;137:12494-7. DOI PubMed
35. Shannon RD. Revised effective ionic radii and systematic studies of interatomic distances in halides and chalcogenides. *Acta Cryst A* 1976;32:751-67. DOI
36. Zhang L, Wang D, Hao Z, et al. Cr^{3+}-Doped broadband NIR garnet phosphor with enhanced luminescence and its application in NIR spectroscopy. *Adv Opt Mater* 2019;7:1900185. DOI
37. Tanabe Y, Sugano S. On the absorption spectra of complex ions II. *J Phys Soc Jpn* 1954:5;766-79. DOI
38. Mao M, Zhou T, Zeng H, et al. Broadband near-infrared (NIR) emission realized by the crystal-field engineering of $Y_{3-x}Ca_xAl_{5-x}Si_xO_{12}:Cr^{3+}$ (x = 0-2.0) garnet phosphors. *J Mater Chem C* 2020;8:1981-8. DOI
39. Zhang S, Qiu B, Li Z, et al. Achieving high quantum efficiency independent on luminescence center through sub-lattice cage engineering. *Chem Eng J* 2021;426:130734. DOI
40. Lian H, Li Y, Sharafudeen K, et al. Highly thermotolerant metal halide perovskite solids. *Adv Mater* 2020;32:e2002495. DOI PubMed
41. Malysa B, Meijerink A, Jüstel T. Temperature dependent Cr^{3+} photoluminescence in garnets of the type $X_3Sc_2Ga_3O_{12}$ (X = Lu, Y, Gd, La). *J Lumin* 2018;202:523-31. DOI
42. Kayanuma Y, Noba K. On the line shape of phonon side-band in photo-absorption of localized centers. *J Phys Soc Jpn* 1999;68:1061-1061. DOI
43. Tang F, Su Z, Ye H, et al. A set of manganese ion activated fluoride phosphors ($A_2BF_6Mn^{4+}$, A = K, Na, B = Si, Ge, Ti): synthesis below 0 °C and efficient room-temperature photoluminescence. *J Mater Chem C* 2016;4:9561-8. DOI
44. Kitzmann WR, Moll J, Heinze K. Spin-flip luminescence. *Photochem Photobiol Sci* 2022;21:1309-31. DOI PubMed
45. Macfarlane P, Han T, Henderson B, Kaminskii A. Cr^{3+} luminescence in calcium and strontium gallogermanate. *Opt Mater* 1994;3:15-24. DOI

Guo *et al. Microstructures* 2022;2:2022021
DOI: 10.20517/microstructures.2022.20

Microstructures

Review

Open Access

Check for updates

Design of super-elastic freestanding ferroelectric thin films guided by phase-field simulations

Changqing Guo[1,2], Houbing Huang[1,2]

[1]School of Materials Science and Engineering, Beijing Institute of Technology, Beijing 100081, China.
[2]Advanced Research Institute of Multidisciplinary Science, Beijing Institute of Technology, Beijing 100081, China.

Correspondence to: Prof. Houbing Huang, School of Materials Science and Engineering & Advanced Research Institute of Multidisciplinary Science, Beijing Institute of Technology, Beijing 100081, China. E-mail: hbhuang@bit.edu.cn

How to cite this article: Guo C, Huang H. Design of super-elastic freestanding ferroelectric thin films guided by phase-field simulations. *Microstructures* 2022;2:2022021. https://dx.doi.org/10.20517/microstructures.2022.20

Received: 16 Aug 2022 **First Decision:** 5 Sep 2022 **Revised:** 17 Sep 2022 **Accepted:** 30 Sep 2022 **Published:** 13 Oct 2022

Academic Editor: Shujun Zhang **Copy Editor:** Fangling Lan **Production Editor:** Fangling Lan

Abstract

Understanding the dynamic behavior of domain structures is critical to the design and application of super-elastic freestanding ferroelectric thin films. Phase-field simulations represent a powerful tool for observing, exploring and revealing the domain-switching behavior and phase transitions in ferroelectric materials at the mesoscopic scale. This review summarizes the recent theoretical progress regarding phase-field methods in freestanding ferroelectric thin films and novel buckling-induced wrinkled and helical structures. Furthermore, the strong coupling relationship between strain and ferroelectric polarization in super-elastic ferroelectric nanostructures is confirmed and discussed, resulting in new design strategies for the strain engineering of freestanding ferroelectric thin film systems. Finally, to further promote the innovative development and application of freestanding ferroelectric thin film systems, this review provides a summary and outlook on the theoretical modeling of freestanding ferroelectric thin films.

Keywords: Freestanding ferroelectric thin films, super-elastic, mechanical structure, topological domain structure, phase-field simulations

INTRODUCTION

The advancement of semiconductor materials and micro-/nanofabrication technologies has promoted the growth of the modern electronics industry. Various materials with excellent qualities which meet the needs

of the automated and intelligent manufacturing industries have been designed and prepared gradually. In recent decades, silicon-based complementary metal-oxide-semiconductor (CMOS)-centric design procedures have played a critical role in the modern electronics industry. However, the emergence of flexible electronic devices has presented new challenges for the traditional CMOS processing technique and new opportunities for the existing electronic manufacturing industry[1-3]. Flexible electronic materials can be applied to fabricate flexible displays[4-6], nanosensors[7-9], health monitors[10-12] and other electronic devices for intelligent processing and human-computer interactions[13]. For example, flexible electronic materials can integrate cutting-edge technologies, including intelligent signal processing, real-time information sensing and nanogenerators, to improve the intelligence level of biocompatible electronics. As a result, they play an increasingly critical role in the intelligent monitoring of human health and biomedical applications, which will significantly change the future of healthcare and the relationship between patients and electronics. Furthermore, with the rise and combination of artificial intelligence and the Internet of Things (AI and IoT, i.e., AIoT), these electronic devices have an increasingly wide range of applications.

However, most traditional inorganic materials with excellent electronic properties show poor stability in complex stress environments, thereby severely limiting their application prospects in flexible electronic devices. Therefore, finding and preparing basic materials with excellent electronic and flexible properties is one of the keys to developing the flexible electronics industry. Generally, two complementary approaches can be applied to obtain electronic materials with superior mechanical and electrical properties. The first is the design and innovation of flexible materials by developing novel materials, including polymers[14,15], hydrogels[16,17], liquid metals[18,19] and freestanding films[20,21]. The second is structural optimization design by designing traditional high-performance electronic materials into appropriate mechanical structures[22,23], including wrinkled[24,25], origami[26,27], kirigami[28,29] and textile[30,31] structures.

Ferroelectric perovskite oxides are indispensable materials in the modern electronics industry because of their abundance of excellent physical properties, extensive research value and long-term practical application prospects. High-performance ferroelectric oxides are critical components in the current electronics industry because they have outstanding electrical properties, including ferroelectricity, piezoelectricity, pyroelectricity and dielectricity. They are widely applied in high-efficiency memories[32-35], microsensors[36,37], high-frequency filters[38,39], energy harvesting systems[40,41], high-energy-density capacitors[42-45], ultrasonic medical treatment[46,47] and other related devices[48-51], and are also expected to be applied in the field of high-temperature superconductivity[52,53]. However, perovskite ferroelectrics are generally considered to be brittle and unbendable[54,55]. Therefore, if they can be transformed into flexible structures through the above two approaches, it will significantly accelerate the growth of the flexible electronics industry and occupy increasingly widespread applications. In addition, organic ferroelectric polymer materials[56-60], such as poly(vinylidene fluoride) and its copolymers, have excellent properties and can achieve sizeable mechanical deformation, such as stretching, bending and twisting, without being damaged. Therefore, for the design and processing of flexible electronic materials, ferroelectric materials with flexibility and super-elasticity have received extensive attention due to their excellent mechanical and electrical properties.

This review mainly focuses on super-elastic freestanding ferroelectric thin films. First, current super-elastic freestanding ferroelectric films and their experimental characterization results are summarized. Subsequently, the origin of the super-elasticity of freestanding ferroelectric thin films is revealed and explained on the basis of phase-field simulations. The designed mechanical structures based on super-elastic ferroelectric thin films, such as two-dimensional (2D) wrinkles and three-dimensional (3D) nanosprings, are then introduced [Figure 1]. Finally, the outlook and prospects for super-elastic flexible freestanding

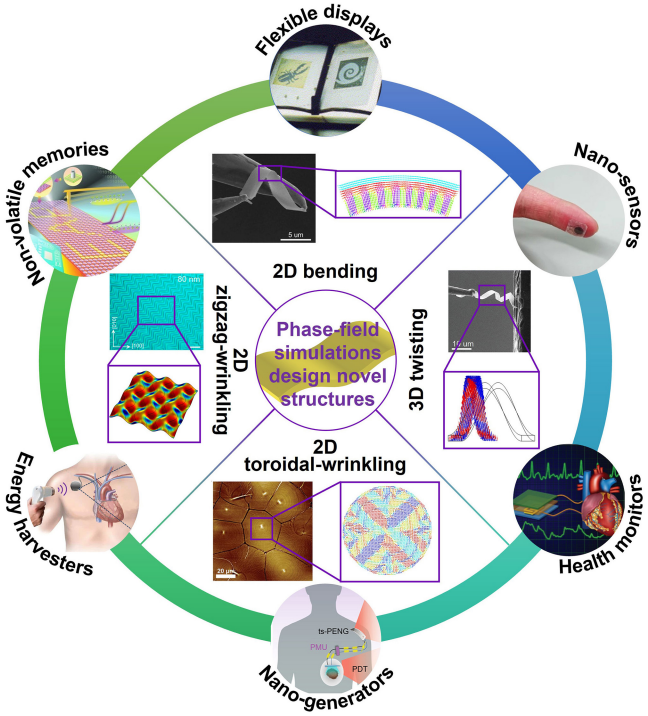

Figure 1. Novel mechanical structures and applications of super-elastic/flexible freestanding ferroelectric thin films. Novel mechanical structures include 2D bending (Left : reprinted with permission[61]. Copyright 2019, The American Association for the Advancement of Science. Right: reprinted with permission[62]. Copyright 2020, AIP Publishing), 2D zigzag-wrinkling (Top: reprinted with permission[63]. Copyright 2020, Wiley-VCH. Bottom: reprinted with permission[64]. Copyright 2022, American Chemical Society), 2D toroidal-wrinkling (reprinted with permission[65]. Copyright 2021, The American Association for the Advancement of Science), and 3D twisting (reprinted with permission[66]. Copyright 2022, Wiley-VCH) structures. Flexible applications include non-volatile memories (reprinted with permission[67]. Copyright 2013, Wiley-VCH), flexible displays (reprinted with permission[68]. Copyright 2004, Elsevier), nano-sensors (reprinted with permission[69]. 2018, CC BY license), health monitors (reprinted with permission[70]. Copyright 2016, Wiley-VCH), nano-generators (reprinted with permission[71]. Copyright 2020, American Chemical Society), and energy harvesters (reprinted with permission[72]. 2016, CC BY license).

ferroelectric thin films are presented.

SUPER-ELASTIC FREESTANDING FERROELECTRIC FILMS

Preparation of flexible ferroelectric thin films

Due to the clamping effect of the rigid substrates during the traditional process of preparing ferroelectric thin films, they often show far poorer electrical performance, in terms of piezoelectric constant, switching speed and switching voltage[73-76], than those of freestanding materials. With the rapid development of new fabrication techniques for thin films[77], high-quality flexible freestanding ferroelectric thin films with excellent mechanical elastic and electrical properties[78,79] can be fabricated. Since many excellent reviews[21,80-83] have discussed the preparation of flexible freestanding ferroelectric films, we only briefly summarize the methods for obtaining them here.

Direct growth. Ferroelectric thin films can be directly grown on flexible substrates, including metals (such as foils), organic polymers (such as polyimide (PI)) and 2D layered materials (such as mica and graphene). Metal foils have low brittleness, excellent electrical conductivity and outstanding thermal stability as flexible substrates. Due to the unfavorable thermal expansion mismatch and ion diffusion between the ferroelectric thin film and the metal foil, a buffer layer is usually grown on the surface of the substrate to solve these problems. For instance, Won *et al.* used $LaNiO_3$, which has closely matched lattice parameters (~0.38 nm)

with most perovskite ferroelectric materials, as a conductive buffer layer and the prepared $Pb(Zr,Ti)O_3$ films exhibited superior ferroelectricity and piezoelectricity than those on conventional $Pt/Ti/SiO_2/Si$ substrates[84]. Although PI substrates have better mechanical ductility and flexibility, the temperature they can withstand (< 400 °C) cannot reach the crystallization temperature of ferroelectric oxides (> 600 °C). Bretos *et al.* proposed a series of solution-based approaches to realize the low-temperature crystallization of ferroelectric thin films, such as $BiFeO_3$ and $Pb(Zr,Ti)O_3$[85-89]. In addition to the aforementioned direct growth on flexible substrates, mechanical exfoliation along heterointerfaces after the deposition of ferroelectric thin films onto 2D layered materials has also been developed. Through van der Waals epitaxy, weak bonds are formed between the thin film and the 2D layered substrate, providing an opportunity for mechanical exfoliation to obtain freestanding ferroelectric thin films with minimal internal stress. Mica[90-92] and graphene[93,94] are promising 2D layered materials as flexible substrates with atomic-level surface roughness, good stability and mechanical flexibility. High-quality flexible ferroelectric films with good mechanical integrity can be grown on mica and graphene substrates by van der Waals epitaxy, demonstrating their potential for next-generation electronics.

Laser lift-off process. The laser lift-off method was initially proposed and developed for transferring epitaxial GaN films from substrates[95,96] and was later utilized to prepare and obtain flexible freestanding ferroelectric oxide films. The specific process is to first deposit a ferroelectric oxide film (such as via a sol-gel method) on a wide band gap substrate (such as sapphire). A laser then irradiates the sample from the back of the substrate to partially vaporize the interface between the ferroelectric film and the substrate. Finally, a freestanding ferroelectric oxide film is obtained. However, this stripping method ablates the ferroelectric thin film, forming a thermally damaged layer at the interface of the thin film, so it is necessary to introduce a sacrificial layer[97,98] and further anneal to recover the surface structure[99].

Wet etching. Obtaining freestanding ferroelectric thin films by wet etching is a promising approach with significant advantages. According to the parts to be etched, wet etching can be divided into wet etching of the substrate, wet etching of the interface layer between the thin film and substrate and wet etching of the sacrificial layer, with the latter being the more cost-effective method[99]. Single-crystal ferroelectric thin films have been grown on sacrificial buffer layer (e.g., $La_{0.7}Sr_{0.3}MnO_3$[100,101], $Sr_3Al_2O_6$[102-106] and BaO[107])-coated $SrTiO_3$ (STO) substrates. Subsequently, the sacrificial buffer layer is dissolved by selective etching to release the freestanding ferroelectric oxide film. Finally, the freestanding thin films can be transferred to flexible substrates, such as polyethylene terephthalate[75,108] or polydimethylsiloxane (PDMS)[61,105,109-111]. They can also be transferred to silicon (Si) substrates and combined with Si-based electronics. For example, Han *et al.* selected water-soluble $Sr_3Al_2O_6$ as the sacrificial layer to grow a series of $(PbTiO_3)_m/(SrTiO_3)_n$ bilayers on STO substrates. After the $Sr_3Al_2O_6$ sacrificial layer was dissolved, the bilayer films were laminated on a platinized Si (001) substrate[112]. Exotic skyrmion-like polar nanodomains are observed in bilayer films, which provide a new strategy for integration into Si-based high-density storage technologies.

Super-elastic behavior of freestanding single-crystal ferroelectric thin films

Ferroelectric oxides are generally considered to be brittle and non-bendable because of their grain boundaries and the small ductility of ionic or covalent bonds within the crystal. In addition, the low fracture toughness (in the order of 1 $MPa{\cdot}m^{1/2}$)[55] means that ferroelectric oxides are prone to fracture. Nevertheless, the high-quality freestanding single-crystal ferroelectric thin films obtained by the above freestanding methods have attractive mechanical flexibility and super-elasticity. Dong *et al.* fabricated freestanding single-crystal $BaTiO_3$ (BTO)[61] and $BiFeO_3$ (BFO)[110] ferroelectric thin films by pulsed-laser deposition (PLD) when using $Sr_3Al_2O_6$ as a sacrificial layer that was dissolved in water. As shown in Figure 2A and B, the fabricated BTO films could undergo a ~180° folding without any cracks in in-situ scanning electron microscopy (SEM) bending tests and also recover to their original shape after removing the bending load.

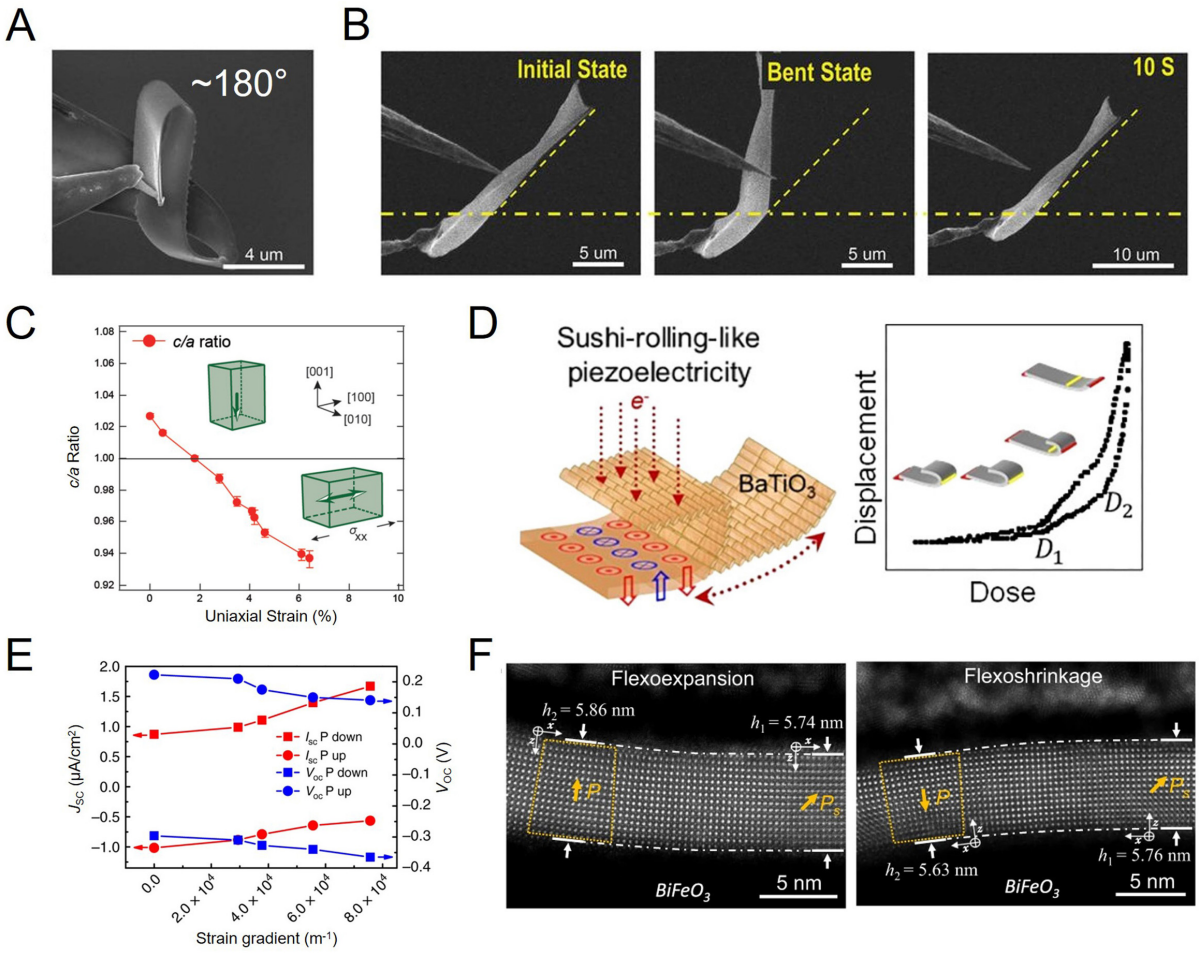

Figure 2. (A) In situ SEM image of the BTO film folded to about 180°. (B) SEM images of bending and recovery process of a BTO film. (C) The *c/a* ratio of freestanding PTO films as a function of uniaxial strain. The inset is schematics of as-grown and stretched polarization state. (D) Electromechanical coupling responses of freestanding BTO films folded and unfolded under an electron beam-induced field. (E) Open circuit voltage (V_{oc}) and short circuit current density (J_{sc}) of freestanding BFO device as a function of strain gradient. (F) The bending-expansion and bending-shrinkage effects were observed in upward and downward bent BFO films. Panels A and B reprinted with permission[61]. Copyright 2019, The American Association for the Advancement of Science. Panel C reprinted with permission[106]. Copyright 2020, Wiley-VCH. Panel D reprinted with permission[113]. Copyright 2020, American Chemical Society. Panel E reprinted with permission[109], 2020, CC BY license. Panel F reprinted with permission[114], 2022, CC BY license.

This behavior demonstrates their super-elasticity and flexibility. Similarly, the BFO film could withstand cyclic folding tests of up to 180° and the largest bending strain was observed to reach 5.42% during the bending process. Furthermore, freestanding flexible multiferroic $BiMnO_3$ films were synthesized by Jin *et al.*, which could maintain mechanical integrity under nearly 180° folding[111].

Freestanding thin films, in contrast to epitaxial thin films, are free from the clamp of the substrate and therefore provide ideal and unique flexible platforms for continuously controllable strain engineering. For example, Han *et al.* applied a continuous uniaxial tensile strain as high as 6.4% to freestanding $PbTiO_3$ (PTO) films, far exceeding the realizable value for epitaxial PTO films [Figure 2C][106]. This demonstrates the efficient and meaningful strain tunability of freestanding ferroelectric films, which deserves further exploration and design. Flexible freestanding oxides also provide a new direction for exploring outstanding performance, including piezoelectricity and flexoelectricity. By PLD, Elangovan *et al.* fabricated 30-nm-thick flexible freestanding piezoelectric BTO thin films with good electromechanical-coupling

properties[113]. As shown in Figure 2D, under an external electric field, the thin film could fold gradually and continuously by 180° and the fold-unfold cycles were reversible. The contribution of the flexoelectric effect caused by the strain gradient induced by bending in flexible films is considerable. Guo *et al.* demonstrated the tunable photovoltaic effect in freestanding single-crystal BFO films and obtained multilevel photoconductance in BFO by altering the bending radius of the flexible device [Figure 2E][109]. As shown in Figure 2F, Cai *et al.* observed a giant flexoelectric response at strain gradients of up to ~3.5 × 10^7 m^{-1} in a wrinkled structure based on high-quality flexible freestanding BFO perovskite oxides[105,114]. Furthermore, the unusual bending expansion and shrinkage observed in bent freestanding BFO are also never seen in crystalline materials. Corresponding theoretical models show that these novel phenomena are attributed to the combined action of flexoelectricity and piezoelectricity. These experimental observations and theoretical models may provide a new path toward the strain and strain-gradient engineering of super-elastic freestanding ferroelectric thin films.

PHASE-FIELD METHOD OF FERROELECTRICS

The mechanical, electrical, optical, magnetic and other macroscopic physical properties of a material are not only related to its chemical composition but also largely depend on the characteristics of its internal microstructure. Such microstructures can be phase structures composed of crystalline structures, grains with different orientations, ferroelectric domains and dislocations, which are usually at the mesoscopic scale, ranging from nanometers to micrometers[115]. In material processing and service, external stimuli may cause the microstructure to move away from equilibrium. Furthermore, the corresponding theoretical description requires a combination of non-equilibrium thermodynamics and kinetic theories. Thermodynamic theory and kinetic principles determine the evolution direction and path of the microstructure, respectively. Due to the complexity and nonlinearity of microstructural evolution, we usually use numerical simulation methods to predict the evolution process. Compared to traditional modeling methods involving the explicit tracking of interface locations, the phase-field method has become one of the most powerful methods for simulating the evolution process of various microstructures. The phase-field method is based on the Landau theory of phase transitions, which holds that one of the standard features of a phase transition is a change in the symmetry of a system. Changes in symmetry imply changes in the degree of order, which can be measured by the order parameter (as a space function). According to the selection of order parameters, ferroelectrics are classified as proper or improper. For BTO, PTO and other proper ferroelectrics, the selected order parameter is the ferroelectric polarization P that can explain the symmetry change in the phase transition. However, for improper ferroelectrics, such as hexagonal manganites h-$REMnO_3$ (RE = rare earth), the primary order parameter is the amplitude Q and phase Φ characterizing the structural trimerization and the secondary order parameter is the polarization P induced by the trimerization[116,117].

Theoretical fundamentals of phase-field method

The phase-field method with diffusive interfaces considers the non-local energy of the polarization gradient, which is different from the homogeneous assumption in thermodynamic models. By solving the phase-field equations, the order parameters in the space and time distribution can be calculated, the spatially continuous but inhomogeneous polarization distribution in the ferroelectric at different times can be determined and the evolution process of the microstructure can be obtained. The evolution process is a direct consequence of the minimization of the total free energy of the entire system, where ferroelectric polarization switching and phase transitions can be simulated by solving the time-dependent Ginzburg-Landau equation[118-122]:

$$\frac{\partial P_i(\boldsymbol{r},t)}{\partial t} = -L\frac{\delta F}{\delta P_i(\boldsymbol{r},t)}, i = x, y, z, \tag{1}$$

where $P_i(\boldsymbol{r},t)$ is the spontaneous polarization, $\boldsymbol{r}$ is the spatial coordinate, t is the evolution time, L is the kinetic coefficient that is related to the domain evolution and F is the total free energy that includes the contributions from the Landau, gradient, elastic, electric and flexoelectric coupling energies:

$$F = \iiint_V [f_{Land}(P_i) + f_{grad}(P_{i,j}) + f_{elec}(P_i, E_i) + f_{elas}(P_i, \varepsilon_{ij}) + f_{flexo}(P_i, \varepsilon_{kl}, P_{i,j}, \varepsilon_{kl,j})]dV. \tag{2}$$

The Landau energy density f_{Land} and the gradient energy density f_{grad} are given by:

$$f_{Land} = \alpha_{ij}P_iP_j + \alpha_{ijkl}P_iP_jP_kP_l + \alpha_{ijklmn}P_iP_jP_kP_lP_mP_n, \tag{3}$$

$$f_{grad} = \frac{1}{2}G_{ijkl}P_{i,j}P_{k,l}, \tag{4}$$

where α_{ij}, α_{ijkl} and α_{ijklmn} are the Landau coefficients, G_{ijkl} is the gradient energy coefficient and $P_{i,j} = \partial P_i/\partial x_j$.

The electric energy density f_{elec} is expressed as:

$$f_{elec} = -E_i(P_i + \frac{1}{2}\varepsilon_0\kappa_{ij}E_j), \tag{5}$$

where E_i is the electric field component, ε_0 is the vacuum permittivity and κ_{ij} is the dielectric constant. The electrical quantities should satisfy the electrostatic equilibrium (Poisson's) equation:

$$-\nabla^2\varphi = \frac{\rho - \nabla P_i}{\varepsilon_0\kappa_{ij}}, \tag{6}$$

where φ is the electric potential and ρ represents the total space charges. The electric field is related to the potential through $E_i = -\varphi_{,i}$.

The elastic energy density f_{elas} and the flexoelectric coupling energy density f_{flexo} can be written as:

$$f_{elas} = \frac{1}{2}C_{ijkl}e_{ij}e_{kl} = \frac{1}{2}C_{ijkl}(\varepsilon_{ij} - \varepsilon_{ij}^0)(\varepsilon_{kl} - \varepsilon_{kl}^0), \tag{7}$$

$$f_{flexo} = -\frac{1}{2}f_{ijkl}(\varepsilon_{ij,l}P_k - \varepsilon_{ij}P_{k,l}), \tag{8}$$

where C_{ijkl} is the elastic stiffness tensor, e_{ij} is the elastic strain and ε_{ij} and ε_{ij}^0 are the total local strain and eigenstrain, respectively. Moreover, $\varepsilon_{ij}^0 = Q_{ijkl}P_kP_l$, where Q_{ijkl} represents the electrostrictive coefficients. f_{ijkl} is the flexoelectricity tensor and there are three independent flexoelectric coupling coefficients for a material of cubic point group, namely, the longitudinal coupling coefficient f_{1111}, the transversal coupling coefficient f_{1122} and the shear coupling coefficient f_{1212}.

The mechanical quantities are satisfied by solving the mechanical equilibrium equation:

$$\sigma_{ji,j} + b_i = 0, \tag{9}$$

where σ_{ij} is the stress tensor and b_i is the external force per unit volume.

Phase-field model of freestanding ferroelectric thin films

The phase-field model of a freestanding ferroelectric thin film differs from that of an epitaxial ferroelectric thin film with a substrate. As shown in Figure 3A and B, the lattice points of traditional epitaxial ferroelectric thin film models are subjected to compressive (or tensile) misfit strains induced by the substrate. The lattice points in the new phase-field model of the freestanding ferroelectric thin film have deformability characteristics, which can change the volume and shape following the bending deformation of the thin film.

The deformation of freestanding ferroelectric films can be set by applying displacement or stress (strain) boundary conditions. For instance, Guo *et al.* achieved the bending deformation of a freestanding film by applying displacement boundary conditions, explicitly adjusting the rotational inclination of the left and right end of the film along the neutral surface[62]. Moreover, Peng *et al.* stabilized the film to a bending state by applying stress (strain) boundary conditions, explicitly introducing a bending strain state that exhibits a gradient distribution along the film thickness[110,123,124]. In addition, the top and bottom layers of the film are set as stress-free boundaries to satisfy the freestanding boundary conditions. Therefore, as shown in Figure 3C, for the phase-field method of freestanding ferroelectric thin films, by using the well-established phase-field model of deformable lattices, considering the freestanding boundary conditions and the complex strain (and strain gradient) states caused by the deformation of novel mechanical structures, the nanodomains corresponding to the freestanding ferroelectric structure can be obtained. The mechano-electric coupling relationship and electrical properties (including piezoelectricity and electrocaloric performance) of the freestanding ferroelectric system can then be explored.

MODEL-GUIDED UNDERSTANDING OF SUPER-ELASTICITY IN FREESTANDING FERROELECTRIC THIN FILMS

Freestanding thin films demonstrate the advantages of tunable strain states compared with epitaxial growth on lattice-mismatched substrates. The source of the superior super-elasticity of freestanding films needs to be further explored because it is crucial for their further application in flexible electronics. The super-elasticity of freestanding ferroelectric membranes may originate from the mesoscale ferroelectric domain evolution in the presence of the external deformation. However, the direct observation of the domain structure evolution of nanoscale freestanding films during continuous deformation is challenging by current experimental methods.

The phase-field method can simulate the dynamic evolution of freestanding ferroelectric films during mechanical deformation under external loads and the ferroelectric phase transition behavior under various strains and temperatures. Unlike the domain structure of ferroelectric films under a single strain in previous studies, more complex nanodomains appear due to the coexistence of tensile and compressive strains in bent freestanding films. For instance, Guo *et al.* and Peng *et al.* performed phase-field simulations on the bending deformation process of freestanding ferroelectric films to reveal the theoretical origin of the super-elasticity of freestanding ferroelectric films from the perspective of domain evolution[62,123]. During the continuous bending process of a freestanding BTO film, the mixed tensile and compressive stress generated

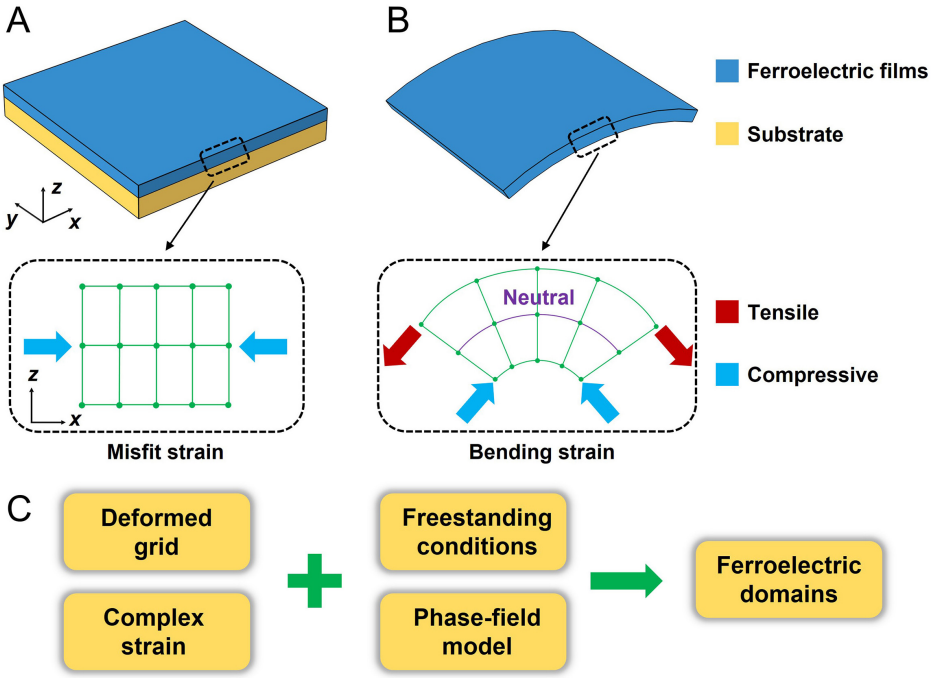

Figure 3. (A) Phase-field model of the epitaxial ferroelectric thin film with a substrate. The dashed box is a schematic of the model lattice under compressive misfit strain. (B) Phase-field model of the bent freestanding ferroelectric thin film. The dashed box is a schematic of the deformable model lattice under bending strain, and the purple line represents the neutral layer of the model. (C) The structural schematic of the phase-field method for freestanding ferroelectric thin films.

by the bending [Figure 4A] caused the electric dipole to rotate continuously in the transition region, thereby connecting the *a* and *c* domains to form "vortex-like" domain structures [Figure 4B]. The formation of "vortex-like" domains essentially eliminates the sharp stress caused by lattice mismatch, allowing the freestanding film to maintain mechanical integrity during the bending process. The continuous rotation of the electric dipole can be explained by the phenomenological Landau theory[61]. As seen from Figure 4C, four minima in the energy landscape exist in a bulk stress-free state of BTO, corresponding to two *a* domains and two *c* domains. When in the bending state, the energy barrier between the *a* and *c* domains decreases, indicating that the polarization transition between the *a* and *c* domains becomes easier. The appearance of "vortex-like" domains has apparent size effects and the *a*/*c* phase with a vortex-like structure emerges when the film thickness reaches 12 nm [Figure 4D]. This may indicate that the super-elasticity of freestanding ferroelectric films has a specific relationship with the film thickness.

From the perspective of phase-field energy minimization, the generation of a local ferroelectric vortex and the ferroelectric polarization rotation can effectively promote the reduction in elastic energy and modulate the mechanical stress on the freestanding ferroelectric film during bending, which contributes to the accommodation of the large deformation and super-elasticity. As shown in Figure 4E, Peng *et al.* investigated the dynamic domain evolution process of bent freestanding BFO films, with an exotic ferroelectric vortex generated by local ferroelastic switching when the bending angle was higher than the critical value (e.g., 17.19° for a thickness of 80 nm)[123]. By comparing the dynamic evolution of different energy densities during the phase-field simulation [Figure 4F], the intrinsic energy barrier ($\Delta f_{barrier}$ = 1076.19 kJ/m^3) is overcome by reducing the elastic energy ($\Delta f_{elastic}$ =1157.65 kJ/m^3) when vortex domains are generated, which indicates that the minimization of elastic energy drives the generation of the vortex. As reviewed above from the perspective of domain structure evolution, the excellent mechanical

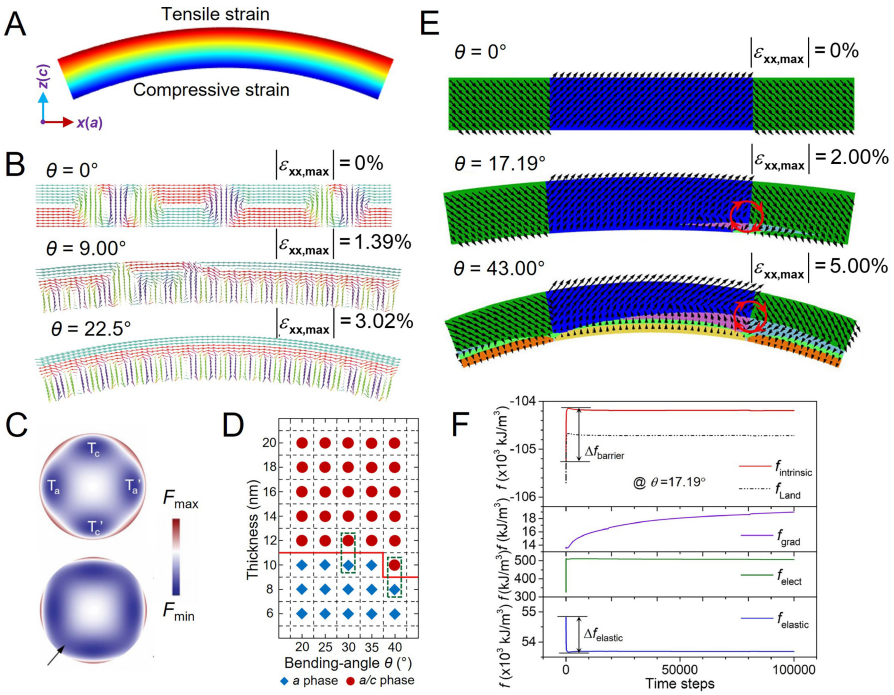

Figure 4. (A) Strain distribution of *n*-shape bent freestanding films. (B) Domain structures and surface strain of freestanding BTO thin film at different bending angles. (C) Schematic illustration of free energy landscape of bulk BTO (top) and freestanding thin films upon bending (bottom). (D) Size effect on domain patterns of BTO thin film under bending. (E) Dynamic evolution of ferroelectric domains in freestanding BFO thin films during bending. (F) Dynamic evolution of volume average energy density of freestanding BFO thin films under θ = 17.19° with time step. Panels A, B and D reprinted with permission. Copyright 2020, AIP Publishing[62]. Panel C reprinted with permission. Copyright 2019, American Association for the Advancement of Science[61]. Panels E and F reprinted with permission. Copyright 2021, Elsevier[123].

elasticity of freestanding ferroelectric films can be attributed to the strong coupling effects between the bending strain state and electric dipoles, including the continuous rotation of polarization, the emergence of polar vortex domains and ferroelectric phase transitions.

FUNCTIONAL MECHANICAL STRUCTURES BASED ON SUPER-ELASTIC FERROELECTRIC THIN FILMS

Freestanding ferroelectric thin films are ideal for studying the distortion of crystal structures and future applications of ferroelectric materials. Taking flexible carriers for memory logic devices as an example, Chen *et al.* systematically investigated the stability of 180° cylindrical domains in bent freestanding ferroelectric nanofilms and explored the possibility of mechanical erasure of bit information ("0" and "1")[125]. Ferroelectrics are potential candidates for data storage due to their switchable spontaneous polarization. Figure 5A shows a freestanding PTO thin film divided into rectangular memory units, where the bit information "1" is represented by a cylindrical domain with downward polarization of radius *r*. From the phase diagram in Figure 5B, the bending deformation can effectively control the stability of the cylindrical domain and regulate the erasing of bit information. By changing the strain state of freestanding ferroelectric thin films, cylindrical domains can be erased, thereby providing a new theoretical idea for flexible memory devices. In addition to bending structures based on super-elastic freestanding ferroelectric films, other mechanical structures, such as 2D wrinkled and 3D nanospring structures, are also paving the way for novel flexible electronics.

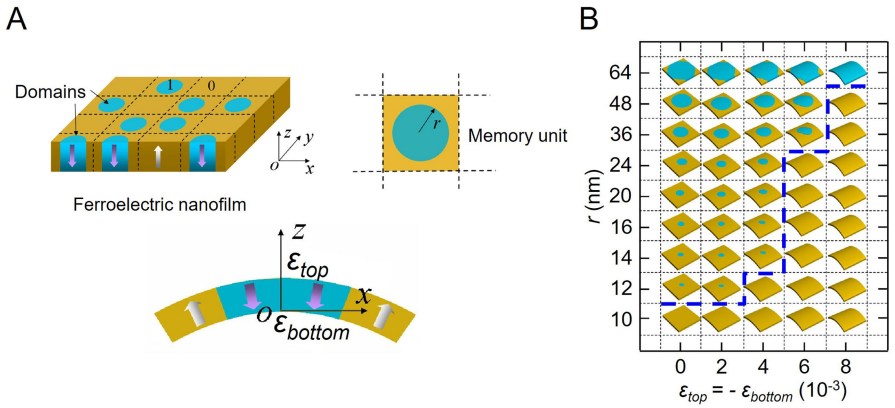

Figure 5. (A) Schematic illustration of a ferroelectric nanofilm with rectangular memory units (upper left), a single basic memory unit (upper right), and a bent single memory unit (bottom). (B) Phase diagram of the domain pattern in memory units under bending. All panels reprinted with permission[125], 2014, CC BY license.

2D wrinkled structure of freestanding ferroelectric thin films

The buckling instability mode, which leads to out-of-plane deformation, is prone to occur in thin film structures under certain environmental stimuli (e.g., mechanical forces[126-130], temperature[131], van der Waals interactions[132] and localized diffusion of the solvent[133,134]). For example, when the film is subjected to in-plane compressive stress, it is in an unstable state with high energy. As a result, the film and substrate deform to release compressive stress, thereby reducing the energy of the system. Moreover, because the film thickness h is small, its bending rigidity $D = E_f h^3/12$ is minimal compared to Young's modulus E_f. Films generally deform via out-of-plane wrinkling to release internal compressive stress by generating bending energy. For the simplest sinusoidal wrinkling mode $w(x,y) = A\cos(kx)$, both the wavelength and amplitude are related to the mechanical quantities of the film-substrate system[135-139]:

$$\begin{aligned} \lambda &= 2\pi h\left(\frac{\bar{E}_f}{3\bar{E}_s}\right)^{\frac{1}{3}}, \\ \varepsilon_c &= \frac{1}{4}\left(\frac{3\bar{E}_s}{\bar{E}_f}\right)^{\frac{2}{3}}, \\ A &= h\left(\frac{\varepsilon}{\varepsilon_c}-1\right)^{\frac{1}{2}}, \\ \bar{E} &= \frac{E}{1-\nu^2}, \end{aligned} \tag{10}$$

where E_f and E_s are Young's modulus of the film and substrate, respectively, ν is the Poisson's ratio and λ and A are the wavelength and amplitude of the wrinkle, respectively [Figure 6A].

The buckling instability of wrinkles is a fascinating nonlinear mechanical model and is very effective in understanding their formation mechanism from an energy perspective. For a film bonded to a compliant substrate, Huang *et al.* obtained the wavelength and amplitude of the wrinkles for substrates with different moduli and thicknesses by minimizing the energy[137]. As shown in Figure 6B, when the strain of the film $\varepsilon_{\text{film}}$ is less than ε_c, the system minimizes at the state $A = 0$, and when the strain of the film $\varepsilon_{\text{film}}$ exceeds ε_c, the system wrinkles to an equilibrium amplitude A_{eq}. The occurrence of buckling modes may lead to structural and functional failure of the membranes, potentially limiting the performance of materials and is often considered to be avoided. In contrast, stress-driven buckling instability can self-assemble ordered surface

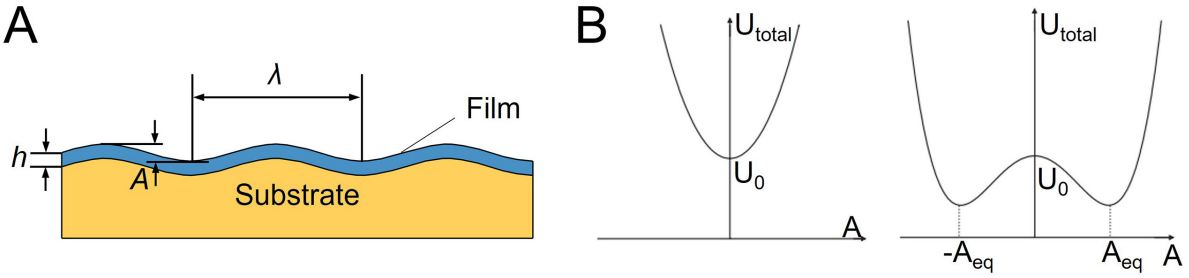

Figure 6. (A) A thin film on a compliant substrate undergoes surface wrinkling. (B) Schematic of the total energy of the thin film system as a function of the wrinkle amplitude *A* at small (left) and large (right) film strains (reprinted with permission[137]. Copyright 2005, Elsevier).

topographies, including sinusoidal, zigzag, labyrinthine, triangular and checkerboard patterns. The physical properties of wrinkles show broad application prospects in the design of flexible electronic devices, the assembly of 3D complex microstructures[140], the morphological control of innovative optoelectronics and integrated systems[141-143], the measurement of mechanical properties of materials[144,145] and even medical assistance in diagnosis and treatment[146].

The formation of various wrinkled structures has been reported in thin film systems such as metals[126], graphene[132], organics[130,131,133,134], gels[147], biological tissues[148] and more recently in freestanding ferroelectric thin film systems. As shown in Figure 7A, Dong *et al.* successfully fabricated periodic wrinkle-patterned BTO/PDMS membranes based on an as-prepared super-elastic single-crystal freestanding BTO film[63,64]. Moreover, finely controlled wrinkle patterns, such as sinusoidal, zigzag and labyrinthine patterns, were obtained by changing the anisotropy and magnitude of the applied stress or adjusting the interfacial adhesion conditions. It is noteworthy that the thickness of the super-elastic BTO film significantly affected the period of the wrinkle pattern. The thicker the BTO film, the larger the wavelength, which also conforms to Equation (10), i.e., the wavelength and period of the wrinkle pattern are proportional to the thickness of the film.

Due to the peculiar morphology of wrinkled ferroelectric films, the strain state is different from the interfacial mismatch strain of conventional epitaxial films. Therefore, a unique ferroelectric domain structure distribution can be generated by applying external loads. For example, the strain field is introduced by a scanning probe, which is quite different from applying out-of-plane strain directly to the epitaxial film, as shown in Figure 7C. Zhou *et al.* found a periodic "braided" in-plane domain superstructure and opposite out-of-plane domains between peaks and valleys through the modulation of scanning probe microscopy (SPM) tip-induced loading forces, as seen in Figure 7B[64]. This unique domain depends on the strain state induced by the zigzag wrinkle morphology and the loading of the SPM tip. Due to the periodic "braided-like" strain state, the polarization is deflected to the direction parallel (perpendicular) to the tensile strain (compressive strain) ε_{xx}, resulting in the formation of the ferroelectric nanodomain structure, as shown in Figure 7D. In addition, some novel wrinkle structures also exist in flexible ferroelectric polymer systems. As shown in Figure 7E, Guo *et al.* found a periodic toroidal "target-like" wrinkle morphology in a flexible ferroelectric polymer poly(vinylidene fluoride-ran-trifluoroethylene) [P(VDF-TrFE)], as well as a peculiar toroidal topological texture using in-plane piezoresponse force microscopy (IP-PFM) measurements[65]. The distribution of the toroidal domain structure [Figure 7G] is caused by the strain state induced by the "target-like" wrinkle morphology under external tensile strain, which is a periodically alternating tensile and compressive strain [Figure 7F]. According to this calculation, the electric toroidal moment[149] G_z is much larger than G_x and G_y, indicating the existence of in-plane toroidal order

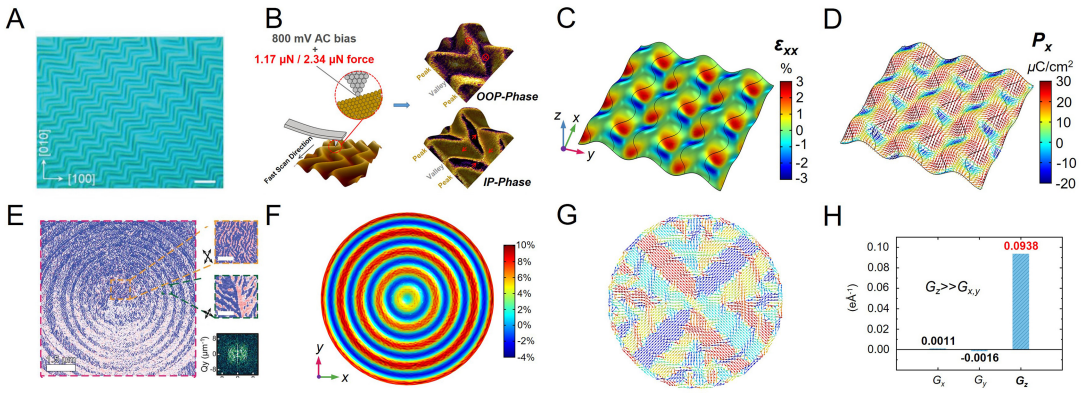

Figure 7. (A) Optical microscopy images of wrinkled BTO. The scale bar is 20 μm. (B) Piezoresponse force microscopy (PFM) phase color images of zigzag-wrinkled BTO under scanning force induced by the SPM tip. (C) Distribution of corresponding strain component ε_{xx} of zigzag-wrinkled BTO by the SPM tip from phase-field simulations considering the flexoelectric effect. (D) Distribution of "braided-like" polarization of zigzag-wrinkled BTO by the SPM tip. The color bar represents the polarization component P_x. (E) IP-PFM phase image showing the toroidal polar topology of wrinkled P(VDF-TrFE) film. (F and G) The in-plane strain and domain structure of the wrinkled P(VDF-TrFE) under an applied tensile strain of 7.3% from phase-field simulations, respectively. (H) The electric toroidal moments corresponding to the domain structure in (G) illustrate the presence of in-plane topological domains. Panel A reprinted with permission[63]. Copyright 2020, Wiley-VCH. Panels B-D reprinted with permission[64]. Copyright 2022, American Chemical Society. Panels E-H reprinted with permission[65]. Copyright 2021, The American Association for the Advancement of Science.

[Figure 7H]. Therefore, the morphology of freestanding ferroelectric wrinkled films can be developed as a degree of freedom for strain tuning the domains and physical properties of flexible ferroelectric systems.

3D nanospring structure of freestanding ferroelectric thin films

Ferroelectric materials display a range of individual polar topological states, including flux-closure domains[150,151], vortices[152-155], skyrmion bubbles[156,112,157], merons[158], center domains[159] and sixfold vortex networks[160], as a result of geometrical constraints between structural shape and material interface at the micro/nanoscale. The competition and coupling of elastic, electrostatic and gradient energies can lead to the induction of novel polar topologies that are not stable in conventional bulk ferroelectrics under the combined influence of a sharply increased depolarization field caused by size, noticeable interface and boundary constraint effects. With the demand for the miniaturization and multi-functionalization of functional ferroelectric devices, an increasing number of nanostructures with novel topological ferroelectric domains can be realized through top-down and bottom-up nanofabrication techniques. For example, Shimada *et al.* designed and studied 2D PTO nanostructures (including honeycomb, kagome and star shapes) by establishing a phase-field model based on a 2D Archimedes lattice[161]. Furthermore, the polarization was gradually rotated at the junctions of different repeating units in these nano-metamaterials to form a continuous flow pattern.

Among the unique nanostructures designed and produced, the emergence of nanosprings has received considerable attention. Nanosprings can achieve enormous amounts of mechanical deformation while maintaining mechanical integrity and are also an essential set of geometries among chiral structures. This 3D helical structure can have broad potential applications in electromechanical devices such as nanoactuators, nanosensors and nanomotors. In contrast to the wrinkles reviewed in the previous section, mechanical buckling-induced self-assembled nanosprings can be obtained by removing the mechanical constraints in the out-of-plane direction and introducing a bilayer structure. Changes in these mechanical conditions enable the system not to be confined to 2D in-plane extended wrinkle deformation but to 3D deformation modes, such as rolling and twisting, leading to the formation of 3D rolled-up structures. This

unique buckling behavior has been utilized in various studies to obtain 3D structures from 2D bilayers, coupled with the characteristic that nanomembranes typically exhibit anisotropic mechanical properties and deform alongside a particular direction. From an energy perspective, the helical shape usually results from the competition between bending and in-plane stretching energy driven by some internal or external force (including surface stress, residual stress, mismatch strain, and so on). The strain gradient in the flexible layer leads to bending along the direction with the smallest Young's modulus[162,163] and the twisting of the bilayer structure can be achieved by the strain gradient field introduced by the mismatch strain between the anisotropic bilayers.

Many helical structures have been found in many inorganic thin film systems[164] and have recently been reported in ferroelectric oxides. Despite the fragile ionic or covalent bonds in oxides, Dong *et al.* fabricated self-assembled $La_{0.7}Sr_{0.3}MnO_3/BaTiO_3$ (LSMO/BTO) ferroelectric nanosprings with excellent elasticity and recovering capability via a water-peeling off process[66]. The BTO nanospring could be stretched or compressed to the geometric limit without breaking failure, thereby achieving a considerable scalability of 500% [Figure 8A and G]. The corresponding bilayer fabrication process with a strain gradient can produce high-quality spring structures of ferroelectric oxides, which have wide applicability. The phase-field simulations reveal that the excellent scalability originates from the continuously rotating ferroelastic domain structures, which provide displacement tolerance and energy to accommodate complex strains of mixed bending and twisting during mechanical deformation. Figure 8B and H show the strain component distribution ε_{zz} of nanosprings under compression and elongation, respectively. This unique strain state results in the transition of 180° strip domains distributed around the surface of the ferroelectric nanospring, as shown in Figure 8C and I. For example, during the compression/elongation process, the outer and inner surfaces of the nanospring are subjected to opposite strains, which results in different ferroelectric domain structures on the two surfaces [Figure 8D, E, J and K]. It is noteworthy that the bending moment is the largest in the region farthest laterally from the centerline of the 3D helix (i.e., the middle region of a single helical structure); therefore, the strain effect in this region is more evident. For example, when the nanospring is stretched, the compressive strain on the outer surface of the middle region is more evident than the tensile strain on the inner surface, so the electric dipoles in this region deflected perpendicular to the *z*-axis, forming a 180° domain structure in the out-of-plane of the BTO layer.

Figure 8F and L show the relationship between the polarization and the strain distribution on the outer surface of the BTO nanospring under compression and elongation, respectively. When the BTO thin films are twisted into the self-assembled nanosprings, the electromechanical coupling behavior differs from the direct relationship between polarization and strain in the previous ferroelectric film state [Figure 9]. Furthermore, the effect of shear strain is different in the two states. In the previous ferroelectric thin film state, the shear strain has almost no effect on the domain structure; however, when the BTO film is twisted into a nanospring state, the effect of shear strain cannot be ignored. Therefore, the nanospring design provides a novel conceptual framework and platform for the strain engineering of freestanding ferroelectric thin films. Regarding the 3D helical structure, many experimental and theoretical works[163,165-167] have reported the shape transition and regulation by external fields of the helical structure. Therefore, the helical structure of ferroelectric oxides can be further regulated in morphology and properties by changing the geometric parameters, modulus ratio and pre-strain of the bilayer film. For example, the mechanical deformation of the nanospring can also be regulated by applying an electron-beam-induced field, which is expected to be applied in flexible nanorobots.

Through the nonlinear mechanical model of Euler buckling, a series of novel functional mechanical structures can be realized, including other self-assembled superstructures (such as origami, kirigami and

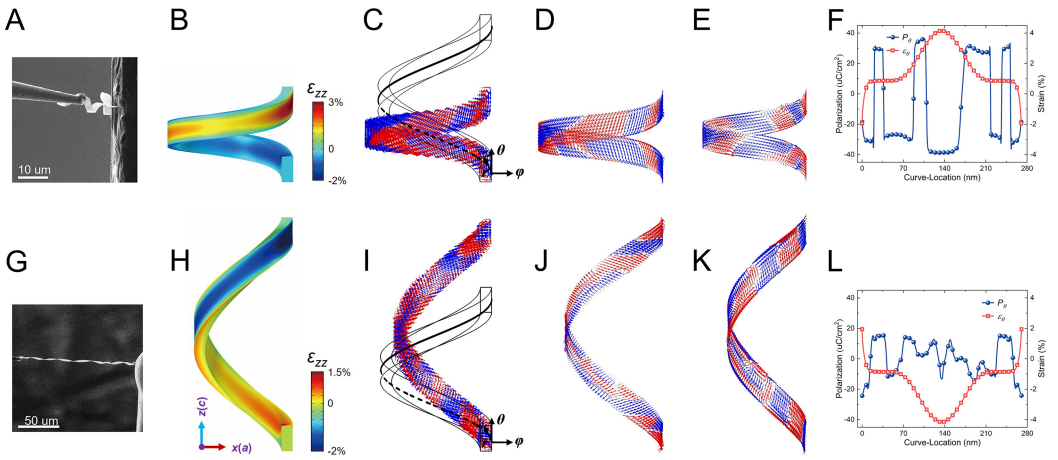

Figure 8. (A and G) In situ SEM images of the BTO nano-spring in compressive and tensile deformation, respectively. (B-F and H-L) Distribution of the strain component ε_{zz}, the domain structure, the outer surface domain, the inner surface domain, and the polarization component P_θ and strain distribution ε_θ along the middle line of the outer surface of the BTO nano-spring during compression and stretching, respectively. All panels reprinted with permission[66]. Copyright 2022, Wiley-VCH.

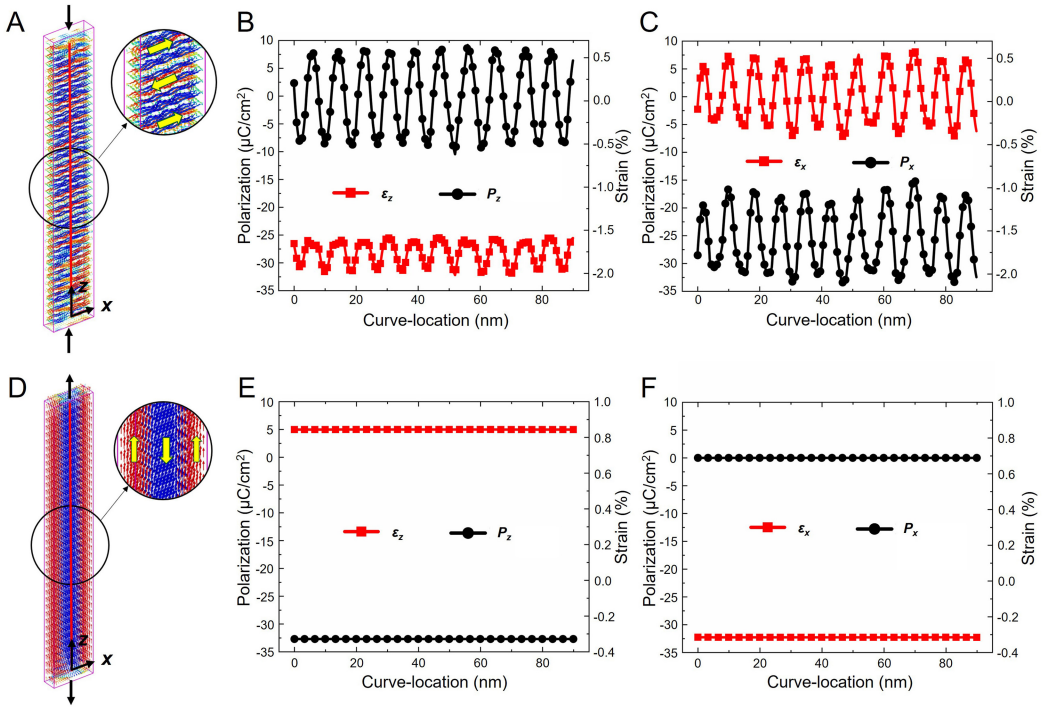

Figure 9. (A and D) The polarization distribution of BTO freestanding thin films under compressive and tensile deformation, respectively. [(B and C) and (E and F)] The polarization-strain distribution on the centerline of BTO freestanding thin films during compression and elongation, respectively. All panels reprinted with permission[66]. Copyright 2022, Wiley-VCH.

textile shapes), in addition to the previously reviewed wrinkled and helical structures. This mechanical modeling strategy based on these self-assembled 3D structure concepts can provide additional and unique ideas and solutions for developing and designing high-performance flexible ferroelectric devices. Furthermore, utilizing external stimuli (such as an external force or electric field) can qualitatively or even quantitatively manipulate the deformation of these mechanically buckling structures, providing a new

approach for strain engineering and domain engineering of freestanding ferroelectric systems.

CONCLUSION AND OUTLOOK

As reviewed in this article, super-elastic ferroelectric materials are expected to be applied in a wide range of flexible electronic devices, including flexible memories, nanosensors, and nanogenerators. It is essential that ferroelectric materials maintain stable electrical performance under various mechanical deformations, such as stretching, compression, bending and twisting, which involves the dynamic behavior of mesoscopic domain structures in the ferroelectric materials. However, the direct observation of domain structure evolution during continuous deformation of freestanding ferroelectric thin films is challenging for current experimental methods. Moreover, phase-field simulations have become increasingly critical in revealing the super-elasticity of freestanding ferroelectric films and the dynamical behavior of domain structures in different nanostructures. Therefore, the combination of experimental observations and phase-field simulations plays a crucial role in expanding the research and application of super-elastic ferroelectric materials in the field of flexible electronics. To further play the guiding role of theoretical modeling in super-elastic freestanding ferroelectric thin films, the following crucial issues deserve attention and solutions:

Flexoelectric effect. The flexoelectric effect describes the coupling between the electric polarization and strain gradient. Since the strain gradient is inversely proportional to the spatial scale (i.e., the gradient of the strain concerning the spatial coordinate), the flexoelectric effect is size-dependent[168]. Therefore, the flexoelectric effect becomes increasingly evident and prominent as the size diminishes, and its contribution to the domain engineering of super-elastic freestanding ferroelectric thin films cannot be ignored. However, the theories and algorithms considering the flexoelectric effect in the phase-field model of super-elastic ferroelectrics still need further verification and improvement. For the freestanding ferroelectric system under mechanical deformation, it is necessary to establish a phase-field model considering the flexoelectric effect to study the origin, enhancement and application of the flexoelectric effect on super-elasticity.

Design, fabrication and regulation of novel and functional mechanical structures. In the regulation and application of freestanding ferroelectric systems, the design and preparation of novel and functional mechanical structures are also the focus of research. The influence of 3D superstructures (e.g., isometric helicoids, kagome shapes and hexagonal honeycombs) on the polarization distribution of ferroelectrics also requires systematic research and analysis.

Responsive behavior in multiple fields. Freestanding ferroelectric thin film systems exhibit several novel topological phenomena and it is essential to demonstrate the response and regulation of these topological structures in multi-physical fields (e.g., individual or mixed applications of mechanical, electric and magnetic fields). In contrast, the response behavior of super-elastic freestanding ferroelectric nanostructures under the external field still needs further research and analysis. For example, the stretching and compressing behavior of ferroelectric nano-springs may be modulated by an electron-beam-induced field, which could have potential applications in the design of flexible nanorobots.

DECLARATIONS

Authors' contributions

Conceived and designed the manuscript: Huang HB, Guo CQ
Drafted and revised the manuscript: Huang HB, Guo CQ

Availability of data and materials

Not applicable.

Financial support and sponsorship

This work was financially supported by the National Natural Science Foundation of China (Grant No. 51972028) and the State Key Development Program for Basic Research of China (Grant No. 2019YFA0307900).

Conflicts of interest

All authors declared that there are no conflicts of interest.

Ethical approval and consent to participate

Not applicable.

Consent for publication

Not applicable.

REFERENCES

1. Hussain AM, Hussain MM. CMOS-technology-enabled flexible and stretchable electronics for internet of everything applications. *Adv Mater* 2016;28:4219-49. DOI PubMed
2. Vilouras A, Heidari H, Gupta S, Dahiya R. Modeling of CMOS devices and circuits on flexible ultrathin chips. *IEEE Trans Electron Devices* 2017;64:2038-46. DOI
3. Zhang H, Xiang L, Yang Y, et al. High-performance carbon nanotube complementary electronics and integrated sensor systems on ultrathin plastic foil. *ACS Nano* 2018;12:2773-9. DOI PubMed
4. Comiskey B, Albert JD, Yoshizawa H, Jacobson J. An electrophoretic ink for all-printed reflective electronic displays. *Nature* 1998;394:253-5. DOI
5. Rogers JA, Bao Z, Baldwin K, et al. Paper-like electronic displays: large-area rubber-stamped plastic sheets of electronics and microencapsulated electrophoretic inks. *Proc Natl Acad Sci USA* 2001;98:4835-40. DOI PubMed PMC
6. Gelinck GH, Huitema HE, van Veenendaal E, et al. Flexible active-matrix displays and shift registers based on solution-processed organic transistors. *Nat Mater* 2004;3:106-10. DOI PubMed
7. McAlpine MC, Ahmad H, Wang D, Heath JR. Highly ordered nanowire arrays on plastic substrates for ultrasensitive flexible chemical sensors. *Nat Mater* 2007;6:379-84. DOI PubMed PMC
8. Segev-Bar M, Haick H. Flexible sensors based on nanoparticles. *ACS Nano* 2013;7:8366-78. DOI PubMed
9. Lee HS, Chung J, Hwang G, et al. Flexible inorganic piezoelectric acoustic nanosensors for biomimetic artificial hair cells. *Adv Funct Mater* 2014;24:6914-21. DOI
10. Yamamoto Y, Harada S, Yamamoto D, et al. Printed multifunctional flexible device with an integrated motion sensor for health care monitoring. *Sci Adv* 2016;2:e1601473. DOI PubMed PMC
11. Wang X, Liu Z, Zhang T. Flexible sensing electronics for wearable/attachable health monitoring. *Small* 2017;13:1602790. DOI PubMed
12. Chen Y, Lu S, Zhang S, et al. Skin-like biosensor system via electrochemical channels for noninvasive blood glucose monitoring. *Sci Adv* 2017;3:e1701629. DOI PubMed PMC
13. Tee BC, Chortos A, Dunn RR, Schwartz G, Eason E, Bao Z. Tunable flexible pressure sensors using microstructured elastomer geometries for intuitive electronics. *Adv Funct Mater* 2014;24:5427-34. DOI
14. Wang Y, Zhu C, Pfattner R, et al. A highly stretchable, transparent, and conductive polymer. *Sci Adv* 2017;3:e1602076. DOI PubMed PMC
15. Lu L, Ding W, Liu J, Yang B. Flexible PVDF based piezoelectric nanogenerators. *Nano Energy* 2020;78:105251. DOI
16. Pan L, Yu G, Zhai D, et al. Hierarchical nanostructured conducting polymer hydrogel with high electrochemical activity. *Proc Natl Acad Sci USA* 2012;109:9287-92. DOI PubMed PMC
17. Sun JY, Zhao X, Illeperuma WR, et al. Highly stretchable and tough hydrogels. *Nature* 2012;489:133-6. DOI PubMed PMC
18. Kubo M, Li X, Kim C, et al. Stretchable microfluidic radiofrequency antennas. *Adv Mater* 2010;22:2749-52. DOI PubMed
19. Gao Y, Ota H, Schaler EW, et al. Wearable microfluidic diaphragm pressure sensor for health and tactile touch monitoring. *Adv*

Mater 2017;29:1701985. DOI PubMed
20. Yan J, Ren CE, Maleski K, et al. Flexible MXene/graphene films for ultrafast supercapacitors with outstanding volumetric capacitance. *Adv Funct Mater* 2017;27:1701264. DOI
21. Gao W, Zhu Y, Wang Y, Yuan G, Liu J. A review of flexible perovskite oxide ferroelectric films and their application. *J Mater* 2020;6:1-16. DOI
22. Bertoldi K, Vitelli V, Christensen J, van Hecke M. Flexible mechanical metamaterials. *Nat Rev Mater* 2017;2:1-11. DOI
23. Xue Z, Song H, Rogers JA, Zhang Y, Huang Y. Mechanically-guided structural designs in stretchable inorganic electronics. *Adv Mater* 2020;32:e1902254. DOI PubMed
24. Kim DH, Ahn JH, Choi WM, et al. Stretchable and foldable silicon integrated circuits. *Science* 2008;320:507-11. DOI PubMed
25. Bae HJ, Bae S, Yoon J, et al. Self-organization of maze-like structures via guided wrinkling. *Sci Adv* 2017;3:e1700071. DOI PubMed PMC
26. Peraza-hernandez EA, Hartl DJ, Malak Jr RJ, Lagoudas DC. Origami-inspired active structures: a synthesis and review. *Smart Mater Struct* 2014;23:094001. DOI
27. Song Z, Ma T, Tang R, et al. Origami lithium-ion batteries. *Nat Commun* 2014;5:3140. DOI PubMed
28. Shyu TC, Damasceno PF, Dodd PM, et al. A kirigami approach to engineering elasticity in nanocomposites through patterned defects. *Nat Mater* 2015;14:785-9. DOI PubMed
29. Callens SJ, Zadpoor AA. From flat sheets to curved geometries: origami and kirigami approaches. *Materials Today* 2018;21:241-64. DOI
30. Meng Y, Zhao Y, Hu C, et al. All-graphene core-sheath microfibers for all-solid-state, stretchable fibriform supercapacitors and wearable electronic textiles. *Adv Mater* 2013;25:2326-31. DOI PubMed
31. Ghosh T. Stretch, wrap, and relax to smartness. *Science* 2015;349:382-3. DOI PubMed
32. Scott JF, Paz de Araujo CA. Ferroelectric memories. *Science* 1989;246:1400-5. DOI PubMed
33. Auciello O, Scott JF, Ramesh R. The physics of ferroelectric memories. *Phys Today* 1998;51:22-7. DOI
34. Wang J, Ma J, Huang H, et al. Ferroelectric domain-wall logic units. *Nat Commun* 2022;13:3255. DOI PubMed PMC
35. Sun H, Wang J, Wang Y, et al. Nonvolatile ferroelectric domain wall memory integrated on silicon. *Nat Commun* 2022;13:4332. DOI PubMed PMC
36. Muralt P. Ferroelectric thin films for micro-sensors and actuators: a review. *J Micromecha Microeng* 2000;10:136-46. DOI
37. Damjanovic D, Muralt P, Setter N. Ferroelectric sensors. *IEEE Sensors J* 2001;1:191-206. DOI
38. Kirby P, Komuro E, Imura M, Zhang Q, Su Q, Whatmore R. High frequency thin film ferroelectric acoustic resonators and filters. *Integr Ferroelectr* 2001;41:91-100. DOI
39. Dragoman M, Aldrigo M, Modreanu M, Dragoman D. Extraordinary tunability of high-frequency devices using $Hf_{0.3}Zr_{0.7}O_2$ ferroelectric at very low applied voltages. *Appl Phys Lett* 2017;110:103104. DOI
40. Bowen CR, Kim HA, Weaver PM, Dunn S. Piezoelectric and ferroelectric materials and structures for energy harvesting applications. *Energy Environ Sci* 2014;7:25-44. DOI
41. Zhang Y, Phuong PTT, Roake E, et al. Thermal energy harvesting using pyroelectric-electrochemical coupling in ferroelectric materials. *Joule* 2020;4:301-9. DOI
42. Li Q, Han K, Gadinski MR, Zhang G, Wang Q. High energy and power density capacitors from solution-processed ternary ferroelectric polymer nanocomposites. *Adv Mater* 2014;26:6244-9. DOI PubMed
43. Thakur VK, Gupta RK. Recent progress on ferroelectric polymer-based nanocomposites for high energy density capacitors: synthesis, dielectric properties, and future aspects. *Chem Rev* 2016;116:4260-317. DOI PubMed
44. Xu K, Shi X, Dong S, Wang J, Huang H. Antiferroelectric phase diagram enhancing energy-storage performance by phase-field simulations. *ACS Appl Mater Interfaces* 2022;14:25770-80. DOI PubMed
45. Xu S, Shi X, Pan H, et al. Strain engineering of energy storage performance in relaxor ferroelectric thin film capacitors. *Adv Theory Simul* 2022;5:2100324. DOI
46. Ohigashi H, Koga K, Suzuki M, Nakanishi T, Kimura K, Hashimoto N. Piezoelectric and ferroelectric properties of P (VDF-TrFE) copolymers and their application to ultrasonic transducers. *Ferroelectrics* 1984;60:263-76. DOI
47. Zhang S, Li F, Jiang X, Kim J, Luo J, Geng X. Advantages and challenges of relaxor-$PbTiO_3$ Ferroelectric crystals for electroacoustic transducers-a review. *Prog Mater Sci* 2015;68:1-66. DOI PubMed PMC
48. Zhang G, Zhang X, Huang H, et al. Toward wearable cooling devices: highly flexible electrocaloric $Ba_{0.67}Sr_{0.33}TiO_3$ nanowire arrays. *Adv Mater* 2016;28:4811-6. DOI PubMed
49. Gao R, Shi X, Wang J, Zhang G, Huang H. Designed giant room-temperature electrocaloric effects in metal-free organic perovskite $[MDABCO](NH_4)I_3$ by phase-field simulations. *Adv Funct Mater* 2021;31:2104393. DOI
50. Qian X, Han D, Zheng L, et al. High-entropy polymer produces a giant electrocaloric effect at low fields. *Nature* 2021;600:664-9. DOI PubMed
51. Gao R, Shi X, Wang J, Huang H. Understanding electrocaloric cooling of ferroelectrics guided by phase-field modeling. *J Am Ceram Soc* 2022;105:3689-714. DOI
52. Ge JF, Liu ZL, Liu C, et al. Superconductivity above 100 K in single-layer FeSe films on doped $SrTiO_3$. *Nat Mater* 2015;14:285-9. DOI PubMed
53. Bégon-lours L, Rouco V, Sander A, et al. High-temperature-superconducting weak link defined by the ferroelectric field effect. *Phys*

Rev Appl 2017:7. DOI
54. Lynch CS, Chen L, Suo Z, Mcmeeking RM, Yang W. Crack growth in ferroelectric ceramics driven by cyclic polarization switching. *J Intell Mater Syst Struct* 1995;6:191-8. DOI
55. Arias I, Serebrinsky S, Ortiz M. A phenomenological cohesive model of ferroelectric fatigue. *Acta Mater* 2006;54:975-84. DOI
56. Horiuchi S, Tokura Y. Organic ferroelectrics. *Nat Mater* 2008;7:357-66. DOI PubMed
57. Bhansali US, Khan M, Alshareef H. Organic ferroelectric memory devices with inkjet-printed polymer electrodes on flexible substrates. *Microelect Eng* 2013;105:68-73. DOI
58. Zabek D, Taylor J, Boulbar EL, Bowen CR. Micropatterning of flexible and free standing polyvinylidene difluoride (PVDF) films for enhanced pyroelectric energy transformation. *Adv Energy Mater* 2015;5:1401891. DOI
59. Owczarek M, Hujsak KA, Ferris DP, et al. Flexible ferroelectric organic crystals. *Nat Commun* 2016;7:13108. DOI PubMed PMC
60. Guo M, Jiang J, Qian J, et al. Flexible robust and high-density FeRAM from array of organic ferroelectric nano-lamellae by self-assembly. *Adv Sci* 2019;6:1801931. DOI PubMed PMC
61. Dong G, Li S, Yao M, et al. Super-elastic ferroelectric single-crystal membrane with continuous electric dipole rotation. *Science* 2019;366:475-9. DOI PubMed
62. Guo C, Dong G, Zhou Z, et al. Domain evolution in bended freestanding $BaTiO_3$ ultrathin films: a phase-field simulation. *Appl Phys Lett* 2020;116:152903. DOI
63. Dong G, Li S, Li T, et al. Periodic wrinkle-patterned single-crystalline ferroelectric oxide membranes with enhanced piezoelectricity. *Adv Mater* 2020;32:e2004477. DOI PubMed
64. Zhou Y, Guo C, Dong G, et al. Tip-induced in-plane ferroelectric superstructure in zigzag-wrinkled $BaTiO_3$ thin films. *Nano Lett* 2022;22:2859-66. DOI PubMed
65. Guo M, Guo C, Han J, et al. Toroidal polar topology in strained ferroelectric polymer. *Science* 2021;371:1050-6. DOI PubMed
66. Dong G, Hu Y, Guo C, et al. Self-assembled epitaxial ferroelectric oxide nanospring with super-scalability. *Adv Mater* 2022;34:e2108419. DOI PubMed
67. Chen X, Li Q, Chen X, et al. Nano-imprinted ferroelectric polymer nanodot arrays for high density data storage. *Adv Funct Mater* 2013;23:3124-9. DOI
68. Fujikake H, Sato H, Murashige T. Polymer-stabilized ferroelectric liquid crystal for flexible displays. *Displays* 2004;25:3-8. DOI
69. Sekine T, Sugano R, Tashiro T, et al. Fully printed wearable vital sensor for human pulse rate monitoring using ferroelectric polymer. *Sci Rep* 2018;8:4442. DOI
70. Han X, Chen X, Tang X, Chen Y, Liu J, Shen Q. Flexible polymer transducers for dynamic recognizing physiological signals. *Adv Funct Mater* 2016;26:3640-8. DOI
71. Liu Z, Xu L, Zheng Q, et al. Human motion driven self-powered photodynamic system for long-term autonomous cancer therapy. *ACS Nano* 2020;14:8074-83. DOI PubMed
72. Shi Q, Wang T, Lee C. MEMS based broadband piezoelectric ultrasonic energy harvester (PUEH) for enabling self-powered implantable biomedical devices. *Sci Rep* 2016;6:24946. DOI PubMed PMC
73. Ryu J, Priya S, Park C, et al. Enhanced domain contribution to ferroelectric properties in freestanding thick films. *J Appl Phys* 2009;106:024108. DOI
74. Zuo Z, Chen B, Zhan Q, et al. Preparation and ferroelectric properties of freestanding $Pb(Zr,Ti)O_3$ thin membranes. *J Phys D Appl Phys* 2012;45:185302. DOI
75. Pesquera D, Parsonnet E, Qualls A, et al. Beyond substrates: strain engineering of ferroelectric membranes. *Adv Mater* 2020;32:e2003780. DOI PubMed
76. Shi Q, Parsonnet E, Cheng X, et al. The role of lattice dynamics in ferroelectric switching. *Nat Commun* 2022;13:1110. DOI PubMed PMC
77. Tian M, Xu L, Yang Y. Perovskite oxide ferroelectric thin films. *Adv Elect Mater* 2022;8:2101409. DOI PubMed
78. Jin C, Zhu Y, Han W, et al. Exchange bias in flexible freestanding $La_{0.7}Sr_{0.3}MnO_3/BiFeO_3$ membranes. *Appl Phys Lett* 2020;117:252902. DOI
79. Xu R, Huang J, Barnard ES, et al. Strain-induced room-temperature ferroelectricity in $SrTiO_3$ membranes. *Nat Commun* 2020;11:3141. DOI PubMed PMC
80. Chang L, You L, Wang J. The path to flexible ferroelectrics: approaches and progress. *Jpn J Appl Phys* 2018;57:0902A3. DOI
81. Yao M, Cheng Y, Zhou Z, Liu M. Recent progress on the fabrication and applications of flexible ferroelectric devices. *J Mater Chem C* 2020;8:14-27. DOI
82. Chiabrera FM, Yun S, Li Y, et al. Freestanding perovskite oxide films: synthesis, challenges, and properties. *Annalen Physik* 2022;534:2200084. DOI
83. Li S, Wang Y, Yang M, et al. Ferroelectric thin films: performance modulation and application. *Mater Adv* 2022;3:5735-52. DOI
84. Won SS, Seo H, Kawahara M, et al. Flexible vibrational energy harvesting devices using strain-engineered perovskite piezoelectric thin films. *Nano Energy* 2019;55:182-92. DOI
85. De Dobbelaere C, Calzada ML, Jiménez R, et al. Aqueous solutions for low-temperature photoannealing of functional oxide films: reaching the 400 °C Si-technology integration barrier. *J Am Chem Soc* 2011;133:12922-5. DOI PubMed
86. Bretos I, Jiménez R, Ricote J, Calzada ML. Low-temperature crystallization of solution-derived metal oxide thin films assisted by chemical processes. *Chem Soc Rev* 2018;47:291-308. DOI PubMed

87. Bretos I, Jimenez R, Ricote J, Calzada ML. Low-temperature solution approaches for the potential integration of ferroelectric oxide films in flexible electronics. *IEEE Trans Ultrason Ferroelectr Freq Control* 2020;67:1967-79. DOI PubMed
88. Bretos I, Jiménez R, Ricote J, Sirera R, Calzada ML. Photoferroelectric thin films for flexible systems by a three-in-one solution-based approach. *Adv Funct Mater* 2020;30:2001897. DOI
89. Barrios Ó, Jiménez R, Ricote J, Tartaj P, Calzada ML, Bretos Í. A sustainable self-induced solution seeding approach for multipurpose $BiFeO_3$ active layers in flexible electronic devices. *Adv Funct Mater* 2022;32:2112944. DOI
90. Jiang J, Bitla Y, Huang CW, et al. Flexible ferroelectric element based on van der Waals heteroepitaxy. *Sci Adv* 2017;3:e1700121. DOI
91. Zheng M, Li X, Ni H, Li X, Gao J. van der Waals epitaxy for highly tunable all-inorganic transparent flexible ferroelectric luminescent films. *J Mater Chem C* 2019;7:8310-5. DOI
92. Bitla Y, Chu YH. van der Waals oxide heteroepitaxy for soft transparent electronics. *Nanoscale* 2020;12:18523-44. DOI PubMed
93. Lee SA, Hwang JY, Kim ES, Kim SW, Choi WS. Highly oriented $SrTiO_3$ Thin film on graphene substrate. *ACS Appl Mater Inter* 2017;9:3246-50. DOI PubMed
94. Kum HS, Lee H, Kim S, et al. Heterogeneous integration of single-crystalline complex-oxide membranes. *Nature* 2020;578:75-81. DOI PubMed
95. Wong WS, Sands T, Cheung NW. Damage-free separation of GaN thin films from sapphire substrates. *Appl Phys Lett* 1998;72:599-601. DOI
96. Xu J, Zhang R, Wang Y, et al. Preparation of large area freestanding GaN by laser lift-off technology. *Mater Lett* 2002;56:43-6. DOI
97. Lin I, Hsieh K, Lee K, Tai N. Preparation of ferroelectric Pb(Zr1-xTix)O_3/Si films by laser lift-off technique. *J Eur Ceram Soc* 2004;24:975-8. DOI
98. Lee CH, Kim SJ, Oh Y, Kim MY, Yoon Y, Lee H. Use of laser lift-off for flexible device applications. *J Appl Phys* 2010;108:102814. DOI
99. Zhang Y, Ma C, Lu X, Liu M. Recent progress on flexible inorganic single-crystalline functional oxide films for advanced electronics. *Mater Horiz* 2019;6:911-30. DOI
100. Bakaul SR, Serrao CR, Lee M, et al. Single crystal functional oxides on silicon. *Nat Commun* 2016;7:10547. DOI PubMed PMC
101. Bakaul SR, Prokhorenko S, Zhang Q, et al. Freestanding ferroelectric bubble domains. *Adv Mater* 2021;33:e2105432. DOI PubMed
102. Lu D, Baek DJ, Hong SS, Kourkoutis LF, Hikita Y, Hwang HY. Synthesis of freestanding single-crystal perovskite films and heterostructures by etching of sacrificial water-soluble layers. *Nat Mater* 2016;15:1255-60. DOI PubMed
103. Baek DJ, Lu D, Hikita Y, Hwang HY, Kourkoutis LF. Ultrathin epitaxial barrier layer to avoid thermally induced phase transformation in oxide heterostructures. *ACS Appl Mater Inter* 2017;9:54-9. DOI PubMed
104. Hong SS, Yu JH, Lu D, et al. Two-dimensional limit of crystalline order in perovskite membrane films. *Sci Adv* 2017;3:eaao5173. DOI PubMed PMC
105. Ji D, Cai S, Paudel TR, et al. Freestanding crystalline oxide perovskites down to the monolayer limit. *Nature* 2019;570:87-90. DOI PubMed
106. Han L, Fang Y, Zhao Y, et al. Giant uniaxial strain ferroelectric domain tuning in freestanding $PbTiO_3$ films. *Adv Mater Inter* 2020;7:1901604. DOI
107. Takahashi R, Lippmaa M. Sacrificial water-soluble BaO layer for fabricating free-standing piezoelectric membranes. *ACS Appl Mater Inter* 2020;12:25042-9. DOI PubMed
108. Zhong H, Li M, Zhang Q, et al. Large-scale $Hf_{0.5}Zr_{0.5}O_2$ membranes with robust ferroelectricity. *Adv Mater* 2022;34:e2109889. DOI PubMed
109. Guo R, You L, Lin W, et al. Continuously controllable photoconductance in freestanding $BiFeO_3$ by the macroscopic flexoelectric effect. *Nat Commun* 2020;11:2571. DOI PubMed PMC
110. Peng B, Peng RC, Zhang YQ, et al. Phase transition enhanced superior elasticity in freestanding single-crystalline multiferroic $BiFeO_3$ membranes. *Sci Adv* 2020;6:eaba5847. DOI PubMed PMC
111. Jin C, Zhu Y, Li X, et al. Super-flexible freestanding $BiMnO_3$ membranes with stable ferroelectricity and ferromagnetism. *Adv Sci* 2021;8:e2102178. DOI PubMed PMC
112. Han L, Addiego C, Prokhorenko S, et al. High-density switchable skyrmion-like polar nanodomains integrated on silicon. *Nature* 2022;603:63-7. DOI PubMed
113. Elangovan H, Barzilay M, Seremi S, et al. Giant superelastic piezoelectricity in flexible ferroelectric $BaTiO_3$ membranes. *ACS Nano* 2020;14:5053-60. DOI PubMed
114. Cai S, Lun Y, Ji D, et al. Enhanced polarization and abnormal flexural deformation in bent freestanding perovskite oxides. *Nat Commun* 2022;13:5116. DOI PubMed PMC
115. Chen L. Phase-field models for microstructure evolution. *Annu Rev Mater Res* 2002;32:113-40. DOI
116. Artyukhin S, Delaney KT, Spaldin NA, Mostovoy M. Landau theory of topological defects in multiferroic hexagonal manganites. *Nat Mater* 2014;13:42-9. DOI PubMed
117. Xue F, Wang X, Shi Y, Cheong S, Chen L. Strain-induced incommensurate phases in hexagonal manganites. *Phys Rev B* 2017;96:104109. DOI
118. Wang J, Shi S, Chen L, Li Y, Zhang T. Phase-field simulations of ferroelectric/ferroelastic polarization switching. *Acta Materialia* 2004;52:749-64. DOI

119. Cao W. Constructing landau-ginzburg-devonshire type models for ferroelectric systems based on symmetry. *Ferroelectrics* 2008;375:28-39. DOI
120. Chen L. Phase-field method of phase transitions/domain structures in ferroelectric thin films: a review. *J Am Ceram Soc* 2008;91:1835-44. DOI
121. Chen HT, Soh AK, Ni Y. Phase field modeling of flexoelectric effects in ferroelectric epitaxial thin films. *Acta Mech* 2014;225:1323-33. DOI
122. Wang J, Wang B, Chen L. Understanding, predicting, and designing ferroelectric domain structures and switching guided by the phase-field method. *Annu Rev Mater Res* 2019;49:127-52. DOI
123. Peng R, Cheng X, Peng B, Zhou Z, Chen L, Liu M. Domain patterns and super-elasticity of freestanding $BiFeO_3$ membranes via phase-field simulations. *Acta Materialia* 2021;208:116689. DOI
124. Peng R, Cheng X, Peng B, Zhou Z, Chen L, Liu M. Boundary conditions manipulation of polar vortex domains in $BiFeO_3$ membranes via phase-field simulations. *J Phys D Appl Phys* 2021;54:495301. DOI
125. Chen WJ, Zheng Y, Xiong WM, Feng X, Wang B, Wang Y. Effect of mechanical loads on stability of nanodomains in ferroelectric ultrathin films: towards flexible erasing of the non-volatile memories. *Sci Rep* 2014;4:5339. DOI PubMed PMC
126. Lacour S, Jones J, Suo Z, Wagner S. Design and performance of thin metal film interconnects for skin-like electronic circuits. *IEEE Electron Device Lett* 2004;25:179-81. DOI
127. Cheng H, Zhang Y, Hwang K, Rogers JA, Huang Y. Buckling of a stiff thin film on a pre-strained bi-layer substrate. *Int J Solids Struct* 2014;51:3113-8. DOI
128. Pan K, Ni Y, He L, Huang R. Nonlinear analysis of compressed elastic thin films on elastic substrates: from wrinkling to buckle-delamination. *Int J Solids Struct* 2014;51:3715-26. DOI
129. Xu F, Potier-ferry M, Belouettar S, Cong Y. 3D finite element modeling for instabilities in thin films on soft substrates. *Int J Solids Struct* 2014;51:3619-32. DOI
130. Yan D, Zhang K, Hu G. Wrinkling of structured thin films via contrasted materials. *Soft Matter* 2016;12:3937-42. DOI PubMed
131. Park HG, Jeong HC, Jung YH, Seo DS. Control of the wrinkle structure on surface-reformed poly(dimethylsiloxane) via ion-beam bombardment. *Sci Rep* 2015;5:12356. DOI PubMed PMC
132. Zhu W, Low T, Perebeinos V, et al. Structure and electronic transport in graphene wrinkles. *Nano Lett* 2012;12:3431-6. DOI PubMed
133. Chung JY, Nolte AJ, Stafford CM. Diffusion-controlled, self-organized growth of symmetric wrinkling patterns. *Adv Mater* 2009;21:1358-62. DOI
134. Guvendiren M, Yang S, Burdick JA. Swelling-induced surface patterns in hydrogels with gradient crosslinking density. *Adv Funct Mater* 2009;19:3038-45. DOI
135. Jiang H, Khang DY, Song J, Sun Y, Huang Y, Rogers JA. Finite deformation mechanics in buckled thin films on compliant supports. *Proc Natl Acad Sci USA* 2007;104:15607-12. DOI PubMed PMC
136. Hendricks TR, Wang W, Lee I. Buckling in nanomechanical films. *Soft Matter* 2010;6:3701. DOI
137. Huang Z, Hong W, Suo Z. Nonlinear analyses of wrinkles in a film bonded to a compliant substrate. *J Mech Phys Solids* 2005;53:2101-18. DOI
138. Genzer J, Groenewold J. Soft matter with hard skin: From skin wrinkles to templating and material characterization. *Soft Matter* 2006;2:310-23. DOI PubMed
139. Audoly B, Boudaoud A. Buckling of a stiff film bound to a compliant substrate-part I: formulation, linear stability of cylindrical patterns, secondary bifurcations. *J Mech Phys Solids* 2008;56:2401-21. DOI
140. Zhang Y, Zhang F, Yan Z, et al. Printing, folding and assembly methods for forming 3D mesostructures in advanced materials. *Nat Rev Mater* 2017:2. DOI
141. Rogers JA, Someya T, Huang Y. Materials and mechanics for stretchable electronics. *Science* 2010;327:1603-7. DOI PubMed
142. Kim JB, Kim P, Pégard NC, et al. Wrinkles and deep folds as photonic structures in photovoltaics. *Nat Photon* 2012;6:327-32. DOI
143. Zhang W, Zhang Y, Qiu J, Zhao Z, Liu N. Topological structures of transition metal dichalcogenides: a review on fabrication, effects, applications, and potential. *InfoMat* 2021;3:133-54. DOI
144. Stafford CM, Harrison C, Beers KL, et al. A buckling-based metrology for measuring the elastic moduli of polymeric thin films. *Nat Mater* 2004;3:545-50. DOI PubMed
145. Chung JY, Nolte AJ, Stafford CM. Surface wrinkling: a versatile platform for measuring thin-film properties. *Adv Mater* 2011;23:349-68. DOI PubMed
146. Dervaux J, Couder Y, Guedeau-Boudeville MA, Ben Amar M. Shape transition in artificial tumors: from smooth buckles to singular creases. *Phys Rev Lett* 2011;107:018103. DOI PubMed
147. Guvendiren M, Burdick JA, Yang S. Solvent induced transition from wrinkles to creases in thin film gels with depth-wise crosslinking gradients. *Soft Matter* 2010;6:5795. DOI
148. Tan Y, Hu B, Song J, Chu Z, Wu W. Bioinspired multiscale wrinkling patterns on curved substrates: an overview. *Nanomicro Lett* 2020;12:101. DOI PubMed PMC
149. Naumov II, Bellaiche L, Fu H. Unusual phase transitions in ferroelectric nanodisks and nanorods. *Nature* 2004;432:737-40. DOI PubMed
150. Tang YL, Zhu YL, Ma XL, et al. Observation of a periodic array of flux-closure quadrants in strained ferroelectric $PbTiO_3$ films.

Science 2015;348:547-51. DOI PubMed
151. Hadjimichael M, Li Y, Zatterin E, et al. Metal-ferroelectric supercrystals with periodically curved metallic layers. *Nat Mater* 2021;20:495-502. DOI PubMed
152. Yadav AK, Nelson CT, Hsu SL, et al. Observation of polar vortices in oxide superlattices. *Nature* 2016;530:198-201. DOI
153. Hong Z, Damodaran AR, Xue F, et al. Stability of polar vortex lattice in ferroelectric superlattices. *Nano Lett* 2017;17:2246-52. DOI PubMed
154. Liu D, Shi X, Wang J, Cheng X, Huang H. Phase-field simulations of surface charge-induced ferroelectric vortex. *J Phys D Appl Phys* 2021;54:405302. DOI
155. Liu D, Wang J, Jafri HM, et al. Phase-field simulations of vortex chirality manipulation in ferroelectric thin films. *NPJ Quantum Mater* 2022:7. DOI
156. Das S, Tang YL, Hong Z, et al. Observation of room-temperature polar skyrmions. *Nature* 2019;568:368-72. DOI PubMed
157. Zhang Y, Li Q, Huang H, Hong J, Wang X. Strain manipulation of ferroelectric skyrmion bubbles in a freestanding $PbTiO_3$ film: a phase field simulation. *Phys Rev B* 2022:105. DOI
158. Wang YJ, Feng YP, Zhu YL, et al. Polar meron lattice in strained oxide ferroelectrics. *Nat Mater* 2020;19:881-6. DOI PubMed
159. Vasudevan RK, Chen YC, Tai HH, et al. Exploring topological defects in epitaxial BiFeO3 thin films. *ACS Nano* 2011;5:879-87. DOI PubMed
160. Wang X, Mostovoy M, Han MG, et al. Unfolding of vortices into topological stripes in a multiferroic material. *Phys Rev Lett* 2014;112:247601. DOI PubMed
161. Shimada T, Lich le V, Nagano K, Wang J, Kitamura T. Hierarchical ferroelectric and ferrotoroidic polarizations coexistent in nano-metamaterials. *Sci Rep* 2015;5:14653. DOI PubMed PMC
162. Cavallo F, Lagally MG. Semiconductors turn soft: inorganic nanomembranes. *Soft Matter* 2010;6:439-55. DOI
163. Chen Z, Huang G, Trase I, Han X, Mei Y. Mechanical self-assembly of a strain-engineered flexible layer: wrinkling, rolling, and twisting. *Phys Rev Applied* 2016:5. DOI
164. Yang M, Kotov NA. Nanoscale helices from inorganic materials. *J Mater Chem* 2011;21:6775. DOI
165. Guo Q, Mehta AK, Grover MA, Chen W, Lynn DG, Chen Z. Shape selection and multi-stability in helical ribbons. *Appl Phys Lett* 2014;104:211901. DOI
166. Guo Q, Chen Z, Li W, et al. Mechanics of tunable helices and geometric frustration in biomimetic seashells. *EPL Europhys Lett* 2014;105:64005. DOI
167. Yu X, Zhang L, Hu N, et al. Shape formation of helical ribbons induced by material anisotropy. *Appl Phys Lett* 2017;110:091901. DOI
168. Wang B, Gu Y, Zhang S, Chen L. Flexoelectricity in solids: progress, challenges, and perspectives. *Prog Mater Sci* 2019;106:100570. DOI

AUTHOR INSTRUCTIONS

1. Submission Overview

Before you decide to publish with *Microstructures*, please read the following items carefully and make sure that you are well aware of Editorial Policies and the following requirements.

1.1 Topic Suitability

The topic of the manuscript must fit the scope of the journal. Please refer to Aims and Scope for more information.

1.2 Open Access and Copyright

The journal adopts Gold Open Access publishing model and distributes content under the Creative Commons Attribution 4.0 International License. Copyright is retained by authors. Please make sure that you are well aware of these policies.

1.3 Publication Fees

Microstructures is an open access journal. When a paper is accepted for publication, authors are required to pay Article Processing Charges (APCs) to cover its editorial and production costs. The APC for each submission is $600. There are no additional charges based on color, length, figures, or other elements. For more details, please refer to OAE Publication Fees.

1.4 Language Editing

All submissions are required to be presented clearly and cohesively in good English. Authors whose first language is not English are advised to have their manuscripts checked or edited by a native English speaker before submission to ensure the high quality of expression. A well-organized manuscript in good English would make the peer review even the whole editorial handling more smoothly and efficiently.

If needed, authors are recommended to consider the language editing services provided by Charlesworth to ensure that the manuscript is written in correct scientific English before submission. Authors who publish with OAE journals enjoy a special discount for the services of Charlesworth via the following two ways.

Submit your manuscripts directly at http://www.charlesworthauthorservices.com/~OAE;

Open the link http://www.charlesworthauthorservices.com/, and enter Promotion Code “OAE” when you submit.

1.5 Work Funded by the National Institutes of Health

If an accepted manuscript was funded by National Institutes of Health (NIH), the author may inform editors of the NIH funding number. The editors are able to deposit the paper to the NIH Manuscript Submission System on behalf of the author.

2. Submission Preparation

2.1 Cover Letter

A cover letter is required to be submitted accompanying each manuscript. It should be concise and explain why the study is significant, why it fits the scope of the journal, and why it would be attractive to readers, etc.

Here is a guideline of a cover letter for authors’ consideration:

In the first paragraph: include the title and type (e.g., Research Article, Review Article, etc.) of the manuscript, a brief on the background of the study, the question the author sought out to answer and why;

In the second paragraph: concisely explain what was done, the main findings and why they are significant;

In the third paragraph: indicate why the manuscript fits the Aims and Scope of the journal, and why it would be attractive to readers;

In the fourth paragraph: confirm that the manuscript has not been published elsewhere and not under consideration of any other journal. All authors have approved the manuscript and agreed on its submission to the journal. Journal’s specific requirements have been met if any.

If the manuscript is contributed to a special issue, please also mention it in the cover letter.

If the manuscript was presented partly or entirely in a conference, the author should clearly state the background information of the event, including the conference name, time and place in the cover letter.

2.2 Types of Manuscripts

There is no restriction on the length of manuscripts, number of figures, tables and references, provided that the manuscript is concise and comprehensive. The journal publishes Research Article, Review Article, Editorial, Perspective etc. For more details about paper type, please refer to the following table.

Manuscript Type	Definition	Abstract	Keywords	Main Text Structure
Research Article	A Research Article describes detailed results from novel research. All findings are extensively discussed.	Structured abstract including Aim, Methods, Results and Conclusion. No more than 250 words.	3-8 keywords	The main content should include four sections: Introduction, Materials and Methods, Results and Discussion.
Review Article	A Review Article summarizes the literature on previous studies. It usually does not present any new information on a subject.	Unstructured abstract. No more than 250 words.	3-8 keywords	The main text may consist of several sections with unfixed section titles. We suggest that the author include an "Introduction" section at the beginning, several sections with unfixed titles in the middle part, and a "Conclusion" section in the end.
Meta-Analysis	A Meta-Analysis is a statistical analysis combining the results of multiple scientific studies. It is often an overview of clinical trials.	Structured abstract including Aim, Methods, Results and Conclusion. No more than 250 words.	3-8 keywords	The main content should include four sections: Introduction, Methods, Results and Discussion.
Technical Note	A Technical Note is a short article giving a brief description of a specific development, technique or procedure, or it may describe a modification of an existing technique, procedure or device applied in research.	Unstructured abstract. No more than 250 words.	3-8 keywords	/
Commentary	A Commentary is to provide comments on a newly published article or an alternative viewpoint on a certain topic.	Unstructured abstract. No more than 250 words.	3-8 keywords	/
Editorial	An Editorial is a short article describing news about the journal or opinions of senior editors or the publisher.	None required.	None required.	/
Letter to Editor	A Letter to Editor is usually an open post-publication review of a paper from its readers, often critical of some aspect of a published paper. Controversial papers often attract numerous Letters to Editor.	Unstructured abstract (optional). No more than 250 words.	3-8 keywords (optional)	/
Opinion	An Opinion usually presents personal thoughts, beliefs, or feelings on a topic.	Unstructured abstract (optional). No more than 250 words.	3-8 keywords	/
Perspective	A Perspective provides personal points of view on the state-of-the-art of a specific area of knowledge and its future prospects. Links to areas of intense current research focus can also be made. The emphasis should be on a personal assessment rather than a comprehensive, critical review. However, comments should be put into the context of existing literature. Perspectives are usually invited by the Editors.	Unstructured abstract. No more than 150 words.	3-8 keywords	/

2.3 Manuscript Structure

2.3.1 Front Matter

2.3.1.1 Title

The title of the manuscript should be concise, specific and relevant, with no more than 16 words if possible. When gene or protein names are included, the abbreviated name rather than full name should be used.

2.3.1.2 Authors and Affiliations

Authors' full names should be listed. The initials of middle names can be provided. Institutional addresses and email addresses for all authors should be listed. At least one author should be designated as corresponding author. In addition, corresponding authors are suggested to provide their Open Researcher and Contributor ID upon submission. Please note that any change to authorship is not allowed after manuscript acceptance.

2.3.1.3 Highlights

Highlights are mandatory because they can help increase the discoverability of your article through search engines. They consist of a short collection of bullet points that capture the novel results of your research as well as new methods that were used during the study (if any). They should be submitted in a separate editable file in the online submission system. Please use 'Highlights' in the file name and include 3 to 5 bullet points (maximum 85 characters per bullet point, including spaces).

2.3.1.4 Abstract

The abstract should be a single paragraph with word limitation and specific structure requirements (for more details please refer to Types of Manuscripts). It usually describes the main objective(s) of the study, explains how the study was done, including any model organisms used, without methodological detail, and summarizes the most important results and their significance. The abstract must be an objective representation of the study: it is not allowed to contain results which are not presented and substantiated in the manuscript, or exaggerate the main conclusions. Citations should not be included in the abstract.

2.3.1.5 Graphical Abstract

The graphical abstract is essential as this can catch first view of your publication by readers. We recommend you to submit an eye-catching figure. It should summarize the content of the article in a concise graphical form. It is recommended to use it because this can make online articles get more attention. The graphic abstract should be submitted as a separate document in the online submission system. Please provide an image with a minimum of 730 × 1,228 pixels (h × w) or proportionally more. The image should be readable at a size of 7 × 12 cm using a regular screen resolution of 96 dpi. Preferred file types: TIFF, PSD, AI, JPG, JPEG, EPS, PNG, ZIP and PDF files.

2.3.1.6 Keywords

Three to eight keywords should be provided, which are specific to the article, yet reasonably common within the subject discipline.

2.3.2 Main Text

Manuscripts of different types are structured with different sections of content. Please refer to Types of Manuscripts to make sure which sections should be included in the manuscripts.

2.3.2.1 Introduction

The introduction should contain background that puts the manuscript into context, allow readers to understand why the study is important, include a brief review of key literature, and conclude with a brief statement of the overall aim of the work and a comment about whether that aim was achieved. Relevant controversies or disagreements in the field should be introduced as well.

2.3.2.2 Materials and Methods

Materials and Methods should contain sufficient details to allow others to fully replicate the study. New methods and protocols should be described in detail while well-established methods can be briefly described or appropriately cited. Experimental participants selected, the drugs and chemicals used, the statistical methods taken, and the computer software used should be identified precisely. Statistical terms, abbreviations, and all symbols used should be defined clearly. Protocol documents for clinical trials, observational studies, and other non-laboratory investigations may be uploaded as supplementary materials.

2.3.2.3 Results and Discussion

This section should contain the findings of the study and discuss the implications of the findings in context of existing research and highlight limitations of the study. Future research directions may also be mentioned. Results of statistical analysis should also be included either as text or as tables or figures if appropriate. Authors should emphasize and summarize

only the most important observations. Data on all primary and secondary outcomes identified in the section Methods should also be provided. Extra or supplementary materials and technical details can be placed in supplementary documents.

2.3.2.4 Conclusions

It should state clearly the main conclusions and include the explanation of their relevance or importance to the field.

2.3.3 Back Matter

2.3.3.1 Acknowledgments

Anyone who contributed towards the article but does not meet the criteria for authorship, including those who provided professional writing services or materials, should be acknowledged. Authors should obtain permission to acknowledge from all those mentioned in the Acknowledgments section. This section is not added if the author does not have anyone to acknowledge.

2.3.3.2 Authors' Contributions

Each author is expected to have made substantial contributions to the conception or design of the work, or the acquisition, analysis, or interpretation of data, or the creation of new software used in the work, or have drafted the work or substantively revised it.

Please use Surname and Initial of Forename to refer to an author's contribution. For example: made substantial contributions to conception and design of the study and performed data analysis and interpretation: Salas H, Castaneda WV; performed data acquisition, as well as provided administrative, technical, and material support: Castillo N, Young V.

If an article is single-authored, please include "The author contributed solely to the article." in this section.

2.3.3.3 Availability of Data and Materials

In order to maintain the integrity, transparency and reproducibility of research records, authors should include this section in their manuscripts, detailing where the data supporting their findings can be found. Data can be deposited into data repositories or published as supplementary information in the journal. Authors who cannot share their data should state that the data will not be shared and explain it. If a manuscript does not involve such issue, please state "Not applicable." in this section.

2.3.3.4 Financial Support and Sponsorship

All sources of funding for the study reported should be declared. The role of the funding body in the experiment design, collection, analysis and interpretation of data, and writing of the manuscript should be declared. Any relevant grant numbers and the link of funder's website should be provided if any. If the study is not involved with this issue, state "None." in this section.

2.3.3.5 Conflicts of Interest

Authors must declare any potential conflicts of interest that may be perceived as inappropriately influencing the representation or interpretation of reported research results. If there are no conflicts of interest, please state "All authors declared that there are no conflicts of interest." in this section. Some authors may be bound by confidentiality agreements. In such cases, in place of itemized disclosures, we will require authors to state "All authors declare that they are bound by confidentiality agreements that prevent them from disclosing their conflicts of interest in this work.". If authors are unsure whether conflicts of interest exist, please refer to the "Conflicts of Interest" of *Microstructures* Editorial Policies for a full explanation.

2.3.3.6 Copyright

Authors retain copyright of their works through a Creative Commons Attribution 4.0 International License that clearly states how readers can copy, distribute, and use their attributed research, free of charge. A declaration "© The Author(s) 2022." will be added to each article. Authors are required to sign License to Publish before formal publication.

2.3.3.7 References

References should be numbered in order of appearance at the end of manuscripts. In the text, reference numbers should be placed in square brackets and the corresponding references are cited thereafter. If the number of authors is less than or equal to six, we require to list all authors' names. If the number of authors is more than six, only the first three authors' names are required to be listed in the references, other authors' names should be omitted and replaced with "et al.". Abbreviations of the journals should be provided on the basis of Index Medicus. Information from manuscripts accepted but not published should be cited in the text as "Unpublished material" with written permission from the source.

References should be described as follows, depending on the types of works:

Types	Examples
Journal articles by individual authors	Weaver DL, Ashikaga T, Krag DN, et al. Effect of occult metastases on survival in node-negative breast cancer. *N Engl J Med* 2011;364:412-21. [DOI: 10.1056/NEJMoa1008108]

Organization as author	Diabetes Prevention Program Research Group. Hypertension, insulin, and proinsulin in participants with impaired glucose tolerance. *Hypertension* 2002;40:679-86. [DOI: 10.1161/01.hyp.0000035706.28494.09]
Both personal authors and organization as author	Vallancien G, Emberton M, Harving N, van Moorselaar RJ; Alf-One Study Group. Sexual dysfunction in 1,274 European men suffering from lower urinary tract symptoms. *J Urol* 2003;169:2257-61. [DOI: 10.1097/01.ju.0000067940.76090.73]
Journal articles not in English	Zhang X, Xiong H, Ji TY, Zhang YH, Wang Y. Case report of anti-N-methyl-D-aspartate receptor encephalitis in child. *J Appl Clin Pediatr* 2012;27:1903-7. (in Chinese)
Journal articles ahead of print	Odibo AO. Falling stillbirth and neonatal mortality rates in twin gestation: not a reason for complacency. *BJOG* 2018; Epub ahead of print [DOI: 10.1111/1471-0528.15541]
Books	Sherlock S, Dooley J. Diseases of the liver and billiary system. 9th ed. Oxford: Blackwell Sci Pub; 1993. pp. 258-96.
Book chapters	Meltzer PS, Kallioniemi A, Trent JM. Chromosome alterations in human solid tumors. In: Vogelstein B, Kinzler KW, editors. The genetic basis of human cancer. New York: McGraw-Hill; 2002. pp. 93-113.
Online resource	FDA News Release. FDA approval brings first gene therapy to the United States. Available from: https://www.fda.gov/NewsEvents/Newsroom/PressAnnouncements/ucm574058.htm. [Last accessed on 30 Oct 2017]
Conference proceedings	Harnden P, Joffe JK, Jones WG, editors. Germ cell tumours V. Proceedings of the 5th Germ Cell Tumour Conference; 2001 Sep 13-15; Leeds, UK. New York: Springer; 2002..
Conference paper	Christensen S, Oppacher F. An analysis of Koza's computational effort statistic for genetic programming. In: Foster JA, Lutton E, Miller J, Ryan C, Tettamanzi AG, Editors. Genetic programming. EuroGP 2002: Proceedings of the 5th European Conference on Genetic Programming; 2002 Apr 3-5; Kinsdale, Ireland. Berlin: Springer; 2002. pp. 182-91.
Unpublished material	Tian D, Araki H, Stahl E, Bergelson J, Kreitman M. Signature of balancing selection in Arabidopsis. *Proc Natl Acad Sci U S A*. Forthcoming 2002.

For other types of references, please refer to U.S. National Library of Medicine.

The journal also recommends that authors prepare references with a bibliography software package, such as EndNote to avoid typing mistakes and duplicated references.

2.3.3.8 Supplementary Materials

Additional data and information can be uploaded as Supplementary Materials to accompany the manuscripts. The supplementary materials will also be available to the referees as part of the peer-review process. Any file format is acceptable, such as data sheet (word, excel, csv, cdx, fasta, pdf or zip files), presentation (powerpoint, pdf or zip files), image (cdx, eps, jpeg, pdf, png or tiff), table (word, excel, csv or pdf), audio (mp3, wav or wma) or video (avi, divx, flv, mov, mp4, mpeg, mpg or wmv). All information should be clearly presented. Supplementary materials should be cited in the main text in numeric order (e.g., Supplementary Figure 1, Supplementary Figure 2, Supplementary Table 1, Supplementary Table 2, etc.). The style of supplementary figures or tables complies with the same requirements on figures or tables in main text. Videos and audios should be prepared in English, and limited to a size of 500 MB.

2.4 Manuscript Format

2.4.1 File Format

Manuscript files can be in DOC and DOCX formats and should not be locked or protected.

2.4.2 Length

There are no restrictions on paper length, number of figures, or number of supporting documents. Authors are encouraged to present and discuss their findings concisely.

2.4.3 Language

Manuscripts must be written in English.

2.4.4 Multimedia Files

The journal supports manuscripts with multimedia files. The requirements are listed as follows:

Video or audio files are only acceptable in English. The presentation and introduction should be easy to understand. The frames should be clear, and the speech speed should be moderate.

A brief overview of the video or audio files should be given in the manuscript text.

The video or audio files should be limited to a size of up to 500 MB.

Please use professional software to produce high-quality video files, to facilitate acceptance and publication along with the submitted article. Upload the videos in mp4, wmv, or rm format (preferably mp4) and audio files in mp3 or wav format.

2.4.5 Figures

Figures should be cited in numeric order (e.g., Figure 1, Figure 2) and placed after the paragraph where it is first cited;
Figures can be submitted in format of TIFF, PSD, AI, EPS or JPEG, with resolution of 300-600 dpi;
Figure caption is placed under the Figure;
Diagrams with describing words (including, flow chart, coordinate diagram, bar chart, line chart, and scatter diagram, etc.) should be editable in word, excel or powerpoint format. Non-English information should be avoided;
Labels, numbers, letters, arrows, and symbols in figure should be clear, of uniform size, and contrast with the background;
Symbols, arrows, numbers, or letters used to identify parts of the illustrations must be identified and explained in the legend;
Internal scale (magnification) should be explained and the staining method in photomicrographs should be identified;
All non-standard abbreviations should be explained in the legend;
Permission for use of copyrighted materials from other sources, including re-published, adapted, modified, or partial figures and images from the internet, must be obtained. It is authors' responsibility to acquire the licenses, to follow any citation instruction requested by third-party rights holders, and cover any supplementary charges.

2.4.6 Tables

Tables should be cited in numeric order and placed after the paragraph where it is first cited;
The table caption should be placed above the table and labeled sequentially (e.g., Table 1, Table 2);
Tables should be provided in editable form like DOC or DOCX format (picture is not allowed);
Abbreviations and symbols used in table should be explained in footnote;
Explanatory matter should also be placed in footnotes;
Permission for use of copyrighted materials from other sources, including re-published, adapted, modified, or partial tables from the internet, must be obtained. It is authors' responsibility to acquire the licenses, to follow any citation instruction requested by third-party rights holders, and cover any supplementary charges.

2.4.7 Abbreviations

Abbreviations should be defined upon first appearance in the abstract, main text, and in figure or table captions and used consistently thereafter. Non-standard abbreviations are not allowed unless they appear at least three times in the text. Commonly-used abbreviations, such as DNA, RNA, ATP, etc., can be used directly without definition. Abbreviations in titles and keywords should be avoided, except for the ones which are widely used.

2.4.8 Italics

General italic words like vs., et al., etc., in vivo, in vitro; t test, F test, U test; related coefficient as r, sample number as n, and probability as P; names of genes; names of bacteria and biology species in Latin.

2.4.9 Units

SI Units should be used. Imperial, US customary and other units should be converted to SI units whenever possible. There is a space between the number and the unit (i.e., 23 mL). Hour, minute, second should be written as h, min, s.

2.4.10 Numbers

Numbers appearing at the beginning of sentences should be expressed in English. When there are two or more numbers in a paragraph, they should be expressed as Arabic numerals; when there is only one number in a paragraph, number < 10 should be expressed in English and number > 10 should be expressed as Arabic numerals. 12345678 should be written as 12,345,678.

2.4.11 Equations

Equations should be editable and not appear in a picture format. Authors are advised to use either the Microsoft Equation Editor or the MathType for display and inline equations.

2.5 Submission Link

Submit an article via https://oaemesas.com/login?JournalId=microstructures.